A cold strontium Rydberg gas

MILLEN, JAMES

A cold strontium Rydberg gas

James Millen

Abstract

Rydberg atoms have come under intense study in recent years due to their exaggerated properties as compared to atoms in the ground state. This thesis describes the design and construction ofthe world's first cold strontium Rydberg gas experiment. We have studied a wide range of Rydberg states, and have developed a sensitive "step-scan" spectroscopic technique that detects the spontaneous ionization of the Rydberg gas. We have used the step-scan method to acquire Stark maps, and used these measurements to test a single-electron model for calculating dipole matrix-elements. From the matrix-elements, interaction strengths between strontium Rydberg atoms have been calculated for the first time.

The presence of two valence electrons in an alkaline earth metal, such as strontium, offers a new angle on the study of Rydberg atoms. We create doubly excited "autoionizing" states in a cold Rydberg gas of strontium. We use autoionization as a high yield probe of Rydberg states, and are able to study excitation dynamics with nanosecond time-resolution. We show that autoionization can quantitatively identify and elucidate state mixing in the Rydberg gas, and probe population transfer at the very onset of ultra-cold plasma formation.

A cold strontium Rydberg gas

James Millen

A thesis submitted in partial fulfilment
of the requirements for the degree of
Doctor of Philosophy

Department of Physics
Durham University

March 12, 2011

Contents

List of Figures

Declaration

I confirm that no part of the material offered has previously been submitted by myself for a degree in this or any other University. Where material has been generated through joint work, the work of others has been indicated.

James Millen
Durham, March 12, 2011

Acknowledgments

When I visited the Durham Atomic and Molecular Physics group in 2007, I was instantly curious about the project involving some strange element, strontium, being proposed by Dr. Matt Jones. He made it clear that working on a new project as the first student, in fact as *his* first student, was a gamble. It was a gamble that certainly paid off! I would like to thank Matt for his constant friendship and guidance, ensuring that I have enjoyed every day I have spent as a Ph.D. student. In a turn of phrase that greatly amused him "I love my project!".

What would the last two and a half years have been like without my fellow strontium student and co-conspirator Graham? Certainly less amusing! Many hours confined in small dark spaces together have enabled us to exploit each others strengths, and have pushed the project to a point at which I am sad to leave it. I am very lucky to have worked in team strontium with Matt, Graham and Danielle, and am jealous that they get to take the project to the next stage of exciting results, especially now that the world is watching!

AtMol is an incredibly friendly group to work in, and I am very grateful to the warm open door policy of, in particular, Prof. C. S. Adams, Dr. I. G. Hughes and Dr. R. M. Potvliege. There have been so many students past and present who have been essential for my day-to-day sanity. I joined the group at a time of real transformation for AtMol, and in particular it has been great to have had Richard Abel and Jon Pritchard there the whole time for mutual support and banter.

I would like to thank my girlfriend Becca for constantly reminding me that there is more to life than physics, a vital lesson for any Ph.D. student to learn! She has helped me explore this wonderful part of the country, that has been as large a part of my life as my studies. I would not have got as far as I have without my parents. They have given me the love, support and confidence necessary to make the right decisions, both professionally and personally. The one regret of my time as a Ph.D. student is that Dad is not here to see me finish.

Dedicated to my father,
thank you for putting me on the right path.

Publications

Publications prepared during the course of this work:

- **Spectroscopy of strontium Rydberg states using electromagnetically induced transparency**
  S. Mauger, J. Millen and M. P. A. Jones
  J. Phys. B: At. Mol. Opt Phys. **40**, F319 (2007)

- **A vapor cell based on dispensers for laser spectroscopy**
  E. M. Bridge, J. Millen, C. S. Adams and M. P. A. Jones
  Rev. Sci. Instrum. **80**, 013101 (2009)

- **Modulation-free pump-probe spectroscopy of strontium atoms**
  C. Javaux, I. G. Hughes, G. Lochead, J. Millen and M. P. A. Jones
  Eur. Phys. J. D **57**, 151-154 (2010)

- **Two-electron excitation of an interacting cold Rydberg gas**
  J. Millen, G. Lochead and M. P. A. Jones
  Phys. Rev. Lett. **105**, 213004 (2010)

- **Spectroscopy of a cold strontium Rydberg gas**
  J. Millen, G. Lochead, G. R. Corbett, R. M. Potvliege and M. P. A. Jones
  Submitted to *J. Phys. B: At. Mol. Opt Phys.* Special issue on strong Rydberg interactions in ultracold atomic and molecular gases (2011)
  arXiv:1102.2715

- **Many-body Physics with Alkaline-Earth Rydberg lattices**
  R. Mukherjee, J. Millen, R. Nath, M. P. A. Jones and T. Pohl
  Submitted to *J. Phys. B: At. Mol. Opt Phys.* Special issue on strong Rydberg interactions in ultracold atomic and molecular gases (2011)
  arXiv:1102.3792

Chapter 1

Introduction

This thesis presents a study of Rydberg states in a cold gas of the alkaline earth metal strontium. Why are we interested in Rydberg states? An understanding of the Rydberg series of an atom is essential in understanding its behaviour. The earliest tests of atomic theories relied upon predicting the nature and behaviour of Rydberg states. However, the field of Rydberg physics has progressed well beyond spectroscopy, and now encompasses ultra-cold physics, plasma physics, molecular physics, quantum and classical phase transitions, quantum information, quantum chaos, even the study of anti-particles. Much of the interest in these fields stems from the extremely strong interactions between Rydberg atoms. One emergent and exciting area of research into Rydberg states concerns many-body effects, such as crystallization and the preparation of many-member entangled states.

Cold gases of alkaline earth metal atoms are under investigation for numerous reasons, and in this thesis the unique aspects of using such a species to study Rydberg physics will be presented. The presence of an extra valence electron provides an additional degree of freedom for studying, controlling, and manipulating Rydberg atoms.

This chapter will:

- Provide a **motivation** for the work in this thesis, in section 1.1.
- Present an overview of the field of **Rydberg physics**, in section 1.2.
- Introduce the concept of **ultra-cold neutral plasma** formation, in section 1.3.
- Introduce some of the experiments in which cold **strontium** is studied, in section 1.4.
- Give an **outline** of the work that is presented in this thesis, in section 1.5.

1.1 Motivation

Previous studies of Rydberg states in cold atomic gases have mainly used cold gases of *alkali metal* elements. An *alkaline earth metal* element like strontium can be used to perform fundamentally different cold Rydberg gas experiments. The presence of two valence electrons leads to the possibility of imaging Rydberg atoms by using the core $5snl \rightarrow 6sn'l$ excitation. Strontium Rydberg and ground state atoms could be trapped simultaneously in the same optical lattice, using the dipole force on the core and primary $5s^2 \rightarrow 5s5p$ transition respectively [1]. This kind of trapped system could be used to study excitation transfer between Rydberg atoms [2] and even the potential for forming a superconducting metal-like state from a gas [3].

The interaction between strontium Rydberg atoms is also fundamentally different to those in the alkali metal atoms. The $^2S_{1/2}$ states in the alkali metals have isotropic *repulsive* dipole-dipole interactions [4]. The $^1S_0$ series in strontium has isotropic *attractive* interactions. Unlike the alkali metals, strontium

Rydberg *and* ground state atoms could simultaneously be trapped in an optical lattice, and their attractive interactions used to form GHZ states [1]. Crystalline states could also be formed from a strontium Rydberg lattice, since the $^3S_0$ states have repulsive interactions.

The ground state of strontium could be dressed with the $5sns$ Rydberg states [5, 6]. If this dressing was performed for degenerate ground state atoms [7], i.e. atoms in a strontium Bose-Einstein condensate [8, 9], with attractive interactions, it could lead to the production of three-dimensional bright solitons, or "matter-wave bullets" [1, 10].

The presence of doubly excited states in strontium is a key motivation for the work in this thesis. We have shown that the interaction between the two valence electrons can be used to identify and measure state mixing in a cold Rydberg gas of strontium [11]. By exciting the inner valence electron we can autoionize Rydberg atoms in the gas, giving us a high yield probe of the Rydberg state population [11, 12]. By pulsing and focusing the autoionizing beam we create a probe of the Rydberg atoms which has spatial, temporal, population and state resolution. There is the potential to focus the beam to smaller than a "dipole blockade radius", and with the ability to detect single ions this will enable us to probe complex, theoretically predicted Rydberg density distributions.

The prospect of trapping strontium Rydberg atoms could be extended to imaging or even laser cooling them using the core transition. We could also create highly exotic doubly excited states, such a "planetary" Rydberg atoms, where both valence electrons are in a Rydberg state [13, 14]. The electrons in such an atom are predicted to be highly correlated [15]; we could study correlation *within* a single atom.

The use of strontium in studying ultra-cold plasmas has already been discussed, where the plasma has been imaged [16], and could be further cooled or trapped [17]. An optical lattice could be used to impose order on a disor-

dered plasma, and imaging could be used to study already highly structured, crystalline plasma systems [18].

There will surely be much research into cold Rydberg gases formed from alkaline earth metal elements in the future, as they offer the potential to study highly correlated quantum and classical systems, and will add a degree of control that is not possible when considering alkali metal Rydberg gases. In the rest of this chapter we will develop some of the ideas that have been introduced above, and discuss in more detail the properties of strontium.

1.2 Rydberg physics

Rydberg states are atomic states of high principal quantum number n. They are interesting because many of their properties are exaggerated as compared to ground state atoms. Rydberg states have large orbital radii, are long-lived, and have large polarizabilities. Some of the scaling laws for Rydberg atoms are collected in table 1.1. Exceedingly highly excited Rydberg states have been created, with $n = 300 \rightarrow 600$, in circular states ($m_l \sim l \sim n$) [19]. This has enabled the study of Bohr-like orbiting electron wavepackets [19], and fundamental tests of quantum decoherence [20].

However, for this thesis the most important property of Rydberg states is that the interaction strength *between* Rydberg atoms is extremely large as compared to that between ground state atoms. The dipole-dipole interaction between atoms scales as n^{11}, as will be shown in chapter 4. This leads to the possibility of long-range, very large, switchable interatomic interactions, as illustrated in fig. 1.1.

The long-range interactions lead to novel binding mechanisms, and Rydberg-ground state [21] and Rydberg-Rydberg state [22] molecules have been created. Interparticle correlations in a Rydberg gas modify the atom-light interaction [23], and the strong dipole-dipole interactions have been mapped

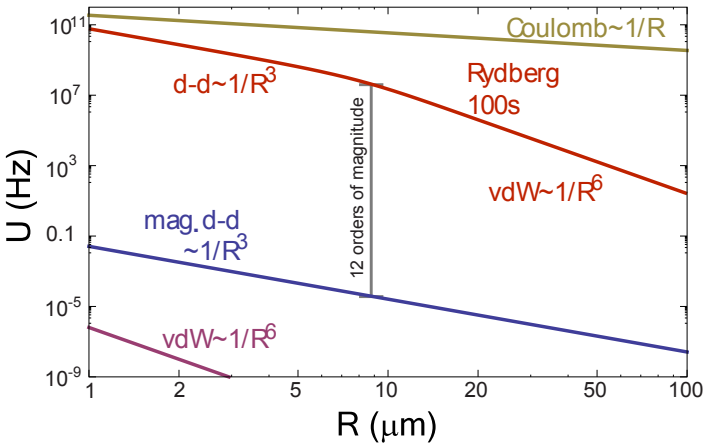

Figure 1.1: The van der Waals and magnetic dipole-dipole interaction strength between ground state Rb atoms (purple and blue lines respectively) compared to the total dipole-dipole interaction strength between Rb atoms in the $100s$ Rydberg state (red line). At interatomic separations of ~ 10 μm the interaction strength between the Rydberg atoms is 12 orders of magnitude larger than between ground state atoms. In our experiment inter-Rydberg atom spacings of $3-5$ μm are common. The coulomb interaction between two singly-charged ions is also shown (gold line).

onto a light field [24]. These modified atom-light interactions could be used to create a photonic phase gate [25].

In fact, much of the interest surrounding the study of Rydberg atoms is their application to studies of quantum information theory [27], where the switchable nature of the interactions could lead to unprecedented fidelity, and the production of quantum many-body states. Both of these utilizations rely upon a process called the "dipole blockade", which will be considered below, followed by its extension to many-body systems.

There are many other interesting areas of physics that involve Rydberg atoms, which will not be covered in detail here. They include, but are not limited to, the presence of Rydberg atoms in helium clusters [28], the production of anti-hydrogen via electron cascade through Rydberg states [29], and Rydberg atom formation through the collision of anti-protons with neutral

Binding energy	n^{-2}
Energy between adjacent n states	n^{-3}
Orbital radius	n^2
Dipole moment $\langle nd\|er\|nf\rangle$	n^2
Polarizability	n^7
Radiative lifetime	n^3

Table 1.1: Rydberg atom scaling laws, reproduced from [26].

atoms [30].

Dipole blockade

The dipole-dipole interaction between atoms in Rydberg states is extremely strong, as compared to those between ground state atoms, as shown in fig. 1.1. The interaction causes a shift in the energy levels of the participating atoms. If the shift is larger than the linewidth of the Rydberg excitation then the probability of having multiple, simultaneous excitations is suppressed. This process is known as the Rydberg dipole blockade. It was proposed that the dipole blockade between two atoms could be used to produce a fast, neutral atom quantum gate [31]. This concept was rapidly extended to a single Rydberg excitation shared amongst *many* atoms, within a sphere of radius R_B: the blockade radius. This shared excitation produces a mesoscopic entangled sample, dubbed a "superatom", with unique applications in quantum information and entanglement enhanced measurement [32].

The dipole blockade between two individually trapped atoms has been experimentally observed [33, 34]. The atoms have been shown to be in an entangled state with a fidelity greater than 0.7 [35, 36], and the atoms have been used to perform a CNOT gate operation [37]. The blockade has been observed in cold atomic gases as a Rydberg atom density dependent suppression of excitation [38–40]. It has been shown that the dipole blockade can

be tuned with an electric field [41], and the dipole blockade has even been observed for Rydberg atoms excited from a Bose-Einstein condensate [42].

Using Rydberg atoms for quantum information theory has several advantages over using ions, superconductors, quantum dots, or any other scheme [27]. Cold neutral atoms offer a large degree of control, with optical trapping being common and well understood. By using Rydberg atoms the interaction-induced entanglement can be "switched on" rapidly, as shown by the 12 orders of magnitude difference in interaction energy between ground and Rydberg state atoms in fig. 1.1; in schemes involving ions the fact that the interactions are always "on" is a limitation, even though the interactions are stronger (fig. 1.1) [27]. The coherence times involved in cold Rydberg atom schemes are exceptionally long, even up to a few seconds [32].

Next, the many dipole blockade mediated collective phenomena that arise when Rydberg atoms are excited in a gas containing many atoms, are discussed.

Many-body physics

We have considered the dipole blockade between two atoms, and a mesoscopic entangled ensemble containing a single, shared Rydberg excitation (a superatom). Much recent work has focused on a system containing many superatom states. When considering uniformly separated superatoms, in an optical lattice, it was found that correlations are preserved over large distances in the lattice [43]. It was shown that for atoms trapped in a ring shaped optical lattice a collective entangled state of the entire system can be formed through Rydberg excitation [44].

These proposed many-body states have very complex excitation dynamics, often requiring very exact initial conditions. However, it was shown that the many-body quantum state could be coherently manipulated, by building up the excitations in a lattice. This leads to a crystallization effect, and this form

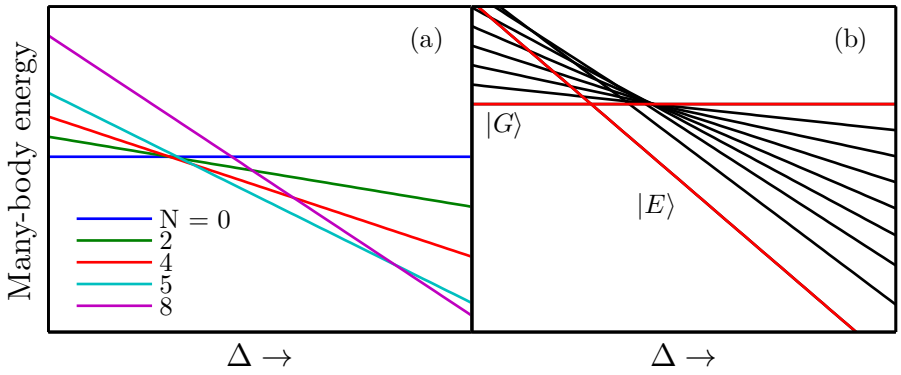

Figure 1.2: (a) The variation in the many-body state energy with Rydberg excitation laser detuning Δ for a system with *repulsive* interactions. As Δ increases from being blue detuned to red detuned, an increasing number N of collective states are created. Reproduced from [45]. (b) If the same process is repeated for a system with *attractive* interactions, then the system evolves from having no collective excitations $|G\rangle$, to having the maximum number of collective excitations $|E\rangle$. Reproduced from [1].

of excitation could be mapped onto a light field [45]. Crystallization, and the closely related quantum melting of the collective excitations [46], offers the opportunity to study quantum phase transitions in a highly controlled, and easy to study, system. The parallel between many-body, dipole blockade mediated, collective excitations in optical lattices and solid-state systems such as crystals (long range order) and paramagnets (short range correlation) has been explored [47]. It has also been suggested that systems of Rydberg atoms can be used as a "quantum simulator", to solve exotic Hamiltonians [48].

The formation of crystalline states relies on *repulsive* interactions between the Rydberg atoms in the lattice, whereby one collective excitation at a time is formed by chirping the Rydberg excitation laser frequency from blue to red detuning [45]. This crystallization is illustrated in fig. 1.2(a), which shows the many-body energy for a system with an increasing number of shared Rydberg excitations. With repulsive interactions, by varying the detuning,

an increasing number of Rydberg excitations can be created, one at a time. This gives rise to the crystallization phenomenon.

The situation in dramatically different for a system with attractive interactions, as illustrated in fig. 1.2(b). In this case, by varying the detuning from blue to red, the first state that is encountered on the many-body energy diagram, when starting in the state with no Rydberg excitations $|G\rangle \equiv |g, g, g...\rangle$, is the *maximally* excited state $|E\rangle \equiv |r, r, r...\rangle$ [1]. Figure 1.2(b) is only an approximation, and in a real system the crossing point of the minimally and maximally excited states is an avoided crossing, and the resultant Landau-Zener transitions lead to the production of an experimentally realizable, high fidelity, entangled Greenberger-Horne-Zeilinger (GHZ) state [1].

1.3 Ultra-cold neutral plasmas

In the previous section the exotic many-body, correlated, quantum systems that can be formed from gases of Rydberg atoms were discussed. Rydberg gases can also form highly correlated *classical* states, in the form of ultra-cold neutral plasmas.

A plasma is a gas of positively and negatively particles, generally ions and electrons, which is "quasi-neutral". Quasi-neutrality requires that, over a certain length scale (the Debye length), the charge in the plasma is balanced, and it appears neutral. The Debye length must be smaller than the total size of the charged gas for the system to be a plasma. Plasmas that occur in nature tend to be exceedingly hot ($> 10,000$ K), since the charged particles are generally created through collisions between neutral atoms, and electron binding energies in neutral atoms are on the order of an electron volt. In this hot regime the dominant energy scale in the system is the kinetic energy of the charged particles, which exceeds the coulomb interaction energy between

the particles in the plasma.

The ability to create very cold, very controlled matter, through laser cooling, enables the creation of an "ultra-cold" neutral plasma. The first ultra-cold plasma was created by photoionizing a fraction of laser cooled xenon [49]. The excess energy above the photoionization limit is shared between the ions and electrons, but due to their much smaller mass the electrons take most of the kinetic energy. In this way, a plasma with ion temperatures as low as 10 μK, electron temperatures as low as 100 mK, and densities as high as 2×10^9 cm^{-3} is created [49]. It was shown that in these ultra-cold plasmas the interparticle interaction energy is greater than the thermal energy of the particles [50]; these plasmas are "strongly coupled"[1].

Strongly coupled plasmas are a very exotic phase of matter. Examples are few and far between, but include the interior of highly evolved stars, the core of Jupiter, laser implosion induced plasmas, explosive shock tubes, electrons on the surface of liquid helium [51], and the quark-gluon plasma [52]. The ions in a strongly coupled plasma are spatially correlated, as they rearrange themselves to minimize the potential energy of the system [53]. This is predicted to lead to the creation of shell structures for the ions in cold plasmas, as can be seen in fig. 1.3(a); the plasma will crystallize [18].

The evolution dynamics of an ultra-cold plasma have been studied using absorption imaging [16]. The plasma was formed by photoionizing cold strontium, and strontium ions have an optical transition at $\sim$ 422 nm, which enables the absorption imaging technique. This study revealed novel expansion dynamics in the plasma, and ions existing on the boundary of a gaseous and liquid state. Another observed process in ultra-cold plasmas is the recombination of ions and electrons into Rydberg states [55]. Up to 20% of the

[1] Further work suggests that heating in the plasma rapidly breaks the strongly coupled condition [18], though this could be overcome by further cooling the plasma after its formation [17].

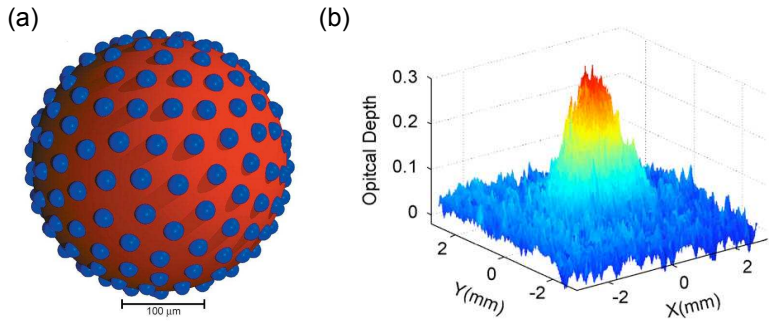

Figure 1.3: (a) Arrangement of ions (blue spheres) in an expanding ultra-cold plasma. This image represents one of many ion shells that are predicted to form. Taken from [18]. (b) Absorption image of an ultra-cold plasma created from strontium. The strontium ions have an optical transition at $\sim$ 422 nm. Taken from [54].

initial free charges were found to recombine to form Rydberg atoms, within 100 μs of the formation of the plasma. A broad range of Rydberg states are populated through this process.

Photoionization is not the only way to form an ultra-cold neutral plasma. It was observed that a gas of cold Rydberg atoms could *spontaneously* evolve into a plasma [56]. Rydberg gases exhibit a degree of rapid spontaneous ionization (see section 3.1). Since the atoms are initially cold, the spontaneously created electrons rapidly leave the gas, while the corresponding ions remain essentially stationary, leaving a net positive charge. Further spontaneously created electrons are bound by the positive charge, forming a plasma [57]. The electrons subsequently oscillate through the Rydberg gas, causing further ionization, and a redistribution of population amongst different Rydberg states [57, 58]. The correlations between ions in a plasma formed from a cold Rydberg gas has a quantitative effect on the evolution dynamics [59].

Ultra-cold plasmas formed from cold atomic gases are already shedding light on the complex dynamics predicted in strongly coupled plasmas, and the control will only improve if the plasmas can be cooled or even trapped [17].

1.4 Strontium

We have introduced some of the reasons for studying cold gases of Rydberg atoms. In this section we discuss some of the unique aspects and prospects of working with strontium.

Strontium is an alkaline earth metal element, in group two of the periodic table. It has three Bosonic isotopes, ^{88,86,84}Sr, with a relative abundance of 82.58, 9.86, 0.56% respectively. These isotopes have no nuclear spin, which leads to no hyperfine structure. The ground state, $5s^2\,{}^1S_0$, is completely unique, with no substructure. There is also a Fermionic isotope, ^{87}Sr, with a relative abundance of 7.00%, and a nuclear spin of $I = 9/2$. More properties of the isotopes of strontium can be found in table A.3.

Group two atoms offer certain advantages over alkali metal atoms when considering the creation of a cold gas. The ground state is a closed shell $^1S_0$ state. This leads to fewer elastic scattering channels, allowing for the creation of a higher density trapped cloud [60]. This ground state has no magnetic structure, and for the Bosonic isotopes no hyperfine structure. This offers a simple system, and one in which the theories of Doppler cooling and light assisted collisions can be tested [61].

The most important property of strontium for the experiments presented in this thesis is that the atom has two valence electrons, or is "divalent".

The divalent nature of strontium means that it supports both singlet and triplet electronic spin states. Although transitions between the singlet and triplet states are "forbidden", according to the electric dipole transition selection rules, transitions do become weakly allowed due to higher order electric and magnetic multipole effects [62, 63]. Singlet-triplet transitions have very small linewidths. The $5s^2\,{}^1S_0 \rightarrow 5s5p\,{}^3P_1$ transition (see fig. 2.10), which has a linewidth of $2\pi\times$7.5 kHz, has been been used to cool ^{88}Sr to 400 nk, with a ground state density of over 10^{12} cm^{-1}, and a phase space density of 10^{-2}

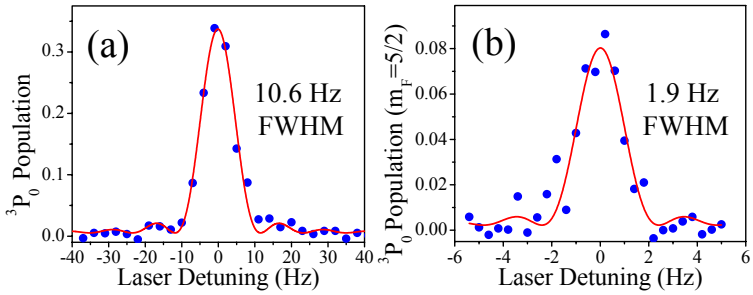

Figure 1.4: (a) Lineshape of the $^1S_0 \rightarrow {}^3P_0$ clock transition in ^{87}Sr, measured using an electron shelving technique. (b) The same transition, specifically addressing the $m_F = 5/2$ level of the $^3P_0$ state. Reproduced from [67].

[60].

Singlet-triplet transitions are also useful for performing high precision spectroscopy [64], which has important applications in fundamental frequency metrology. The state of the art is the ^{87}Sr lattice clock [65–67], which has reached a systematic uncertainty of 9×10^{-16} [67], which is comparable to the caesium fountain clock standard, and the lattice clock is close to pushing below the 1×10^{-17} limit [68]. Coherence times of 1 s have been achieved experimentally, and of 100 s are predicted theoretically [64]. The absolute transition frequency measurement in a ^{87}Sr lattice clock is the most accurate neutral atom frequency measurement there is, and has been used to constrain fundamental constants [69]. Examples of the extremely narrow lines that have been measured in ^{87}Sr are shown in fig. 1.4.

There is interest in the creation of Bose-Einstein condensates (BECs) from alkaline earth metal atoms, due in part to their rich internal structure as compared to the alkali metals. The isotope ^{84}Sr has been condensed, chosen because of its favourable scattering properties [8, 9]. The unique properties of degenerate gases of alkaline earth metals could be used to perform quantum gate measurements, quantum simulation and to build few qubit quantum registers [70, 71].

The divalency of strontium also means that the atom can support doubly

excited states, which will be covered in detail in Part II of this thesis.

As a final point, singly ionized strontium Sr^+ has a transition $^2S_{1/2} \rightarrow {}^2P_{1/2}$ at 422 nm ($\Gamma = 2\pi \times 22$ MHz), which has been used to absorption image ions in an ultra-cold plasma [16]. This technique is only possible in atomic species whose ions have an optical transition, and is a unique non-destructive probe of plasma dynamics.

In this thesis the ^{88}Sr isotope is cooled in a magneto-optical trap (MOT) using the $5s^2\,{}^1S_0 \rightarrow 5s5p\,{}^1P_1$ transition (see fig. 2.10), which has a linewidth of $2\pi\times32$ MHz. This allows cooling to a few mK. For more information on this cooling transition see section 2.4.

1.5 Outline

In this thesis, the first study of Rydberg states in a cold gas of strontium is presented. The design and detail of an experiment to cool and trap strontium, and create a gas of atoms in a Rydberg state, will be outlined in chapter 2. We have developed unique experimental techniques and apparatuses for working with strontium. We employ a unique "step-scan" method for performing highly sensitive spectroscopy of Rydberg states, where the spontaneous ionization of the Rydberg atoms is used as the signal. A characterization of the step-scan technique, and results of performing Rydberg state spectroscopy, are presented in chapter 3. A simple theoretical model for describing the energy structure of alkaline earth metals is described, where the Rydberg electron is considered to behave independently from the inner valence electron. This "single-electron" model is extended to describe highly excited Rydberg states, up to a principal quantum number of $n = 81$, in chapter 4. The ability to perform sensitive spectroscopic measurements allows for a verification of the single-electron model, which is utilized to calculate interaction energies between strontium atoms in Rydberg states.

By optically exciting the inner valence electron of strontium Rydberg atoms, the atom is autoionized. This is the first study of autoionizing states in a cold gas. In chapter 5 we show that autoionization is a highly sensitive probe of Rydberg states, and can be used to explore population dynamics on a nanosecond timescale. Excitation of the inner valence electron yields information on the state of the Rydberg electron. By studying the spectrum of the autoionizing transition, density dependent state mixing in the Rydberg gas is observed. A study of the autoionization spectra is presented in chapter 6, and enables a quantitative analysis of population transfer in an interacting Rydberg gas. The formation of an ultra-cold plasma is identified as the dominant transfer mechanism. We have performed a unique study of state mixing at the very onset of plasma formation in a cold Rydberg gas.

Part I

Spectroscopy of a cold strontium Rydberg gas

Chapter 2

The cold strontium experiment

Introduction

This experiment is designed to study a cold Rydberg gas of strontium. The strontium is cooled and trapped in a magneto-optical trap (MOT). There are several design considerations that are unique to working with an alkaline earth metal element such as strontium, as opposed to an alkali metal such as rubidium.

Unlike the alkali metals, strontium must be heated to form a gas, due to its negligible vapour pressure at room temperature. The hot strontium must be formed into a beam, and the beam must be slowed. A Zeeman slower [72] is used to create a beam of strontium which is cold enough to be trapped in a MOT. The bosonic isotopes of strontium have no hyperfine structure, so sub-Doppler cooling methods [73] are not available.

The magnetic field gradient required to trap strontium is $\sim 30\ \mathrm{G\,cm^{-1}}$, as compared to $\sim 100\ \mathrm{G\,cm^{-1}}$ for rubidium. In this experiment, the coils that produce the magnetic field are placed *inside* the vacuum system, so that the field can be created without the need for water cooling.

The frequency of the cooling laser must be stabilized. A standard technique utilized in many cold atom experiments is to "lock" the laser to an atomic

resonance, obtained by performing spectroscopy on a sample contained in a glass vapour cell. However, hot strontium reacts with reacts with glass, meaning standard vapour cells cannot be used. We have developed our own strontium vapour cell [74] to overcome this problem.

There are specific design requirements for studying Rydberg states, as opposed to a cold gas of atoms in their ground state. One issue is detection. The radiative lifetime of an atomic state scales approximately as the principal quantum number n^3, hence Rydberg atoms do not scatter as much light as ground state atoms, so typical absorption/fluorescence detection techniques are not viable [75].

As will be described in detail in chapter 3 we detect the Rydberg atoms through spontaneous ionization. This requires a micro-channel plate (MCP) detector to detect ions, and electrodes to direct charge to the MCP, both of which are mounted inside the vacuum. The experiment is under computer control, managing both the timing of the experimental sequences, and data acquisition.

This chapter will:

- Detail the **apparatus** required to create a cold gas of strontium in section 2.1.
- Describe the **laser system** used, and our frequency stabilization technique in section 2.2.
- Describe our **measurement techniques** for acquiring data in section 2.3.
- Present details of our magneto-optically trapped **cold gas of strontium** in section 2.4.

2.1 Apparatus

The core requirements for an experiment to produce a magneto-optically trapped gas of strontium are relatively simple, and a scale diagram is shown in fig. 2.1.

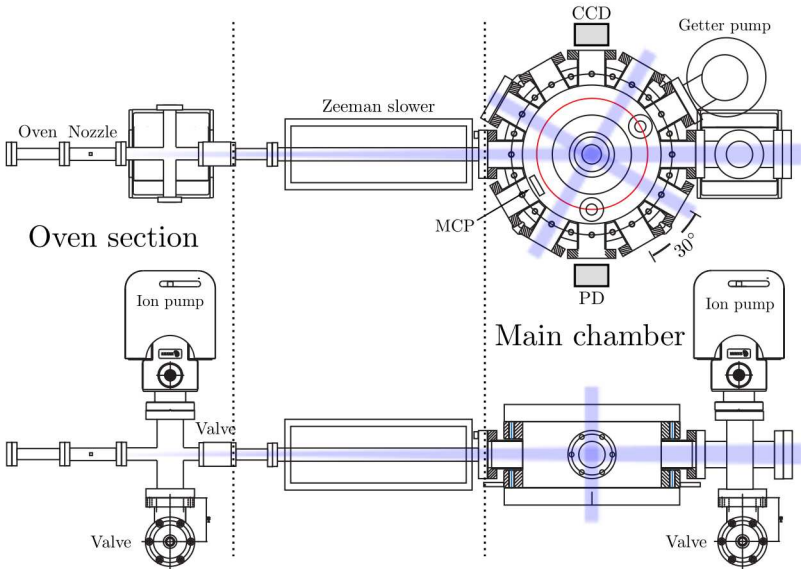

Figure 2.1: A scale diagram of the vacuum apparatus, with the MOT and Zeeman slower beams indicated. The MOT magnetic field coils, electrodes and MCP are mounted inside the main chamber. There is a CCD camera and a photodiode (PD) mounted outside of the chamber.

The apparatus can be separated into three core sections: the oven, which produces the hot beam of strontium; the Zeeman slower, which slows this beam; and the main chamber where the atoms are trapped in a MOT, and excited to Rydberg states. The geometry of the MOT beams and the Zeeman slower beam are marked on fig. 2.1.

Unless specifically noted, the entire system is constructed from stainless steel, and connected with Conflat flanges and copper gaskets. All view-ports on the experiment are Kodial glass, custom anti-reflection coated by CVI Melles Griot. In total, the entire system is 115 cm long.

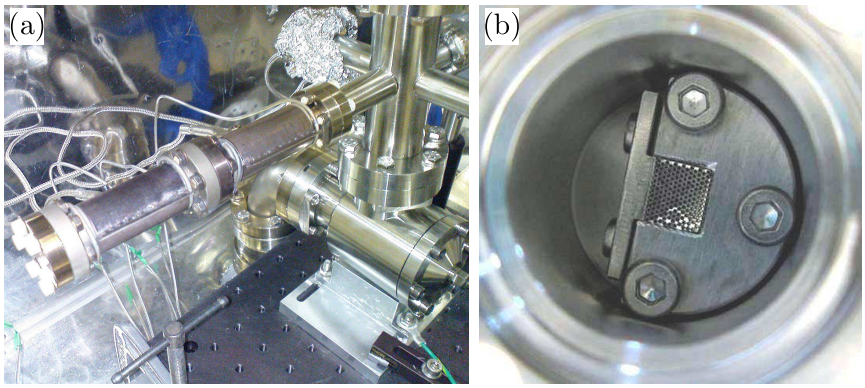

Figure 2.2: (a) A photograph of the oven tube, where strontium metal is heated to approximately 900 K, followed by the nozzle tube. Heater wire is clamped onto the vacuum tubing. (b) A photograph of the nozzle, formed from an array of steel capillaries, which sits inside the vacuum tube. The nozzle forms a beam from the hot atomic vapour.

2.1.1 Oven

The oven heats strontium metal to approximately 900 K. The variation in the vapour pressure of strontium metal with temperature can be found in [76]. A gate valve allows the oven to be isolated from the rest of the experiment, enabling the oven to be reloaded without having to lose vacuum in the main chamber. The oven section has an angle-valve[1], so it can be separately evacuated.

The design for the oven is based on [77]. A standard 76.2 mm DN16 Conflat full-nipple, which is shown in fig. 2.2(a), is loaded with 5 grams of strontium metal. Following the first full-nipple is a custom 82 mm full-nipple containing a "nozzle" formed from 169, 8 mm long, 170 μm diameter stainless steel capillaries, as shown in fig. 2.2(b). The nozzle collimates the hot atomic beam, giving it a geometric divergence of ~ 43 mrad full width. These sections are sealed using nickel gaskets, since hot strontium reacts with copper.

[1] All angle valves on the experiment are VAT All Metal Angle Valves.

The oven is heated by heater wire[2], which is clamped onto the vacuum tubing. The nozzle has a separate and identical heater, which is held at a higher temperature to prevent condensation of the strontium in the capillaries. The oven and nozzle, visible in fig. 2.2(a), is wrapped in fibre-insulation and foil.

Directly after the heated nozzle section is a six-way cross (see fig.2.1), which has two DN16 view-ports, an ion pump[3], and the angle-valve. When the oven is not running this region is at a pressure of 5×10^{-11} Torr. The pressure in the vacuum system is measured by monitoring the ion current from the ion pumps, and will not be accurate below $\sim 1 \times 10^{-11}$ Torr.

2.1.2 Zeeman Slower

The strontium leaving the oven travels at approximately 500 ms^{-1} at 900 K. In order to be trapped in the MOT these hot atoms must be slowed. We use the standard technique of Zeeman slowing [72], where a beam of laser light (counter-propagating to the atomic beam) is kept in resonance with the decelerating atoms through the Zeeman effect. The light is circularly polarized with respect to the Zeeman slower magnetic field, and operates on the $5s^2\,{}^1S_0 \rightarrow 5s5p\,{}^1P_1$ transition, which has a linewidth of $\Gamma = 2\pi \times 32$ MHz. A photograph of the Zeeman slower is shown in fig. 2.3(a).

The Zeeman slowing is purely axial, and due to the decreased axial velocity the radial divergence is increased. For this reason the slower should be kept as short as possible, and the MOT must be as close as possible to the end of the slower. So as not to perturb the trapped atoms, good field cancellation is required outside of the slower. The absorption of the slowing light, and consequential spontaneous emission, causes further divergence. The divergence can be countered to some extent by focusing the slowing beam. The Zee-

[2] Thermocoax SEI 20/150, rated up to 1000°C.

[3] The ion pumps used on this experiment are Gamma Vacuum "TiTan 20S" ion pumps.

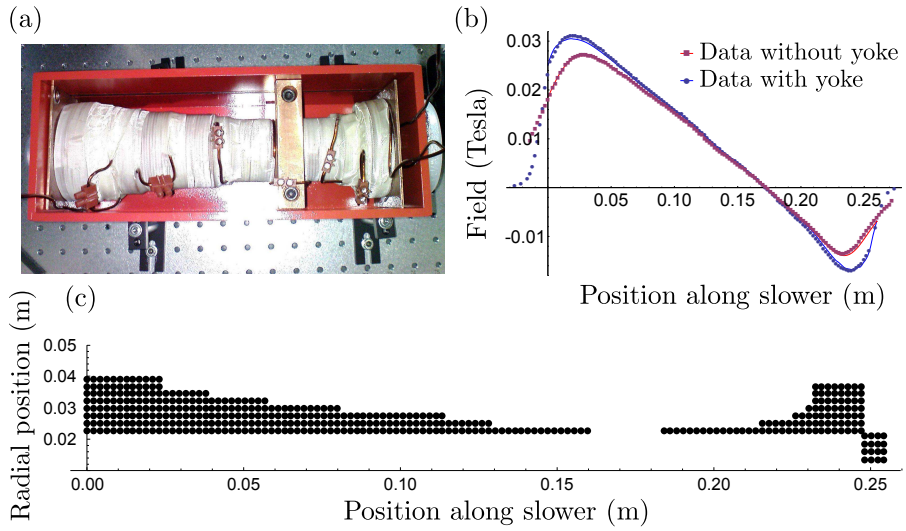

Figure 2.3: (a) A photograph of the Zeeman slower, from above. The coils are wrapped in insulation tape (white). The slower is encased in a mild steel yoke (red). (b) The magnetic field along the slower axis. The red dots/line are data/simulation without the yoke, the blue dots/line are the data/simulation with the yoke. (c) A turn diagram, with each dot representing the cross section of a turn. The 4×4 square of coils at the end are wound directly onto the vacuum tubing.

man slower beam has a $1/e^2$ waist of 13.62 mm parallel to the optical bench, 8.88 mm perpendicular to the bench, where it enters the vacuum chamber. The focus is approximately 900 mm from the entry view-port, which is the position of the nozzle in the oven.

Design of the magnetic field

There are several possible configurations for the magnetic field in a Zeeman slower. The simplest methods are to create either a steadily increasing, or decreasing, magnetic field. The disadvantage of the decreasing field method is that the light for the Zeeman slower is not detuned as far from resonance as with the increasing field case, and this may perturb the atoms in the MOT. The disadvantage of the increasing field method is that the largest magnetic field is closest to the trapped atoms.

We use a hybrid approach, and have built a "zero-crossing", or "spin-flip", Zeeman slower. In this design the magnetic field passes through zero, as shown in fig. 2.3(b). A potential disadvantage of this method is that as the atoms pass through the field zero-crossing the quantization axis for the atoms changes, and population can be redistributed amongst hyperfine sublevels. This is not an issue for ^{88}Sr, as the ground state is unique, with no hyperfine structure. The advantage of the hybrid design is that, by crossing zero magnetic field, the overall magnitude of the field can be reduced, hence reducing the field outside the slower, and reducing the amount of power dissipated in the coils.

In addition we contain the magnetic field coils in a mild steel yoke, as can be seen in fig. 2.3(a). The magnetic field profile with and without the yoke is shown in fig. 2.3(b). The yoke boosts the field at the ends of the slower, and causes the field to decay faster away from the slower.

A thorough discussion on calculating the shape of the magnetic field required to slow the atoms is given in [78]. Our Zeeman slower was designed by Dr. M. P. A. Jones. We use a detuning of -500 MHz (15.6 Γ) from the cooling transition, and the slower is 25 cm long. The calculated and measured field profile along the slower is shown as the red data on fig. 2.3(b). The mild steel yoke was included into the simulation by using a magnetostatic imaging technique, and the measured and simulated field profile with the yoke is shown as the blue data on fig. 2.3(b). The agreement between the theory and the data, both with and without the yoke, is excellent. Numerical simulations suggest that this slower design can slow up to 8% of the hot atoms.

Construction of the Zeeman slower

The physical turn profile of the Zeeman slower required to produce these fields is calculated following [78], and is shown in fig. 2.3(c). The magnetic field is calculated by considering the contribution from each individual turn. The windings are in two sections, as can be seen in fig. 2.3(c). Both sections are driven with 9 A, circulating in opposite directions. The magnetic field at the end of the slower is enhanced by turns wound directly onto the vacuum tubing, driven with 17 A.

The slower was constructed by hand-winding layers of insulated 1 mm diameter copper wire around a 41 mm diameter copper former. The turns are sealed in place with epoxy resin, and the layers separated by heat resistant fibre tape. The copper former includes a large block in the centre which acts as a heatsink. The yoke is open at the top (though not at the bottom), and this was found not to noticeably affect the magnetic field, and allows for dissipation of heat.

The yoke is secured to the copper former, and the slower arrangement sits over a DN16 full-nipple connecting the oven to the main chamber. There is a gap between the yoke and the end of the copper former, as is visible on the far right of fig. 2.3(a). In this gap there are the few turns of copper wound directly onto the vacuum tube. The entire apparatus is 27.5 cm long from each end of the yoke, and does not require water cooling.

2.1.3 Main chamber

The Zeeman slowed atoms are trapped in the "main chamber" region of the apparatus, as illustrated in fig. 2.1. The main chamber is at a pressure of 3×10^{-11} Torr, and serviced by an ion pump and a getter pump[4]. The ion pump has additional magnetic shielding to protect the trapped atoms from

[4] SAES Getters "CapaciTorr B200" non-evaporative getter (NEG) pump.

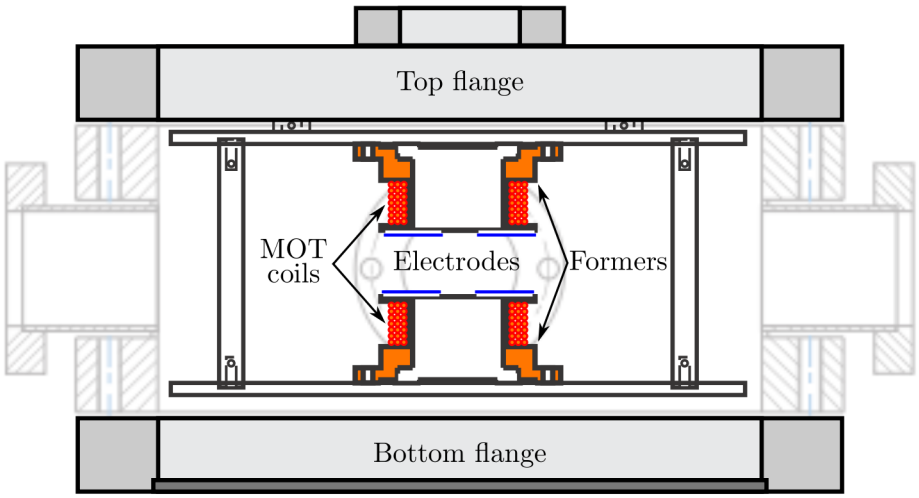

Figure 2.4: A scale cross-section through the main chamber. The internal MOT coil former assembly is mounted to the top flange. Electrical connections to the MOT coils and electrodes are made through electrical feed-throughs on the top flange (not shown).

stray fields. The chamber region is protected from the higher pressure of the hot oven by the 290 mm long DN16 bore Conflat full-nipple joining the sections together (around which the Zeeman slower is mounted).

The main chamber is a stainless steel twelve-port "pancake" shaped chamber, which is 30 cm in diameter from flange-face to flange-face, and 95 mm deep. A cross-section is shown in fig. 2.4. Each port on the circumference is DN40 size. Eight of the ports around the circumference have windows. The view-port that is in direct line-of-sight with the hot atomic beam could be heated to limit any deposition of strontium. However, we have not done this, and after two years of continuous use have noticed no significant coating.

The top and bottom of the chamber is sealed with DN200CF flanges. The top flange is a DN200 to DN40 zero length adapter, with a centred DN40 view-port, and two electrical feed-throughs. One feed-through has 4-pins, a rating of up to 5 kV and 30 A, and supplies two pairs of electrodes. The other has 10-pins, a rating of up to 700 V and 10 A, and supplies the MOT

coils and remainder of the electrodes. The bottom flange has a centred 8" window.

Internal equipment

The coils for producing the MOT magnetic field are mounted inside the main chamber. By driving the coils in an anti-Helmholtz configuration we create the required magnetic field, with a gradient of 30 $\mathrm{G\,cm^{-1}}$ at the position of the trapped atoms. The coils are driven with 2.5 A, and do not require water cooling.

The MOT coils are Kapton insulated, 1 mm diameter copper wire, wound onto copper formers that are mounted onto the DN200CF top-plate of the chamber, as can be seen schematically in fig. 2.4, and as a photograph in fig. 2.5(a). The copper formers do not form a continuous ring, to prevent circulating induced currents, and they also act as a heatsink for the coils. The coils have a minimum radius of 16.5 mm, and each coil has 60 turns. The design is such that the zero-point of the magnetic field is at the centre of the chamber.

The current supplied to the MOT coils can be switched using a FET switch circuit (fig. B.3 in appendix B). This circuit has a rise time of ~ 8 μs and a fall time of ~ 20 μs. The circuit is switched using a TTL from the computer control.

There are a set of electrodes inside the vacuum system, arranged in a split-ring geometry, as shown in fig. 2.5(b), following the design of [79]. The electrodes are made from 0.5 mm thick stainless steel, machine and hand polished to a good finish. They are connected to the electrical feed-throughs with 1 mm diameter stainless steel wire, which is spot-welded to the electrodes. The inner radius of the split ring is 14.5 mm and the outer radius is 26 mm, with a 1.5 mm gap between each electrode.

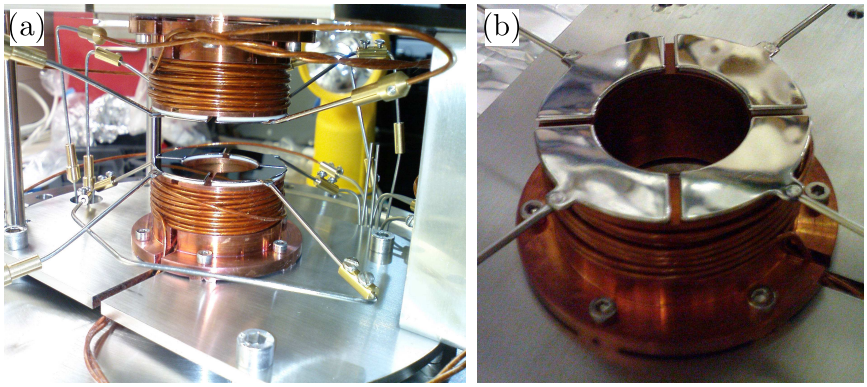

Figure 2.5: (a) A photograph of the main apparatus that is inside the vacuum system, mounted on the DN200CF top-plate. The magnetic field for the MOT is created by a pair of coils formed from Kapton insulated copper wire. Eight electrodes are mounted onto these copper formers, insulated by ceramic spacers. (b) A close-up photograph of one of the pairs of four electrodes in a split-ring geometry.

The two pairs of four electrodes are mounted onto the copper formers for the MOT coils, as illustrated in fig. 2.4 and visible in the photographs in fig. 2.5. The electrodes are insulated from the formers by 1 mm thick ceramic spacers. The spacers are a similar shape to the electrodes, with an inner radius of 15.5 mm, an outer radius of 25 mm, and a 3 mm gap between each spacer. The separation between each set of four electrodes is approximately 19 mm (not accounting for the vacuum grade epoxy bonding the electrodes to the spacers, and the spacers to the former).

The electrodes are used to create static or pulsed electric fields. The electric field is simulated by solving Laplace's equations in 3-D. Details of the simulation can be found in appendix C. The electrodes direct charge to a microchannel plate detector (MCP)[5], which detects ions produced in our experiment. The MCP is mounted directly onto a DN40 Conflat flange, with the flange carrying the electrical feed-throughs. The position of the MCP can be seen in fig. 2.1. It sits next to the port through which the Zeeman

[5] Hamamatsu Compact MCP Assembly F4655.

slowed atomic beam enters the vacuum chamber, i.e. not in line-of-sight with the hot atoms. Further protection from the hot atoms is provided by a metal baffle, which sits between the detector and the port where the atoms enter. The MCP is covered by a home-built steel grid. By supplying a voltage to this grid the collection efficiency of the detector can be increased.

2.2 Laser system

Lasers are a key component of any cold atom experiment. In our experiment they slow, cool and trap the atoms, and are used to populate Rydberg and autoionizing states. This section will describe the lasers that we use, and the method we use to frequency stabilize our cooling laser.

2.2.1 Lasers

The primary cooling transition in strontium, $5s^2\,{}^1S_0 \rightarrow 5s5p\,{}^1P_1$, is at 460.7 nm. The atoms are excited to the Rydberg state via the intermediate $5s5p\,{}^1P_1$ state, using light at $\sim$ 420 or 413 nm, to access states of principal quantum number $n = 17$ right through to the ionization threshold.

This highlights another experimental difficulty when working with an alkaline earth metal, as opposed to an alkali metal where the primary transitions are at red wavelengths. Red laser diodes are readily and cheaply available, whereas blue diodes, required to access the primary transitions in strontium, are not. Instead, laser diodes in the infra-red are used, and the light is subsequently frequency-doubled. This requires a non-linear crystal in a build up cavity.

The laser for the cooling/trapping, and the two lasers used for Rydberg excitation are the same design. They are Toptica DL-SHG frequency-doubled diode laser systems. All three come with supply electronics, which stabilizes

the cavity length, and allows for external frequency stabilization.

The cooling laser fundamental is 922 nm, and the laser system includes a tapered amplifier, leading to maximum output power at 461 nm of ~ 350 mW. One of the Rydberg excitation lasers has a fundamental wavelength of 842 nm, and a maximum output power at 421 nm of ~ 20 mW. This laser can access Rydberg states from $n \sim 17 \rightarrow 20$. The other Rydberg excitation laser has a fundamental wavelength of 824 nm, and a maximum output power at 412 nm of ~ 10.5 mW. During the course of this project the 412 nm system had a tapered amplifier added, taking the maximum output power to ~ 70 mW. This laser can access Rydberg states from $n \sim 33$ to above the ionization threshold (see table A.1).

The lasers that are used to excite the inner valence electron will be described in Part II of this thesis.

2.2.2 Laser stabilization

To create a cold, trapped gas of strontium the 461 nm cooling laser must be frequency stabilized. A common way of doing this is to use the atomic transition to produce an "error signal" [80], which is a signal that crosses zero at the point of the atomic resonance, and use servo electronics to keep the laser on resonance. Broadly speaking there are two ways to generate the error signal: by modulating the frequency (or phase) [81–83] of the laser, or through a direct spectroscopic method. Both modulation and non-modulation techniques require an atomic source, and we have developed a novel dispenser cell for strontium [74], which is described below.

Modulation techniques are not always desirable. If the light is modulated at the laser source, then all of the beams derived from that laser carry the modulation. Otherwise, an expensive external modulator must be used. On the other hand, modulation techniques are very sensitive. For example, elec-

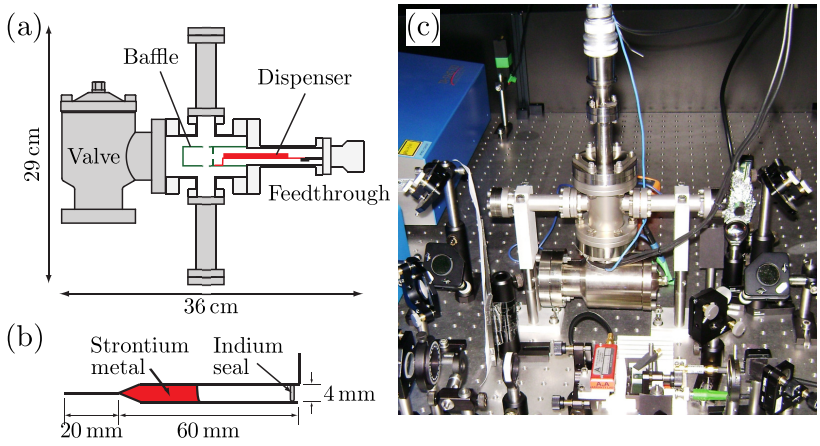

Figure 2.6: (a) A diagram of the dispenser cell. The dispenser is heated by passing a current through it, and spectroscopy is performed transverse to the direction of the ensuing atomic beam. (b) A diagram of the commercial strontium dispenser used in the dispenser cell. (c) A photograph of the dispenser cell in use. The cell can be mounted vertically, as shown, or horizontally, flat to the bench.

tromagnetically induced transparency can be used to generate error signals for high lying Rydberg states [84], and this technique will be used in future on this experiment.

There are various non-modulation laser stabilization techniques. We have studied sub-Doppler DAVLL (Dichroic Atomic Vapour Laser Locking) [85] and polarization spectroscopy [86] in strontium [87]. We have chosen to use polarization spectroscopy in this experiment, since it is free of any Doppler-broadened absorption background, and this method is discussed below.

Strontium dispenser cell

The study of thermal vapours has been central to the study of atomic physics, with laser spectroscopy in particular being fundamental to the understanding of atomic structure. The majority of cold atomic physics experiments use alkali metals, such as rubidium and caesium, which have sufficient vapour pressure at room temperature such that a simple glass cell can be used for

spectroscopy.

However, strontium metal must be heated. Hot strontium chemically reacts with glass and copper, which are materials commonly used in vacuum apparatuses. Some experiments have got around this problem by using complex techniques such as buffer gases, water cooling, and the use of sapphire glass windows [57, 88, 89]. The other option is to build a bulky atomic beam machine, as we have used in [90].

We have designed a compact cell based on commercial dispensers, which operates at room temperature, and does not require the use of a vacuum pump during operation [74]. The cell was designed by Dr. M. P. A. Jones, and built by Clémentine Javaux.

The design of the cell is shown in fig. 2.6(a). A strontium dispenser (Alvatec AS-Sr-500-F), shown in fig. 2.6(b), is mounted to an electrical feed-through at one end, and the open end is mounted to an enclosing baffle, which allows electrical current to return to ground via the cell wall. The baffle fully encloses the dispenser, except for two small holes to allow for transverse spectroscopy of the atomic beam that leaves the dispenser. The cell windows are DN16CF *uncoated* windows[6], and are not in life-of-sight with the dispenser. After two years of operation there has been no evidence of significant strontium deposits on the windows.

The dispenser is heated by passing a current through it, and emits a weakly collimated jet of strontium. The electrical feed-through of the cell is rated to 20 A, and in standard operation approximately 12 A is sufficient to produce enough strontium vapour for spectroscopy. When the dispenser runs out it is simple to replace, requiring a day to pump back to vacuum. This only needs to be done approximately yearly under continuous use.

The room temperature metal of the baffle adsorps the strontium vapour, and

[6] We are unsure as to whether strontium will react with anti-reflection coating.

this deposited metal also acts as a getter, meaning that no external pumping is required during standard operation. The cell is sealed with an all-metal valve.

The dispenser is filled with 500 mg of strontium metal, and is shown in fig. 2.6(b). The strontium metal is held under an argon atmosphere, and the open end is sealed with an indium seal, enabling the dispenser to be handled in ambient conditions. Initially the dispenser must be activated by heating until the indium seal melts ($5 - 8$ A), and the argon gas must be pumped away.

By performing spectroscopy of the $5s^2\,{}^1S_0 \rightarrow 5s5p\,{}^1P_1$ transition the FWHM of the transverse velocity distribution was found to be $158 \pm 5\ \mathrm{m\,s^{-1}}$.

Polarization spectroscopy

We perform polarization spectroscopy ("pol-spec") in our dispenser cell to stabilize the frequency of the cooling laser. A schematic for the optical layout is shown in fig. 2.7(a). A circularly polarized pump beam induces a birefringence in the strontium vapour, which is interrogated with a counter-propagating, linearly polarized probe beam of the same frequency. As shown, the pump and probe derive from the same beam, and typically have intensities of 200 and 5 $\mathrm{mW\,cm^{-2}}$ respectively ($I_{\mathrm{sat}} = 43\ \mathrm{mW\,cm^{-2}}$).

The output signal is the difference in intensity (as measured with a differencing photodiode) between the two outputs of a polarizing beamsplitter (PBS) cube, through which the probe beam passes after going through the cell. The probe beam is initially linearly polarized. After the cell the linear polarization is rotated to an angle of $\phi = \pi/4$ to the axis of the PBS cube, using a $\lambda/2$ waveplate. The PBS cube separates the two circular components of the polarization. When just the probe light passes through the cell the signal on the photodiode is zero for all laser frequencies.

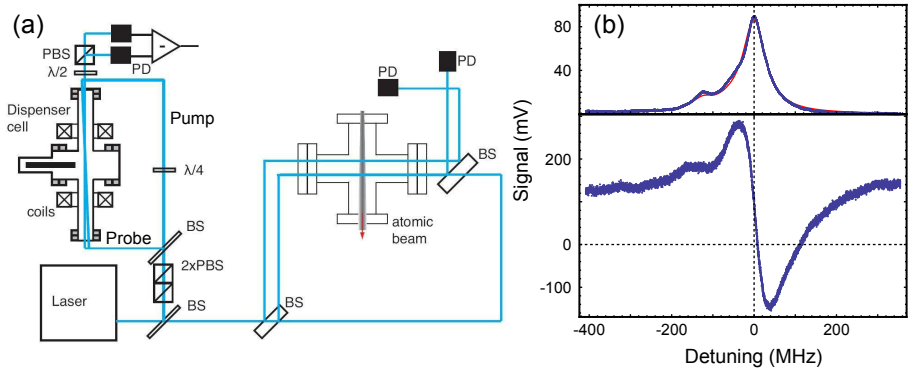

Figure 2.7: (a) A schematic of the set-up to perform polarization spectroscopy (pol-spec) using our dispenser cell. The frequency axis can be calibrated by performing simultaneous saturated absorption spectroscopy (sat-spec) in a beam machine. (b) An example lineshape generated from pol-spec (lower figure), and the corresponding sat-spec used to calibrate the frequency axis (upper figure). The offset of the pol-spec background from zero can be adjusted with the $\lambda/2$ plate before the analyzing PBS cube, shown in (a).

The presence of the circularly polarized pump beam saturates the transition from the ground state to one of the $m_J = \pm 1$ Zeeman sublevels of the $5s5p\,{}^1P_1$ state, thus inducing a circular birefringence in the medium. The birefringence adds an additional rotation Φ to the polarization of the probe beam, and the output signal is no longer zero for all laser frequencies.

An example of the difference signal is shown in the lower frame of fig. 2.7(b). It is an error type signal, with the zero crossing corresponding to the resonant transition frequency for the ^{88}Sr isotope. Contributions from the other isotopes are visible on the negative detuning side. Sometimes, as in fig. 2.7(b), the entire signal is offset from zero, which means that the initial rotation of the probe polarization is not $\phi = \pi/4$. This can be adjusted with the $\lambda/2$ waveplate, but polarization spectroscopy is limited by offset drift, due to changes in temperature of the polarization optics and the windows of the cell. The offset has an RMS drift of ~ 0.8 MHz per hour.

Details of the behaviour of the error signal gradient and amplitude can be

found in [87]. In brief, both saturate with the pump beam intensity, and the gradient begins to decrease at high intensity as power broadening becomes important. A large error signal amplitude means that the lock will be more robust against large frequency perturbations, and a large gradient means that the lock will be "tighter", i.e. the locked frequency fluctuations will be smaller.

The frequency axis for the error signal shown in fig. 2.7(b) can be calibrated by performing simultaneous saturated absorption spectroscopy, "sat-spec", on the $5s^2\,{}^1S_0 \rightarrow 5s5p\,{}^1P_1$ transition in a strontium thermal beam machine. An example of such a sat-spec with the Doppler-background subtracted is shown in the upper frame of fig. 2.7(b). The fit is a sum of six Lorentzians, one for each isotope and hyperfine component of strontium, and since the isotope shifts and hyperfine splittings are known (see table A.3) this enables a calibration of the frequency axis. For more details on this technique see [90]. In standard operation, when pol-spec is being used to stabilize the cooling laser, the frequency calibration is not performed, and in general the thermal beam machine is not used in the experiment.

As a final interesting point, pol-spec in the alkaline earth metals is different to pol-spec in the alkali metals. In the latter the circular birefringence arises from two distinct mechanisms. At high intensity the pump beam saturates the transition to one of the Zeeman sublevels, as described above. At low pump intensity ground state population is transferred amongst the Zeeman sublevels through optical pumping. In this case the different circular-polarization components of the probe beam do not couple equally, leading to the circular birefringence. This can actually lead to the error signal changing sign with increasing pump intensity [91, 92]. The bosonic isotopes of the alkaline earth metal elements have a unique ground state, so the birefringence is uniquely caused by saturation.

2.3 Measurement techniques

There are several quantities that must be measured in our experiment. The population of the cold, trapped gas must be known, which is calculated by measuring the fluorescence from the atoms. To detect atoms in a Rydberg state ionization is recorded, for which a micro-channel plate (MCP) detector is used.

The cooling laser is frequency stabilized, as previously mentioned, however the light for the Rydberg transition is not, and the frequency of this light must be monitored. We use a wavemeter[7] to record the wavelength of the lasers. A portion of the laser fundamental light is coupled into the wavemeter with a multi-mode fibre, and the measured wavelength is converted into a doubled frequency in analysis[8]. Use of the wavemeter will be further discussed in chapter 3.

The data from all of these methods must be recorded, for which we use a computer control program. The control program also executes the timing sequences necessary to perform complex experiments on our cold atoms.

2.3.1 Fluorescence measurements

There are two devices for monitoring the fluorescence from the ground state atoms (from which the trap population can be derived): a home-built amplified photodiode, and a CCD camera[9].

The photodiode enables us to gather time-resolved information about the MOT population. The signal from the photodiode is recorded on a digital

[7] HighFinesse/Ångstrom WS7 super-precision wavelength meter.

[8] The wavelength of the lasers that excite the inner valence electron (chapter 5), is measured *directly*.

[9] pco. "PixelFly qe" digital 12 bit CCD camera.

oscilloscope[10], which is read by the control program. The photodiode sits at the end of a sealed 1:1 telescope, focused on the centre of the chamber (the position of the cold atoms), and has an aperture in front of it to further reduce stray light.

The CCD camera takes spatially-resolved images of the MOT. These images can not only be used to calculate the population of the trap, but also the size, density and position of the trap. The CCD camera is mounted to a sealed 1:1 telescope with an aperture. Extensive tests were performed to ensure the linearity of the camera response. The camera trigger time and exposure length is controlled by the control program. The exposure length is typically 40 μs. The data from the camera is recorded directly by the control program.

The camera has a pixel size of 6.45×6.45 μm, and a total chip size of 1392×1024. The efficiency of the camera was found to be 0.132 ± 0.006 counts per pixel per photon, with a shot-to-shot variation of 0.32%. There is a delay of 7.2 μs between the trigger sent to the camera and the start of the exposure.

2.3.2 Ion detection

The MCP detector is mounted inside the vacuum system, and used to detect ions. The detector sits $\sim$ 10 cm from the position of the cold atoms, and ions are directed to it with the electrodes mounted inside the main chamber.

The high-voltage input electrode of the MCP is held at -2 kV, and the anode is at 100 V. We measure a dark count of 34 ± 2 counts s^{-1} under these operating conditions. The MCP is covered by a home-made wire mesh, which can be supplied with a voltage. This enables a higher ion collection efficiency.

The MCP is connected directly to a pre-amplifier (pre-amp) system (see fig. B.1 in appendix B). A single event recorded on the MCP detector after

[10] Tektronix DPO 4054 Digital Phosphor Oscilloscope.

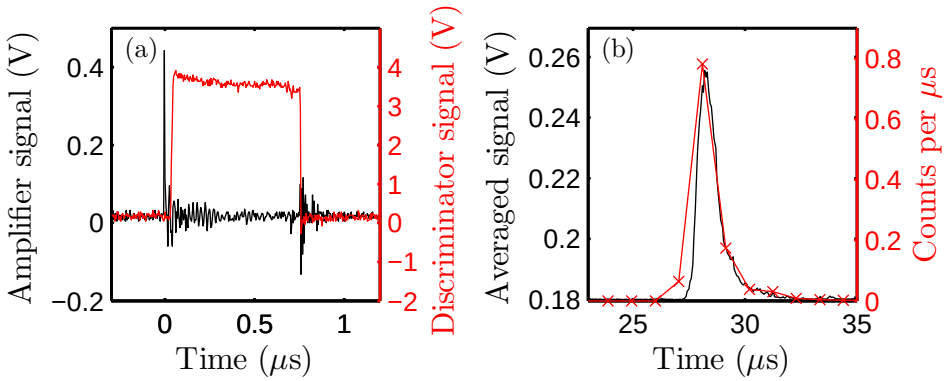

Figure 2.8: (a) Signal due to a single event detected by the MCP, after passing through the discriminator circuit, recorded directly on the oscilloscope. The black trace is taken with just the second stage amplification. The red trace includes the discriminator section. (b) Processed data for a burst of ions detected by the MCP. The black trace is the signal from the second stage amplification averaged 100 times. The red trace is the same data recorded by counting the number of pulses from the discriminator every microsecond.

passing through the pre-amp produces a negative voltage spike with a width of ~ 5 ns, with an amount of ringing.

The pre-amp is connected to a circuit that has an additional second stage of amplification, followed by a discriminator, which can be bypassed. The amplification stage of the discriminator circuit inverts the signal from the pre-amp, amplifies by a factor of 5, and includes an offset. If only the second stage amplifier is use, then the signal is recorded and averaged on the digital oscilloscope. An example is shown as the black trace in fig. 2.8(a).

The discriminator outputs a pulse once it detects a signal of a certain height (which can be chosen), as shown in the red trace in fig. 2.8(a), The pulse has an amplitude of approximately 0.3 V, is 750 ns long, and trails the input signal by 30 ns. Hence, the period between input signals must be greater than 780 ns for the circuit to register separate events. The discriminator therefore saturates when there are a large number of events in a short period of time, whereas the second stage amplifier signal will only saturate if the

MCP detector itself saturates. If the discriminator is used then the signal is recorded directly by the control program, and the program counts events.

The difference between the ion signals recorded by the second state amplifier (averaging) and discriminator (counting) is illustrated in fig. 2.8(b). Excepting fig. 2.8, all of the data presented in this thesis uses the averaging technique.

2.3.3 Computer control

The experiment is run under a large degree of automation. All of the computer control is carried out in the LabVIEW development environment[11]. The control is via a Field-Programmable Gate Array (FPGA) card[12], in which a user reconfigurable FPGA controls all of the digital and analogue input and output lines. The card has 8 analogue inputs, 8 analogue outputs, and 96 configurable digital input/output lines. It has a maximum time resolution of 25 ns.

The code is broadly split into two regions: a highly time-stable region that is written directly onto the FPGA card; and a region which runs on the computer, and uses the computer processor clock.

The FPGA region controls all of the outputs, and can be used to count individual events from the MCP discriminator circuit, if operating in that mode of detection. There are a series of digital TTL output signals, that control the switching of acousto-optic modulators (AOMs), and the triggering of various devices (such as function generators, the CCD camera, and the digital oscilloscope). In some experiments a digital input is used to trigger the card. An analogue output is used to control laser frequencies, as will be discussed in detail in chapter 3. Tests have been done in which the FPGA

[11] National Instruments LabVIEW Professional Development System version 8.5.

[12] NI7831R Reconfigurable I/O Device.

card is used to generate analogue voltage ramps, but in general these are created by other devices, which are triggered by the FPGA card.

The region that runs on the computer is used for operations where the time stability is less vital, namely collecting data. Signals from the MCP (when not being used in the event counting mode) and photodiode are recorded by the digital oscilloscope, and this oscilloscope is under the control of LabVIEW. This enables remote control of any averaging performed on the oscilloscope, and transfer of the signals to the computer. The CCD camera images are recorded and analyzed by LabVIEW, and various operational parameters are set, namely the exposure time, exposure type, and bin size. This region of the code also records data from the wavemeter.

2.4 A cold gas of strontium

Strontium atoms, which are slowed by the Zeeman slower, are captured in a magneto-optical trap (MOT), as shown in fig. 2.9(a). In the MOT three orthogonal pairs of counterpropagating laser beams provide a three-dimensional frictional force, or "optical molasses" [93]. The addition of a quadrupole magnetic field, and circularly polarized MOT beams, turns this frictional force into a trap. The MOT is the building block of experimental cold atomic physics, and will not be further discussed here, though more information can be found in many standard textbooks, for example [94].

For our experiment the MOT beams are red detuned by 60 MHz from the $5s^2\,{}^1S_0 \rightarrow 5s5p\,{}^1P_1$ transition, and have a $1/e^2$ waist of 6.35 mm parallel to the optical bench, 4.44 mm perpendicular to the bench. By recording the flourescence of the ground state atoms on the CCD camera, the size of the MOT can be measured. We find that our trapped atom cloud has a typical Gaussian standard width of ~ 300 μm.

By measuring the fluorescence from the ground state atoms, due to the MOT

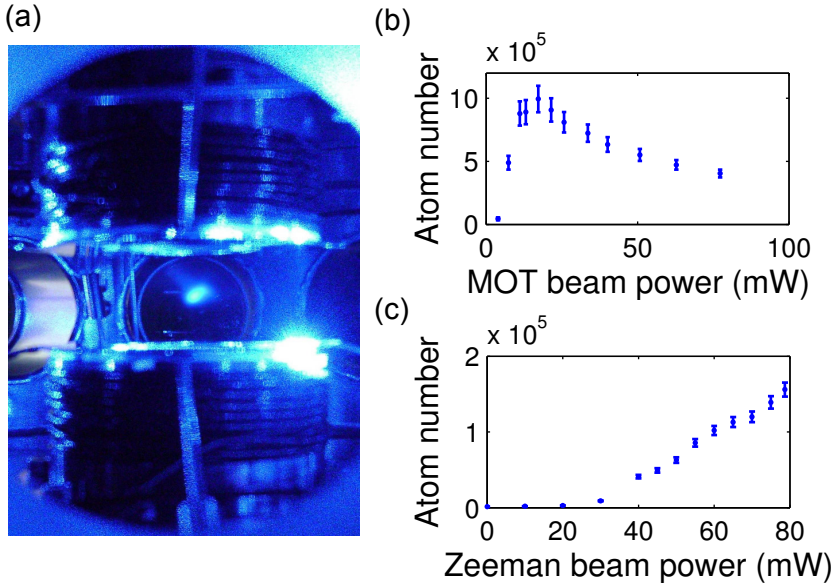

Figure 2.9: (a) A photograph of ~ 2 million atoms at ~ 6 mK trapped in a cloud ~ 1 mm in diameter, fluorescing at 461 nm. (b) The variation in the population of the MOT with the power in the MOT beams. (c) The variation in the population of the MOT with the power of the Zeeman slower beam.

beams (see fig. 2.9(a)), the number of ground state atoms can be measured. This number depends upon many parameters, such as the detuning and power of the MOT and Zeeman slower beams, the temperature of the oven, and the size of the trapping magnetic field. We thoroughly studied these dependencies, and optimized the parameters accordingly.

The variation of the trapped population with the power in the MOT beams is shown in fig. 2.9(b). The power referred to is the *total* power, before the beam is split into three. The trap population initially increases with MOT beam power, begins to plateau, then *decreases* at higher power. The population in the trap (for a constant trapping volume) is governed by the competition between the capture velocity and loss rate of the MOT [61]. The loss rate increases, and eventually saturates, with beam intensity. The capture velocity, however, increases at first as the trapping potential increases, but eventually begins to decrease as the atomic transition becomes power

broadened. In this regime the atoms cannot distinguish between the radiative forces of each beam in a counterpropagating pair, reducing the frictional force and hence the capture velocity [95]. At this point, the trap population begins to decrease, as seen in fig. 2.9(b).

The trapped population increases with the power in the Zeeman slower beam, as shown in fig. 2.9(c). There is a threshold since atoms have to be slowed to at least the capture velocity of the MOT. After this, increasing the Zeeman slower beam power slows an increasing fraction of the atoms to below the capture velocity, and the population of the MOT will increase.

The number of atoms in the trap increases exponentially with the temperature of the oven. This is expected since the vapour pressure of the strontium metal increases exponentially with temperature. The number of atoms in the trap increases with the size of the magnetic field gradient (which is proportional to the current that drives the coils), which is expected for modest (< 100 G cm^{-1}) field gradients [96]. The limit to the gradient we use is the amount of current that is safe to put through the MOT coils, considering that they are uncooled. We limit this to a normal operational current of 2.5 A.

To measure the decay rate of atoms from the MOT, the Zeeman slower beam is switched off (the loading of the trap is stopped), and the time-variation of the flourescence from the atoms due to the MOT beams is recorded. This yields a typical trap lifetime of 13 ms. This lifetime is limited by the decay of population to the meta-stable $5s5p\,^3P_2$ state via the $5s4d\,^1D_2$ state [97] (see fig. 2.10). The $5s5p\,^3P_2$ state has a lifetime of 13 minutes [98], and so any population that ends up here is lost from the trap. It is a subtle point, but the limit is not the decay of population to the $5s4d\,^1D_2$ state *per se*, because 66% of the population in this state decays to the $5s5p\,^3P_1$ state, which then decays to the ground state, and can re-enter the trapping cycle.

The temperature of the atoms in the MOT is measured using a time-

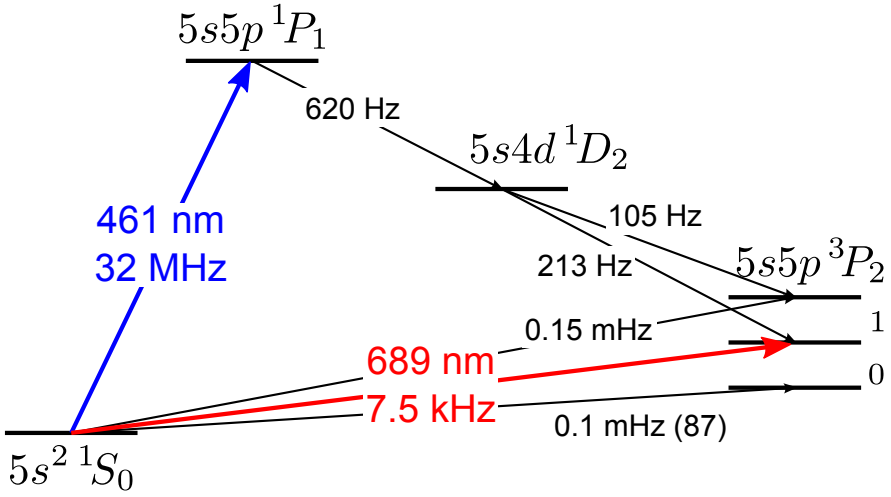

Figure 2.10: A simplified energy level diagram for strontium. The main cooling transition is $5s^2\,^1S_0 \rightarrow 5s5p\,^1P_1$. There is the potential for further cooling via the spin-forbidden $5s^2\,^1S_0 \rightarrow 5s5p\,^3P_1$ transition.

of-flight measurement [99], where the ballistic expansion of the cloud of atoms, once released from the trap, is analyzed. For a MOT beam detuning/power of -71.2 MHz/63 mW and a Zeeman slower beam detuning/power of -519.7 MHz/70 mW the average temperature of the atoms is 5.9 ± 0.5 mK. This is considerably hotter than the Doppler cooling limit of 0.77 mK. It has been found that this theoretical limit isn't reached even at very low MOT beam intensities [61]. This study states that standard Doppler theory underestimates the heating rate in the MOT, possibly by not taking into account standing wave effects, and there has been some work confirming this as a likely additional heating mechanism [100].

Temperatures of mK are not particularly low as cold atom experiments go. For example, in rubidium temperatures of a few hundred μK are reached by cooling on the D2 line. The reasons for this difference in temperature are various. The linewidth of the $5s^2\,^1S_0 \rightarrow 5s5p\,^1P_1$ transition in strontium is $2\pi\times32$ MHz, compared with $2\pi\times6$ MHz for the D2 line in rubidium. A larger linewidth leads to a higher Doppler cooling limit, as photons are scattered at a greater rate. Also, for atoms with hyperfine structure in the ground

state, sub-Doppler cooling mechanisms further cool the gas [73], a process not possible in ^{88}Sr due to its lack of nuclear spin (although sub-Doppler cooling does occur in ^{87}Sr [61]).

As previously mentioned, the population in the strontium MOT can only be lost from the cooling cycle if the atoms end up in the $5s5p\,^3P_2$ state. This happens at a rate of $\sim 1.29 \times 10^3$ s^{-1} [61], which is small compared to the cooling transition rate of 2.0×10^8 s^{-1}. Hence, strontium can be cooled and trapped with the single laser, at 461 nm, without need for a re-pumping laser. There are several possible re-pumping schemes in strontium, which typically increase the population of the MOT by a factor of ~ 10, and the lifetime by a factor of ~ 7 [101]. For the experiments reported in this thesis the increase in population and lifetime was not considered of necessary importance considering the added complexity of including extra lasers.

Conclusion

We have a robust and reliable apparatus for creating a cold gas of strontium atoms. The apparatus is extremely flexible, for example it will be physically (if not technically) simple to add an additional stage of cooling in the form of a second MOT operating on the $5s^2\,^1S_0 \rightarrow 5s5p\,^3P_1$ intercombination transition (see fig. 2.10). Another long term plan involves mounting lenses inside the main chamber for creating a microscope for the dipole blockade effect (see section 1.2) or creating an optical lattice.

Another extension that may be made is the replacement of the oven with a source of pre-cooled strontium. This would take the form of a dispenser loaded "pyramid MOT" [102], with a hole in the apex of the pyramid to transfer the cold atoms to the main chamber [103]. By removing the large, hot source of atoms (the oven) from the experiment there would neither be hot atoms or large amounts of black-body radiation reaching the position of the cold trapped atoms. This would be extremely useful for experiments in the

field of precision frequency metrology (see section 1.4) using strontium, since black-body radiation is a source of measurement uncertainty [67]. Black-body radiation also redistributes population amongst Rydberg states [104], and so this source would lead to cleaner Rydberg gas experiments.

In the next chapter it will be shown that the apparatus described here can be used for more than just creating a magneto-optically trapped cloud of strontium. It forms the basis for studying a cold gas of Rydberg atoms.

Chapter 3

Spectroscopy of a cold Rydberg gas of strontium

Introduction

We study a cold, trapped gas of strontium containing many atoms excited to a Rydberg state. Due to the many-body nature of this system, there can be many complicated interaction effects, such as the redistribution of atoms between different energy and angular momentum states [58], ionization, and the formation of a cold plasma [105]. Performing Rydberg state spectroscopy is an essential first step in understanding these phenomena.

All previous studies of Rydberg states in strontium have used a hot gas [106–115]. In general, the Rydberg states were detected through laser excitation followed by field ionization. We also performed a study in a hot beam [90], using electromagnetically induced transparency to detect atoms in the Rydberg state [116].

In this chapter a completely different spectroscopic approach is presented, in the first ever study of Rydberg states in cold strontium. The Rydberg atoms are detected through spontaneous ionization, a method sensitive to even minimally populated states. We have located many Rydberg series by

measuring this ionization, and have developed a high resolution "step-scan" technique to acquire spectra.

To understand the interactions in a Rydberg gas the transition dipole matrix-elements between various states must be known, and their calculation will be discussed in chapter 4. The spectroscopic technique presented in this chapter enables us to verify our calculations.

This chapter will:

- Discuss the **spontaneous ionization** of a Rydberg gas, which provides our spectroscopic signal, in section 3.1.
- Present the results of **exploratory spectroscopy** in section 3.2.
- Present our method of **high resolution spectroscopy**, the "step-scan" technique, in section 3.3.

3.1 Spontaneous ionization

Most experiments studying Rydberg atoms in cold gases have observed some degree of spontaneous ionization. There are several possible mechanisms to explain the ionization. These include collisions between hot and cold Rydberg atoms, blackbody photoionization [105], photoionization by the amplified spontaneous emission (ASE) of pulsed laser sources [58], and the van der Waals interaction between the Rydberg atoms [117]. We do not, in general, use a pulsed laser in this experiment, so ASE can be ruled out immediately.

Collisions between hot and cold Rydberg atoms have been shown to be a significant, but not sole, contributor to the initial ionization of a cold Rydberg gas [118]. The cross-section for collision between two atoms in states n_1, n_2 scales as $n_1^2 n_2^2$ [118]. Hence, Rydberg-Rydberg collisions will be the dominant collisional ionization mechanism, presuming the *ionizing* collision

cross-section is proportional to the total collision cross-section. "Hot" Rydberg atoms could be present in our experiment. When the Zeeman slower beam is switched off there is a tail of slowed atoms that travels towards the cold atoms which are already loaded into the MOT. A fraction of these slowed atoms could be resonant with the two step excitation to the Rydberg state.

Next, photoionization by blackbody radiation (BBR) is considered. To accurately calculate the photoionization rate it is necessary to consider the fact that BBR redistributes population amongst the Rydberg states [119]. An approximate formula for the BBR induced photoionization rate $1/\tau_{BB}$ is [26]:

$$\frac{1}{\tau_{BB}} = \frac{4\alpha^3 k_B T}{3\hbar n^2}, \tag{3.1}$$

where α is the fine structure constant, and T the temperature in Kelvin. This expression is the total depopulation of the Rydberg state due to BBR, not just photoionization, and so sets an upper bound on the photoionization rate. This formula suggests that at $n = 20$, $\tau_{BB} \approx 20$ μs at 300 K. We observe spontaneous ionization within 1 μs of creating Rydberg atoms, so BBR cannot be playing a large initial ionization role in our experiment. Other research has found that, at high principal quantum number $n > 20$, the spontaneous ionization rate is too high to be explained by BBR induced photoionization [56].

Even though the ground state atoms are cold, and essentially do not move on the times scales of most Rydberg gas experiments (a "frozen Rydberg gas"), long-range attractive van der Waals interactions have been shown to cause cold Rydberg atoms to collide and ionize rapidly through Penning ionization. Ionization can be caused by atoms interacting on an attractive or repulsive potential [120], and the level of Penning ionization can be tuned by varying the size and sign of the interaction [121].

The time τ taken for two initially stationary atoms, separated by R_0, to collide can be estimated as $\tau \simeq 0.2156 R_0^4 (2C_6/m_{Sr})^{-1/2}$ [120], where C_6 encodes the interaction strength. Using the results that will be presented in chapter 4, this leads to an ionization time of $\tau \simeq 0.5$ μs for two atoms in a $50\,^1S_0$ state, at our typical Rydberg densities. This is fast enough to explain our observations. The interaction strength C_6 scales as n^{11}, hence the rate of ionization due to interaction induced collisions will rapidly decrease as n decreases. Interaction induced ionization cannot explain the rapid spontaneous ionization at lower n.

There are other spontaneous ionization mechanisms that may be relevant in our experiment. The lasers we use for the Rydberg excitation have wavelengths of 420 nm and below, so there is a possibility of Rydberg ionization by photoelectrons created through the photoelectric effect. We see no evidence that the laser beams hit any of the metal in the chamber, it is unlikely that photoelectrons are a major cause of Rydberg atom ionization. There is the possibility for direct photoionization through a multi-photon process. This would cause a non-linear increase in the level of ionization with laser power [122], which we do not observe.

A process that could cause ionization in an alkaline earth metal is excitation of an "autoionizing" resonance. This could occur when the $5s5p \rightarrow 5snl$ Rydberg excitation is close in energy to the doubly excited $5snl \rightarrow 5pnl$ autoionizing transition. The closest states that we excite are $5s5p \rightarrow 5s18s$ and $5s18s \rightarrow 5p_{1/2}18s$ [123], which are detuned by ~ 650 GHz. This may seem like a huge detuning, but the autoionization width is ~ 200 GHz [123], hence the detuning is only ~ 3.2 autoionizing linewidths. This doubly excited resonance may cause ionization in the region around $n \sim 18$, but will not be excited at much higher n. There may be other doubly excited resonances that we have neglected in our analysis.

We observe rapid (< 1 μs) spontaneous ionization for all Rydberg states we

have studied ($n = 18$ and above), including states exhibiting both attractive and repulsive interactions. The driving process is most likely a mix of collisions between hot and cold Rydberg atoms, interaction enhanced collisions, black body ionization, and some autoionization at lower n. The presence of spontaneous ionization is a spectroscopic signature that Rydberg atoms have been created.

3.2 Exploratory spectroscopy

In this section, a simple method for performing spontaneous ionization Rydberg spectroscopy is presented. The ground state atoms are continuously loaded into the magneto-optical trap (MOT) from the Zeeman slowed beam, and continuously excited to the Rydberg state. By scanning the frequency ω_2 of the Rydberg excitation laser λ_2, and monitoring ionization from the gas, Rydberg states can be located. This exploratory method will be referred to as the "scanning" technique.

Method

The general set-up for the creation and study of a Rydberg gas in our experiment is shown in fig. 3.1(a). The atoms are excited to the Rydberg state through a two step excitation $\lambda_1 + \lambda_2$, as shown in fig. 3.1(c). In these scanning experiments the first step λ_1 is provided by the MOT trapping beams. The laser $\lambda_2 = 413$ nm drives the second step, with a typical power at the chamber of $\sim$ 2.6 mW, and a $1/e^2$ beam waist of 0.8 mm parallel to the optical bench, 0.4 mm perpendicular to the bench.

A function generator sends a continuous pattern of voltage pulses to the electrodes to direct charge to the micro-channel plate detector (MCP). The field geometry is that shown in fig. 3.1(b), with an applied voltage of ± 10 V, which corresponds to a field of 4.2 ± 0.1 V cm^{-1} at the position of the cold

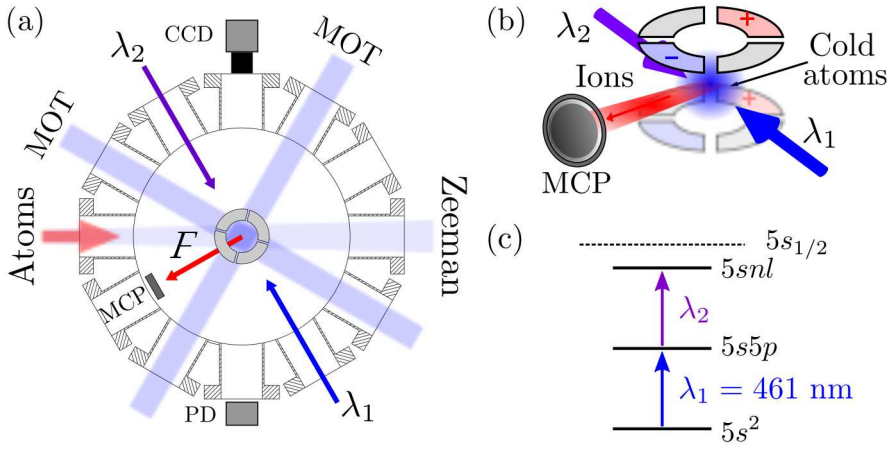

Figure 3.1: (a) Diagram of the main chamber and key elements for Rydberg state spectroscopy. Zeeman slowed atoms enter from the left, and are trapped in a MOT. Ions are directed to the MCP by an electric field F. A CCD camera and photodiode (PD) measure fluorescence from the MOT. (b) Schematic of the electrodes, illustrating the electric field configuration used to direct ions to the MCP. The unmarked electrodes are grounded. (c) Level scheme. Atoms are excited to the $5snl$ state through two-step excitation $\lambda_1 + \lambda_2$.

atoms. The pulses are 10 μs long, and have a period of 100 μs. In these experiments the MCP grid is held at -10 V to increase the ion collection efficiency.

The frequency ω_2 is scanned by applying a ramp of voltage to the piezo on the feedback grating of the diode laser λ_2. The frequency of the laser and the level of spontaneous ionization are simultaneously recorded. The laser $\lambda_2 = 413$ nm can be scanned by ~ 8 GHz before the laser cavity locking electronics cannot track the scan, and the laser unlocks.

Spectroscopy

Some example spontaneous ionization spectra, acquired using the simple scanning technique, are shown in fig. 3.2. The effective quantum number

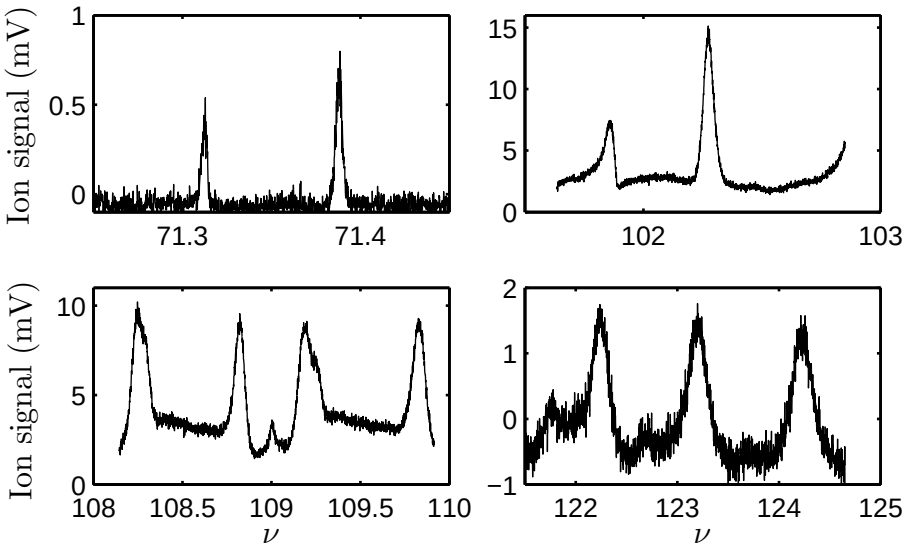

Figure 3.2: Spontaneous ionization spectra of various Rydberg states, acquired with the scanning technique. The laser frequency is converted to effective quantum number ν through eqn. (3.2). Individual lines are clearly visible over $\nu = 100$ using this scanning technique. Note, the MCP electronics create a small negative voltage offset.

ν is used to label the spectral position[1], as it indicates the region of the Rydberg series in which a state lies. The effective quantum number is defined through:

$$\nu = \sqrt{\frac{R_{\mathrm{Sr}}}{\mathrm{E_{ion}} - \mathrm{E}}}\,, \tag{3.2}$$

where R_{Sr} is the Rydberg constant for strontium, $\mathrm{E_{ion}}$ is the ionization threshold (see table A.1), and E is the energy of the laser excitation $\lambda_1 + \lambda_2$.

The signals are averaged 256 times on the digital oscilloscope. In analysis the data is binned to account for the pulsed electric field. Individual lines are clearly discernible at $\nu \simeq 125$, which corresponds to 211 GHz below the

[1] In this thesis two symbols are used to define the effective quantum number: ν is a continuous variable, that does not necessarily label a state; n^* is the effective number of a specific state, as defined through its quantum defect.

ionization threshold.

The electric field that is applied to direct the ions to the MCP can directly ionize the Rydberg atoms. The classical expression for the electric field F_c required to ionize an atom in a state of principal quantum number n is [26]:

$$F_c = \frac{R_{Sr}^2}{4kn^4}\,, \tag{3.3}$$

where $k = 1/(4\pi\epsilon_0)$, with ϵ_0 the permittivity of free space. This formula indicates that states of $n \gtrsim 100$ will be ionized by a field of 4.2 $\mathrm{V\,cm^{-1}}$.

The potential for field ionization explains why the absolute size of the signal above $\nu \simeq 100$ is larger than the signal around $\nu \simeq 71$, as the field ionization signal will add to the spontaneous ionization signal. In the region $\nu > 100$ there is clearly a non-zero background signal, which isn't present lower in the Rydberg series. The presence of a small background stray field (see section 4.2.1) allows excitation of states in the high angular-momentum manifold, which makes the spectrum quasi-continuous.

3.2.1 Quantum defect analysis

We have used the scanning technique to perform Rydberg state spectroscopy over a large range of n. A useful way of displaying this information is through a quantum defect plot, as shown in fig. 3.3. Each Rydberg series has a distinct quantum defect δ. The quantum defect of a state of effective quantum number n^* (as defined through eqn. (3.2), with E the energy of the state) is given by $\delta = n - n^*$. Since n is an integer $\delta \pmod 1 \equiv n^* \pmod 1$. Hence, by plotting $\delta \pmod 1$ against n^* the spectral lines will be separated into their different series, which is evident in fig. 3.3.

At high $n \gtrsim 90$ the series structure is lost, most likely due to stray electric field perturbing the energy level structure. There is evidence that some high

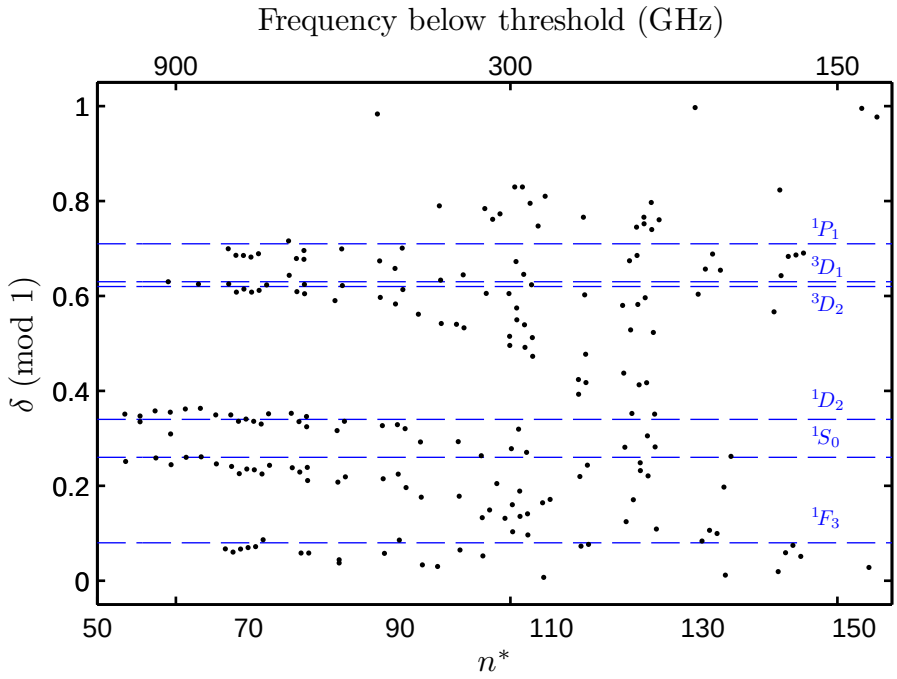

Figure 3.3: A quantum defect plot for the Rydberg series of strontium. The quantum defect δ of the state (mod 1) is plotted against the effective quantum number n^*. The blue lines mark quantum defects from the literature [109, 111, 115].

angular momentum states are excited, with points around $\delta = 1 \equiv 0$ (mod 1). High angular momentum states have quantum defects close to 0 in value, and the appearance of these states on the quantum defect plot supports the assumption that a stray field is present (see section 4.2).

It should be noted that at high n it becomes more difficult to define which observed spectral features are distinct lines. This, and the absolute frequency uncertainty of the wavemeter, will cause some of the spread in the data.

Limitations of the scanning technique

There are several major limitations of the scanning technique. Firstly, the frequency axis is not stable. The ionization signal must be averaged for ~ 2.5 minutes to produce enough signal-to-noise, and in this time the centre

frequency of the laser can drift by ~ 20 MHz, which will broaden the observed spectral features.

Another complication is due to the loading of the MOT during the Rydberg excitation, leading to complex population dynamics. This distorts the shape of the resonances. The ion detection electric field pulses will stark shift the Rydberg state for short bursts of time, since the Rydberg excitation is continuous, which will broaden the spectral features.

Despite the limitations of this scanning technique, it has yielded valuable information. We have located lines belonging to many different series, and it is an extremely fast method for gathering data over a large spectral range. In particular, we have located Rydberg states of the $^1S_0$ and $^1D_2$ series, and these states are studied throughout this thesis. The next section will discuss a cleaner, more precise method for performing Rydberg spectroscopy.

3.3 High-resolution spectroscopy

The cold atoms can be excited to the Rydberg state whilst free from the MOT. This removes any complexities due to the continuous refilling of the trap, or the presence of the MOT magnetic field and trapping beams.

A "probe" beam, resonant with the $5s^2\,{}^1S_0 \rightarrow 5s5p\,{}^1P_1$ transition, provides the first step $\lambda_1 = 461$ nm in the two-step Rydberg excitation shown in fig. 3.1(c). The probe beam arrives at the chamber via an optical fibre, and has a $1/e^2$ waist of 0.86 mm. By using a probe beam resonant with the atomic transition, as opposed to the detuned MOT beams, a greater number of atoms can be excited to the Rydberg state.

The second step λ_2 is made using light at 420 nm or 413 nm[2]. The beams λ_1 and λ_2 are counterpropagating, as shown in fig. 3.1(a). Both beams are

[2] The size and typical power in these beams are given in chapter 5.

linearly polarized perpendicular to the optical bench, propagate normal to the direction of the electric field at the position of the atoms, and are larger than the trapped atom cloud. Both λ_1 and λ_2 are simultaneously pulsed using acousto-optic modulators (AOMs), with a pulse length of 4 μs. By using a short pulse of light it is known exactly when the Rydberg excitation is made, and upon how many ground state atoms.

A fraction of the Rydberg atoms spontaneously ionize, and the ions are directed to the MCP using a subsequent 4 μs long, 4.2 V cm^{-1} pulse of electric field. In these experiments the MCP grid is held at -40 V to maximize the ion collection efficiency.

External laser frequency control

The laser from which the resonant probe beam λ_1 is derived is frequency stabilized, via polarization spectroscopy [87] in the dispenser cell [74], as discussed in section 2.2. The Rydberg excitation laser λ_2 is *not* frequency stabilized, instead its frequency is varied through application of a voltage to the diode laser feedback grating piezo. Since, in this section, the lasers are pulsed, the frequency is *stepped*, not scanned.

In figs. 3.4(a) and (b) a voltage is applied to the laser $\lambda_2 = 413$ nm, in increasing steps of 0.5 mV every second, and the frequency is recorded on the wavemeter. This step size is close to the minimum output voltage resolution of the computer control program (0.3 mV). Figure 3.4(a) shows that a linear ramp of voltage produces a linear ramp of frequency. Figure 3.4(b) is a close up on the frequency ramp, showing that the individual steps can be resolved. In this particular example the average step size is 2.2 MHz, determined by fitting a straight line to the data in fig. 3.4(a). By studying a range of different step sizes the voltage-to-frequency calibration factor is found to be 4.4 ± 0.1 MHz mV^{-1}.

It is important to know if measurements taken by the wavemeter have a

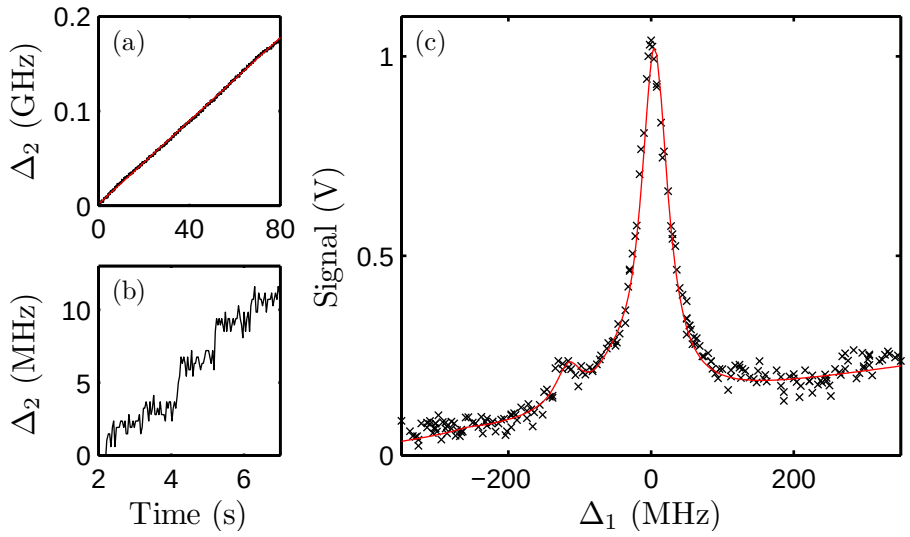

Figure 3.4: (a) Variation in the detuning Δ_2 (black points) of the 413 nm laser from an arbitrary frequency, as a voltage ramp of 0.5 mV s^{-1} is applied. The red line is a linear fit. (b) A close up of the linear ramp in (a). Individual frequency steps of ~ 2 MHz are resolved. (c) Sat-spec (black crosses) acquired by stepping the frequency ω_1 of the 461 nm laser across the $5s^2\,{}^1S_0 \rightarrow 5s5p\,{}^1P_1$ transition. The detuning Δ_1 is from our measured transition frequency. The data is fit with a sum of six Lorentzians (red line).

good *relative* accuracy, i.e. if the wavemeter accurately measures the size of the frequency steps. To test this accuracy saturated absorption spectroscopy [124] ("sat-spec") was performed in the dispenser cell [74], with the result shown in fig. 3.4(c). The frequency ω_1 of the 461 nm laser is stepped across the $5s^2\,{}^1S_0 \rightarrow 5s5p\,{}^1P_1$ transition, which has a linewidth $\Gamma = 2\pi \times 32$ MHz. The resulting spectrum is fit with a function $\sigma(\omega_1)$, which is a sum of six Lorentzians, one for each isotope and hyperfine component of Sr [90]:

$$\sigma(\omega_1) = \left[\sum_{\mathrm{i}=1}^{6} A\left(\frac{(\alpha\Gamma)^2 I_{\mathrm{i}}^a}{(\alpha\Gamma)^2 + \left(\omega_1 - (\alpha I_{\mathrm{i}}^s + \omega_0)\right)^2}\right)\right] + B\omega_1\,, \tag{3.4}$$

where i labels the isotope/hyperfine component. The free parameters of this equation are an overall amplitude A, a frequency axis scaling α, the ^{88}Sr tran-

sition frequency ω_0, and a parameter that allows for a sloping background B. The parameters I_{i}^a and I_{i}^s are the relative abundance and shift for isotope/component i, respectively. These properties are known (see table A.3), and are fixed in the fit.

If the relative frequency measurement accuracy of the wavemeter is perfect, then the frequency scaling parameter $\alpha = 1$. Essentially, the test is that the wavemeter can reproduce the isotope shifts. The fit to the sat-spec in fig. 3.4(c) returns a value of $\alpha = 1.03 \pm 0.02$, meaning that the relative accuracy of the wavemeter can be trusted to the few percent level.

The method of performing spectroscopy by stepping the frequency of the laser will be referred to as the "step-scan" technique. By measuring the frequency at each step, long-term laser frequency drifts are not a problem. The only issue is with frequency drift *within* a step, but this is small, as can be seen in fig. 3.4(b). The noise within a step is a combination of the wavemeter measurement noise, and the voltage noise from the computer control program (~ 150 μV r.m.s.).

Absolute frequency accuracy

It is important to recognize the limitations on the *absolute* frequency accuracy when using the wavemeter. When comparing the state energies we measure to values in the literature there are discrepancies of the order 200 MHz. This is consistent with the wavemeter manufacturer specified absolute frequency accuracy when using a multi-mode fibre.

There are several ways to improve this accuracy, such as to use a single-mode fibre, or to continuously calibrate the wavemeter to a state with known energy. However, it is not our aim to accurately determine state energies, rather it is the *relative* accuracy that is important to us, so that state splittings and spectral features can be measured. Figure 3.4(c) indicates that the relative accuracy is good.

3.3.1 The step-scan technique

Rydberg state spectroscopy is performed using the step-scan technique in the following way. First, the Rydberg excitation laser λ_2 is set to a frequency ω_2, and the two step excitation $\lambda_1 + \lambda_2$ is made. This will be referred to as the "excitation sequence". Second, the data gathered during the excitation sequence is recorded by the computer control program, and ω_2 is stepped using the step-scan technique. This process is repeated as many times as necessary to cover the desired spectral range.

The excitation sequence

A schematic of the excitation sequence is shown in fig. 3.5(a). The sequence is as follows:

- The atoms are released from the MOT by switching off the MOT magnetic field, MOT beams and the Zeeman slower beam.
- A delay of > 100 μs ensures that the MOT magnetic field has decayed.
- The MOT beams are pulsed for 40 μs, and the resulting fluorescence is recorded with the photodiode.
- The two step, 4 μs long Rydberg excitation is made after a ~ 30 μs delay[3]. This delay accounts for the response of the photodiode.
- The Rydberg excitation is followed (after a 500 ns delay) by a 4 μs long electric field pulse, with an amplitude of 4.2 V cm^{-1}, and the geometry shown in fig. 3.1(b).
- After ~ 30 μs delay, the fluorescence from another 40 μs pulse of MOT light is recorded with the photodiode.

[3] The delays are precisely set, but varied slightly experiment to experiment.

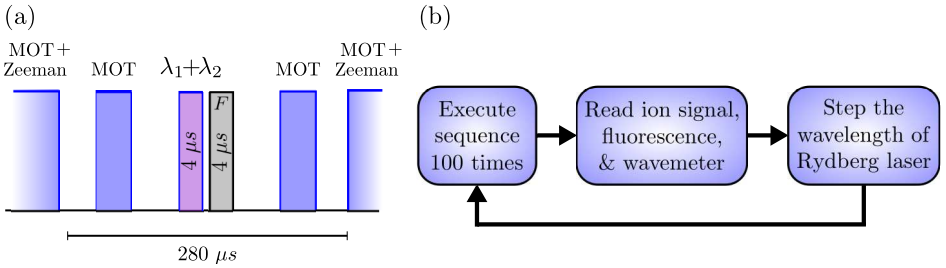

Figure 3.5: (a) Timing diagram for the Rydberg excitation. The MOT light is pulsed on before and after the Rydberg excitation $\lambda_1+\lambda_2$, through which the MOT population, density and any loss is measured. An electric field pulse F follows the Rydberg excitation. (b) Flow diagram for the step-scan technique. The sequence in (a) is repeated 100 times and averaged. Data is subsequently recorded, and ω_2 stepped. This process is repeated to produce spectra.

- The MOT is refilled by switching the MOT magnetic field, MOT beams and Zeeman slower beam back on, after a delay of ~ 30 μs to account for the response of the photodiode. The MOT refills for 7 ms.

This excitation sequence is repeated 100 times, during which the spontaneous ionization and fluorescence signals are averaged on the oscilloscope. The level of fluorescence from the MOT beams is proportional to the ground state population. By making the fluorescence measurement before and after the Rydberg excitation, the number of ground state atoms that are lost due to the Rydberg excitation can be measured. On the final repeat the CCD camera is triggered during the first MOT beam pulse, yielding the ground state atom number and density.

Following the 100 repeats the computer control program reads ω_2 from the wavemeter, taking 100 samples with a period of 1 ms. The mean value of ω_2 is calculated at each step, and the standard deviation gives a measure of the short time-scale noise. This noise is small, as can be seen by the x-error bars on fig. 3.6(a). The averaged ion signal is integrated, to produce an ion signal in units of V μs at each value of ω_2. Once the data has been recorded, the frequency ω_2 is stepped. This process is illustrated in fig. 3.5(b).

3.3.2 Spectroscopy

An example Rydberg spectrum acquired using the step-scan technique is shown in fig. 3.6(a). The laser $\lambda_2 = 420$ nm is stepped in frequency over the $5s5p\,{}^1P_1 \rightarrow 5s18d\,{}^1D_2$ resonance in steps of ~ 2.2 MHz. The corresponding fractional loss of atoms is shown in fig. 3.6(b). Although this "loss spectrum" sits on a non-zero background, there is clearly $\sim 5\%$ of ground state atom loss resonant with the excitation to the Rydberg state. In this region of n the Rydberg state lifetime is much less than the ~ 35 μs delay between the Rydberg excitation and the loss measurement (see section 5.2), so most of the Rydberg atoms will have returned to the ground state. Loss is not due to decay to states other than the ground state [125]. Therefore, the loss spectrum in fig. 3.6(b) must mainly be due to the Rydberg atoms spontaneously ionizing. A discussion of the utility of the loss fraction measurement can be found at the end of this section.

The FWHM of the ion spectrum is $2\pi \times (40.5 \pm 0.4)$ MHz, and the FWHM of the loss spectrum is $2\pi \times (33 \pm 8)$ MHz, which are compatible within errors. The loss fraction data has large error bars since each point is calculated from a small difference between two large numbers, and the photodiode exhibited a lot of ringing.

The ion spectrum FWHM is similar to, but broader than, the natural linewidth of the intermediate $5s5p\,{}^1P_1$ state, $\Gamma = 2\pi \times 32$ MHz. The probe beam power was 0.6 mW when taking this data, which corresponds to an intensity of 0.6 I_{sat}. The power broadened linewidth is $\Gamma' = \Gamma(1 + I/I_{\text{sat}})^{1/2}$, giving $\Gamma' = 2\pi \times 40.5$ MHz, which agrees with the ion spectrum FWHM.

This agreement indicates that, in our experiment, the measured linewidth of the Rydberg state is set by the width of the intermediate state. This observation has been confirmed by many identical measurements over a range of n states. The linewidth of the Rydberg state, if excited directly from the ground state, would be significantly smaller: the linewidth scales as n^{-3} [26].

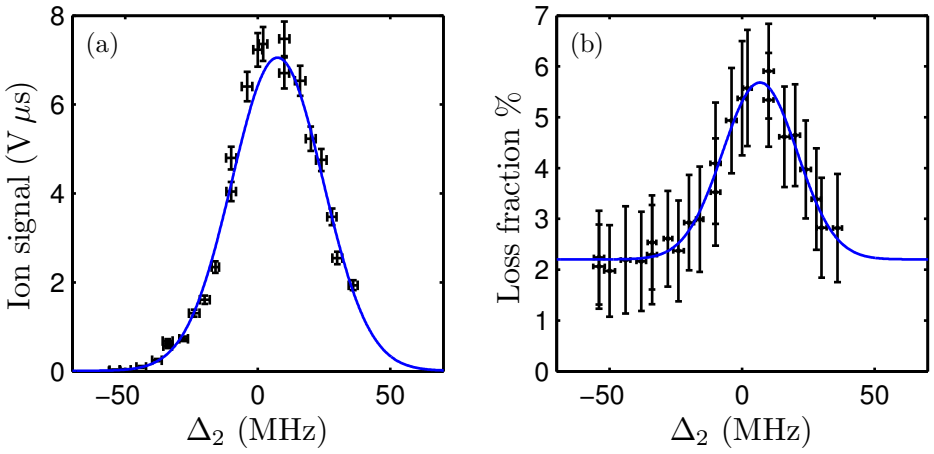

Figure 3.6: (a) Example ion spectrum for the $5s18d\,^1D_2$ state. The signal is the integrated spontaneous ionization signal. The detuning Δ_2 is of ω_2 from our measured line centre. (b) Fractional loss spectrum for the same experiment. The data in both figures is fit with a Gaussian function (blue lines).

For example, we measure the lifetime of the $19\,^1D_2$ state to be $\tau_{19D} = 900$ ns (see section 5.2), which would correspond to a linewidth of $2\pi \times 180$ kHz.

The spectrum of the $18\,^1D_2$ state in fig. 3.6 involved 23 steps of ~ 2 MHz. In fig. 3.7 a step-scan spectrum with 400 steps of ~ 8 MHz is presented. This spectrum is taken in the region of $n = 80$, and during acquisition there is a constant background electric field of 0.35 V cm^{-1}.

The presence of an electric field allows excitation to states that are not accessible from the intermediate $5s5p\,^1P_1$ state in zero-field, (see section 4.2). The only dipole allowed transitions in zero-field are to the $^1S_0$ and $^1D_2$ series. The $^1D_2$ line is clearly the strongest, but the $^1P_1$ state, and its separate $|m_j|$ components, are clearly visible. Triplet states are also visible in fig. 3.7. Transitions to these states are forbidden, but occur in zero-field due to the presence of doubly excited perturbing states [107]. The presence of an electric field will alter the line strength of the triplet states, though will not mix states of different spin. The triplet state lines are surprisingly large at $n = 80$, even in zero electric field, for which we do not have an explanation.

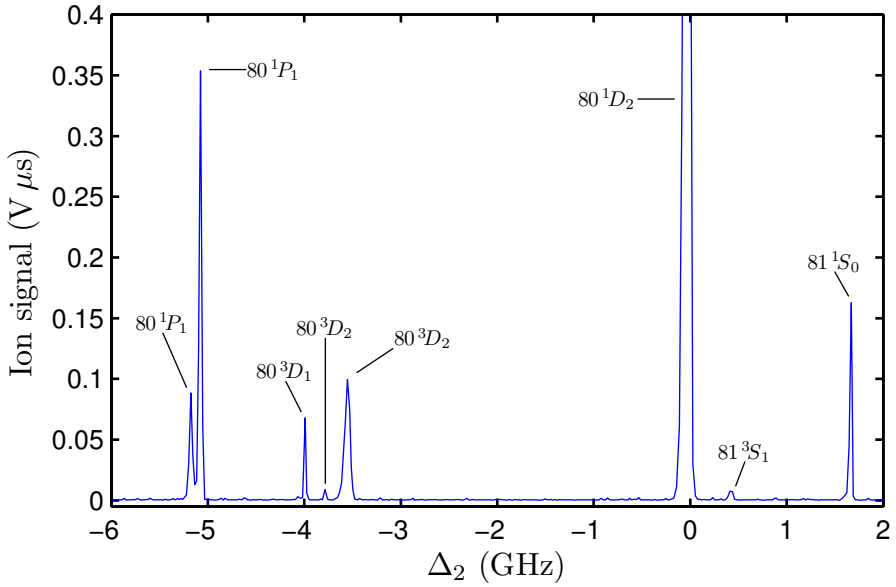

Figure 3.7: Spectrum in the region $n = 80$, in the presence of 0.35 V cm^{-1} of electric field, taken with the step-scan technique. The field has split the $80\,^1P_1$ and $80\,^1D_2$ states into their different $|m_j|$ components. The strongest transition, $80\,^1D_2$, peaks at 1.4 V μs. The lines are assigned using the single electron simulation described in chapter 4. This spectrum is part of the Stark map in fig. 4.3.

The visibility of the forbidden states in fig. 3.7 highlights the sensitivity of the step-scan technique. In the case of the $^3S_1$ peak, it is ~ 150 times smaller than the $^1D_2$ peak. From analysis in chapter 5, the population of the $^1D_2$ state can be estimated to be $\sim 10\%$ of the ground state, which would correspond to $\sim 10^5$ Rydberg atoms. Presuming that the spontaneous ionization signal is linearly proportional to the Rydberg state population, this would suggest that the population of the $^3S_1$ state is less than 10^3.

The states in fig. 3.7 are labeled using the single-electron simulation, which will be presented in chapter 4. A quantum defect analysis can only identify the different series in zero electric field, it requires the simulation to predict the energy positions in an electric field. The step-scan spectroscopy in this section is presented in [12].

Finally, the step-scan technique is compared to the scanning method pre-

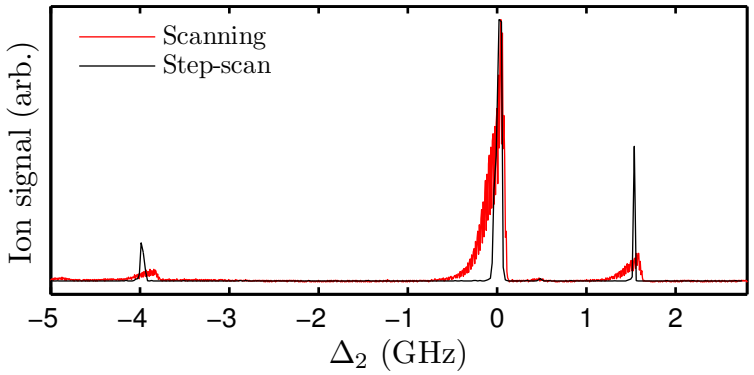

Figure 3.8: A comparison of the scanning technique presented in section 3.2 (red), and the step-scan technique (black). These spectra are taken in the region $n = 80$, with no constantly applied electric field. The amplitude of the two spectra have been scaled for comparison.

sented in section 3.2. In fig. 3.8 a spectrum is taken in the region of $n = 80$, in zero electric field. The step-scan took approximately 10 times longer to acquire than the scanned spectrum.

Although the line positions agree, the step-scan produces much narrower, and hence more precise, features. The lineshapes from the scanning technique are highly asymmetrical, which is not reproduced in the step-scan spectrum. The step-scan technique has better signal-to-noise, so we can identify much smaller spectral features.

3.3.3 Analysis of the loss fraction

The variation in the peak resonant loss fraction (the maximum point on fig. 3.6(b), with the background, "off-resonant", loss subtracted) with the power P_2 of the Rydberg excitation laser λ_2 was studied, for the case of excitation to the $5s56d\,{}^1D_2$ state. The result is shown in fig. 3.9.

An increase in the power P_2 leads to an increase in the number of Rydberg atoms, and hence the Rydberg atom density. The loss fraction saturates with the Rydberg atom density, and is fit with a saturation curve $y = A(1-\mathrm{e}^{-Bx})$,

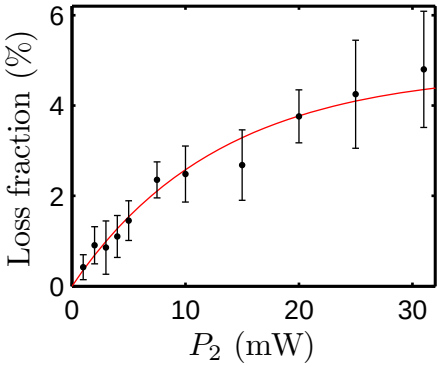

Figure 3.9: Variation is the loss fraction for the 56 $^1D_2$ state with the power P_2 of the Rydberg excitation laser λ_2. The red line is a saturation curve fit.

as shown by the red line on fig. 3.9. The fit returns $A = 5 \pm 1$ and $B = 0.08 \pm 0.03$ mW^{-1}. The loss fraction signal is not susceptible to any form of detector saturation. There is a possibility that this saturation is due to the dipole blockade (see chapter 1), or perhaps "'ion blockade"', where the electric field of the spontaneously created ions shifts the Rydberg state out of resonance with the laser [41, 126].

The loss fraction data in fig. 3.9 is used to estimate the number of Rydberg atoms created at different values of P_2. For this particular experiment the loss fraction is measured 32 μs after the end of the 4 μs Rydberg excitation. Preempting the measurement of the decay rate of the 56 $^1D_2$ state, presented in chapter 6, at this time 28% of the population initially excited to the Rydberg state will remain in the Rydberg state. Hence, by multiplying the loss fraction by $\frac{1}{0.28} = 3.6$ the maximum loss fraction can be estimated. By multiplying the loss fraction by the ground state population a *lower* bound can be set on the number of Rydberg atoms. It is a lower bound since this analysis does not include the Rydberg atoms lost due to spontaneous ionization, or decay to other states. A previous study [125] found that most of the Rydberg state population decays to the ground state.

An expression for the initial population of the Rydberg state N_R as a function of the laser power P_2 (in mW) can be formed:

$$\begin{aligned} N_R &= 3.6A(1 - \mathrm{e}^{-BP_2})N_{g.s.} \\ &\approx 18(1 - \mathrm{e}^{-0.08P_2})N_{g.s.}\,, \end{aligned} \tag{3.5}$$

where $N_{g.s.}$ is the population of the ground state. This analysis yields a peak Rydberg fraction of 17% at $P_2 = 31$ mW, which corresponds to a Rydberg density of $\sim 4.4 \times 10^9$ cm^{-3} in this particular case case.

This method for estimating the Rydberg state population will be essential later in this thesis. As it is presented here, it is *only* valid for experiments on the $5s56d\,^1D_2$ state, with our particular experimental set up.

Conclusion

We have studied a large range of Rydberg states in our cold gas of strontium. This has enabled us to locate states belonging to many different series. When using the step-scan technique we can spectroscopically resolve very weakly allowed transitions. The dynamic range is impressive, even when compared to the standard technique of field ionization, where an electric field ionizes the Rydberg atom, and the free ion or electron is detected. Field ionization produces more signal, since all of the Rydberg atoms are ionized, but by using the step-scan technique we do not need the experimental capability to produce large electric fields.

Using the step-scan method, we can measure many spectral points on a single spectroscopic feature, or cover a wide frequency range and locate many states. The step-scan is used to locate and detect Rydberg states throughout this thesis, since the Rydberg excitation lasers λ_2 are not frequency stabilized. Laser frequency drifts are not an issue when data is acquired with a step-scan, since the frequency is continuously measured. The step-scan can be used to estimate the population of the Rydberg state through measurement of the resonant loss from the ground state population.

The relative frequency accuracy and sensitivity of the step-scan technique allows us to test theoretical predictions of the energy structure of, and interaction between, Rydberg states in strontium. This will be the subject of the next chapter.

Chapter 4

Single-electron model for calculating dipole matrix-elements

Introduction

Rydberg atoms exhibit extremely large dipole-dipole interactions that lead to a wide range of fascinating interaction phenomena. Since neutral atoms do not have permanent dipole moments it is the transition dipole matrix-elements that are important when considering the interactions. With a knowledge of the interaction strengths, the complex many-body effects discussed in chapter 1 can be predicted, created and analyzed.

We calculate the dipole matrix-elements between states from electronic wavefunctions. While there are analytic solutions for the hydrogen atom, calculating wavefunctions for more complex, multi-shell atoms requires numerical techniques. These techniques are well established for alkali metals, where there is a single valence electron. We introduce a method for calculating wavefunctions for divalent atoms, where singly excited Rydberg states are treated as a single valence electron in a modified potential: a "single-electron"

model.

Dipole matrix-elements can be used to calculate the shift of state energies in an electric field, known as the Stark map. We can measure the Stark map using the step-scan technique presented in chapter 3. The high relative accuracy of this technique enables us to test and verify the single-electron model, at much higher n than any previous study. This work is presented in [12].

We use the dipole matrix-elements to calculate the interaction strengths between strontium Rydberg atoms, the first such study for strontium. A knowledge of these interaction strengths will enable us to create experiments that exploit the dipole blockade, which can lead to the creation of many-body entangled states. Some of the C_6 coefficient calculations are presented in [1].

This chapter will:

- Describe the **method** for calculating dipole matrix-elements, in section 4.1.
- Present **Stark maps**, which are used to verify our simulations and calibrate the electric field in our experiment, in section 4.2.
- Present a method for calculating **the C_6 coefficients**, which characterize long-range interaction strengths, in section 4.3.

NOTE: The code for optimizing model potentials, calculating dipole matrix-elements and generating Stark maps were written by Guy Corbett (under the supervision of Dr. R. Potvliege) and Jonathan Pritchard. All of the experimental data, comparison of data to theory, and calculation of interaction strengths in this chapter was my work.

4.1 Method

We wish to calculate the matrix-elements of the dipole operator. The dipole operator is defined as $\hat{\mu} = e\,\hat{\mathbf{r}} \cdot \hat{\mathbf{s}}$, where e is the charge of an electron, $\hat{\mathbf{r}}$ the radial position operator, and $\hat{\mathbf{s}}$ the electric field polarization vector. This can be expressed, in a spherical coordinate system, as [127]:

$$\hat{\mu} = e\hat{r}\sqrt{\frac{4\pi}{3}}\hat{T}_1^q(\theta,\phi)\,, \tag{4.1}$$

where $\hat{T}_1^q(\theta,\phi)$ are the spherical tensor operators of degree 1, with order $q = 0,\ \pm 1$ corresponding to π, $\sigma^{\pm}$ atomic transitions. The states upon which this operator acts can be calculated by considering the Schrödinger equation for a free electron with wavefunction Ψ moving in the potential $V(r)$ of the atomic core:

$$\hat{H}_A\Psi = -\frac{1}{2}\hat{\nabla}^2\Psi + V(r)\Psi = \mathrm{E}\Psi\,, \tag{4.2}$$

which is expressed in atomic units (a.u.). For any radially symmetric potential $V(r)$ the wavefunctions are separable into radial R and angular Y parts: $\Psi(r,\theta,\phi) = R_{n,l}(r)Y_l^{m_l}(\theta,\phi)$. The dipole transition matrix-element between states $|n',l',m_l'\rangle$ and $|n,l,m_l\rangle$ is then defined:

$$\begin{aligned}\langle n,l,m_l|\hat{\mu}|n',l',m_l'\rangle &= \langle R_{nl}|e\hat{r}|R_{n'l'}\rangle\sqrt{\frac{4\pi}{3}}\langle Y_{l,m_l}|\hat{T}_1^q|Y_{l',m_l'}\rangle \\ &\equiv (\mu_r)_{nl}^{n'l'}\,(\mu_\phi)_{lm_l}^{l'm_l'} \\ &\equiv \mu_{T_i}^{\ f}\,,\end{aligned} \tag{4.3}$$

where radial μ_r and angular μ_ϕ dipole transition matrix-elements have been defined, and also a total dipole transition matrix-element $\mu_{T_i}^{\ f}$ between an initial i and final f state. The states are labeled by their principal n, angular

momentum l, and angular momentum projection m_l quantum numbers. The angular matrix-elements have analytic solutions. Hence, the calculation of the dipole matrix-element depends upon the ability to calculate the radial wavefunctions R_{nl}.

To calculate the wavefunctions using our approach the form of the potential $V(r)$ must be known[1]. For hydrogen, the potential is simply the Coulomb potential of an electron exposed to a proton, $V(r) = -\frac{1}{r}$, the wavefunctions have analytic solutions, with binding energy eigenvalues $\mathrm{E} = -\frac{Ry}{n^2}$, where Ry is the Rydberg constant.

For multi-electron atoms, the form of the potential is more complex, due to the finite size of the core, and the possibility for the valence electrons to penetrate closed electronic shells. A model potential must be constructed to describe these effects, which we verify through its ability to reproduce experimentally measured state energies.

When considering an alkali metal, or a singly excited alkaline earth metal, the possibility of core penetration exposes the valence electron to the unscreened core potential, and the binding energy E is increased:

$$\mathrm{E} = -\frac{R_{\mathrm{Sr}}}{(n - \delta_{n,S,L,J})^2}\,, \tag{4.4}$$

where R_{Sr} is the Rydberg constant for strontium (see table A.1), and $\delta_{n,S,L,J}$ is the quantum defect (S labels the spin, and J labels the total angular momentum quantum number). The defect $\delta_{n,S,L,J}$ decreases with L, until the electron no longer penetrates the core, and the defect is very close to zero (and the wavefunctions are approximately hydrogenic). As an example, for Sr, $\delta_{n\to\infty,0,0,0} \simeq 3.26$ and $\delta_{n\to\infty,0,3,3} \simeq 0.08$ [109]. The state energies can be calculated, with eqn. (4.4), if the quantum defect is known.

[1] If using a Coulomb approximation approach the form of the potential does not need to be known [128].

Forming a model potential requires a knowledge of the quantum defects for the singlet and triplet $L = 0, 1, 2, 3$ angular momentum states (higher angular momentum states are presumed to behave hydrogenically; they have very small quantum defects). There is a limited selection of measured state energies for Sr [106–115], so the quantum defects for many of the states are extrapolated from low-n measured values. The variation of the quantum defect for a given series with n is modeled by a function of the form [26]:

$$\delta_{S,L,J}(n) = A_{S,L,J} + \frac{B_{S,L,J}}{(n - A_{S,L,J})^2}\,, \tag{4.5}$$

where A, B are fitting parameters. This model is suitable at high $n > 20$ [129] where the quantum defects are varying smoothly, and away from doubly excited perturbing states [26]. A simple extrapolation is used to find the parameters A and B, and their values are given in table A.4.

Once the quantum defects are known, a potential can be constructed, which must be able to reproduce them. We chose a model potential of the Klapisch form [130], where an electron moves in the field of a Sr^+ core:

$$V(r) = -\frac{1}{r} - \frac{(Z-1)e^{-ar}}{r} + be^{-cr}\,, \tag{4.6}$$

which is chosen to account for the penetration of the core by the valence electron, including both closed and open shells. Z is the atomic number, and a, b, c are fitting parameters. The fitting parameters are optimized so that the model potential reproduces the experimentally measured/extrapolated quantum defects. The optimization is carried out using a simulated annealing algorithm [131]. The parameters a, b, c are listed in table A.4.

Once this potential is known the radial wavefunctions are calculated using the Numerov method [132], and with these wavefunctions the dipole matrix-elements can be calculated [133].

The model potential we use assumes that there is a *single* electron moving in the model potential, and includes no term describing the interaction between valence electrons. For Rydberg states of strontium we assume we can still use this model: we apply a "single-electron" model for a divalent atom. Next, we test the accuracy of this method for calculating dipole matrix-elements.

4.2 Stark maps

One method for testing the single-electron model is to compare the measured and simulated shift in state energy in an electric field, otherwise known as the Stark map. As discussed in section 3.3, the relative frequency accuracy of our spectroscopic step-scan technique is good, so a measure of energy *shifts* is well suited to our experiment.

Theory

The addition of an electric field F along the z-axis modifies the zero-field atomic Hamiltonian operator H_A (see eqn. (4.2)) in the following way:

$$\hat{H}^{\text{total}} = \hat{H}_A + F\hat{z}\,, \tag{4.7}$$

where $\hat{H}^{\text{total}}$ is the Hamiltonian for an atom in a static electric field. This Hamiltonian yields a matrix with entries $H_{ii}^{\text{total}} = \mathrm{E}_i$ for the diagonal elements (where E_i is the energy of the state i in zero electric field), and $H_{ij}^{\text{total}} = F\mu_T{}_i^j$ for the off-diagonal elements ($i \neq j$). The Hamiltonian $\hat{H}^{\text{total}}$ is diagonalized to find the energy eigenvalues and eigenstates in an electric field.

The addition of the Stark interaction term $F\hat{z}$ mixes the bare atomic states. The eigenstates $|\chi\rangle$ of H^{total} at a given field F are a linear superposition of the bare atomic $|n, s, l, j\rangle$ states:

$$|\chi(F)\rangle = \sum_{n,l,j} c_{n,l,j}(F)|n,s,l,j\rangle\,, \tag{4.8}$$

where $c_{n,l,j}$ are the mixing coefficients. To accurately calculate the energy levels in an electric field a wide range of atomic states must be included in the calculation. We include states up to $l = 40$, and a range of $n = \pm 5$.

The Stark interaction does not mix states of different total angular momentum projection number $|m_j|$, so a separate Stark map must be calculated for different values of $|m_j|$. The Stark interaction does not mix states of different total spin S [134]. An example Stark map calculated in the region of the $5s56d\,^1D_2$ state, with $m_j = 0$, is shown in fig. 4.1, with some of the zero energy states labeled. The states with an insignificant quantum defect ($l > 3$) are degenerate in zero-field, and their energies vary linearly with field, forming a high angular momentum manifold. There are avoided crossings as the lower l states intersect the manifold.

A previous study has compared a single-electron model for strontium to a Stark map measured at $n = 12$ [135]. If we wish to utilize our calculated dipole matrix-elements we must be sure that they are accurate at much higher n. Below we present a comparison of measured Stark maps to the single-electron model around $n = 56$ and $n = 80$.

Results

These comparisons of calculated to experimentally measured Stark maps are presented in [12].

An example Stark map around the $5s56d\,^1D_2$ state is shown in fig. 4.2(a). The black lines are individual spectra taken using the step-scan technique, with a constant background electric field applied with the electrodes during the excitation to the Rydberg state. The simulated energy shifts of the $|m_j| = 0, 1, 2$ components of the $56\,^1D_2$ state are shown. The agreement is

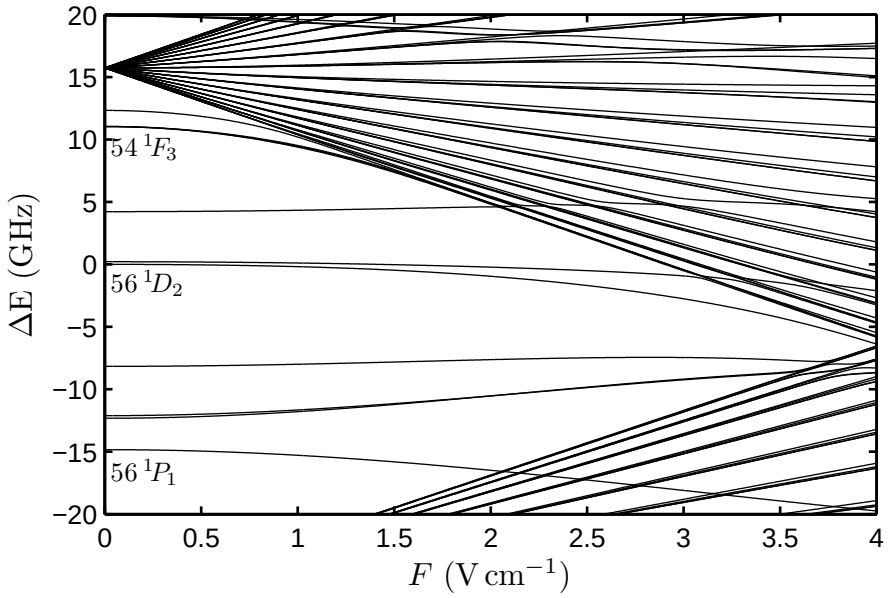

Figure 4.1: An example simulated $m_j = 0$ Stark map in the region of the $5s56d\,^1D_2$ state. Energy shifts ΔE are defined relative to the zero-field energy of the $56\,^1D_2$ state. Some of the states at zero-field are labeled. Gaps in the high angular momentum manifolds are due to a truncation of states above $l = 40$.

clearly good, as can be further seen in fig. 4.5(a), section 4.2.1. The splitting of the m_j components is matched by a broadening of the spectral feature. It should be noted that an arbitrary frequency offset is added to the data to produce the best agreement, necessary due to the absolute measurement uncertainty of the wavemeter.

At fields greater than $\sim$ 3 V cm^{-1}, higher angular momentum states are visible in the data. The simulated higher angular momentum manifold is indicated by the grey region on the plot. The higher angular momentum excitations are visible where the manifold intersects the data.

In fig. 4.2(b) the Stark map for the $5s54f\,^1F_3$ state is shown. Excitation to a Rydberg state is via the $5s5p\,^1P_1$ state, so in zero-field only $^1S_0$ and $^1D_2$ states are accessible. The $^1F_3$ state can only be excited due to the presence of an electric field F, and the signal is seen to vanish as F approaches zero. In this particular experiment autoionization was used to boost the signal, a

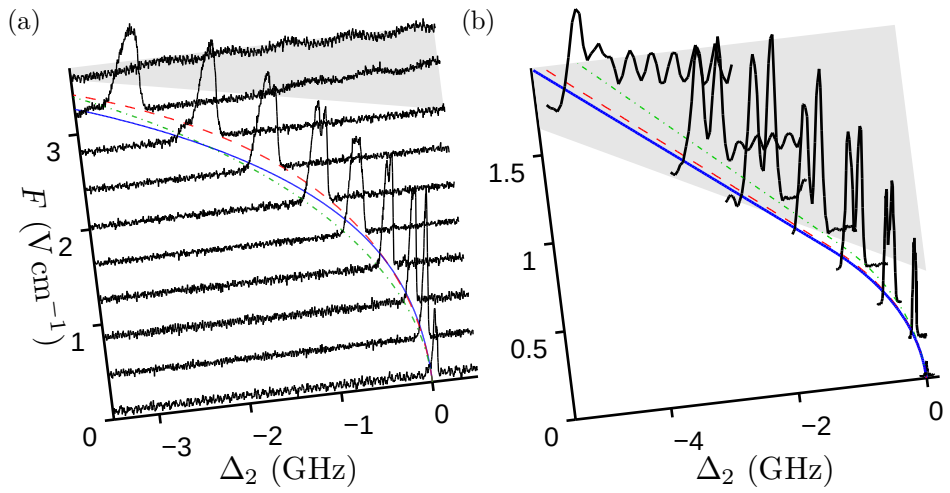

Figure 4.2: Stark maps around the (a) $5s56d\,^1D_2$ and (b) $5s54f\,^1F_3$ states. The black lines are experimental data. The blue solid, red dashed and green dot-dashed lines are the simulated $|m_j| = 0, 1, 2$ components of the state in question respectively. The grey regions are the simulated high angular momentum manifold. The frequency axes are the detunings of ω_2 from our measured zero-field state energies. (b) was taken using autoionization to enhance the ion signal. Nearby triplet states that are not visible in the data are not marked.

technique discussed in chapter 5. This leads to excellent signal-to-noise in this figure.

The simulated energy shifts for the $|m_j| = 0, 1, 2$ components of the $54\,^1F_3$ state are shown on fig. 4.2(b). The agreement is still good, though the proximity of the $^1F_3$ state to the higher angular momentum manifold makes following a specific zero-field state difficult. The simulated lines are linearly extrapolated once they intersect the high angular momentum manifold[2], which is marked in grey. The splitting of the m_j components is evident in the data, and the interaction with the high angular momentum manifold is very clear.

A Stark map in the region of $n = 80$ is presented in fig. 4.3. The Stark map is significantly more complex in this region, since the different atomic states

[2] In future work, the need to extrapolate could be solved through analysis of the coefficients $c_{n,l,j}(F)$ from eqn. (4.8).

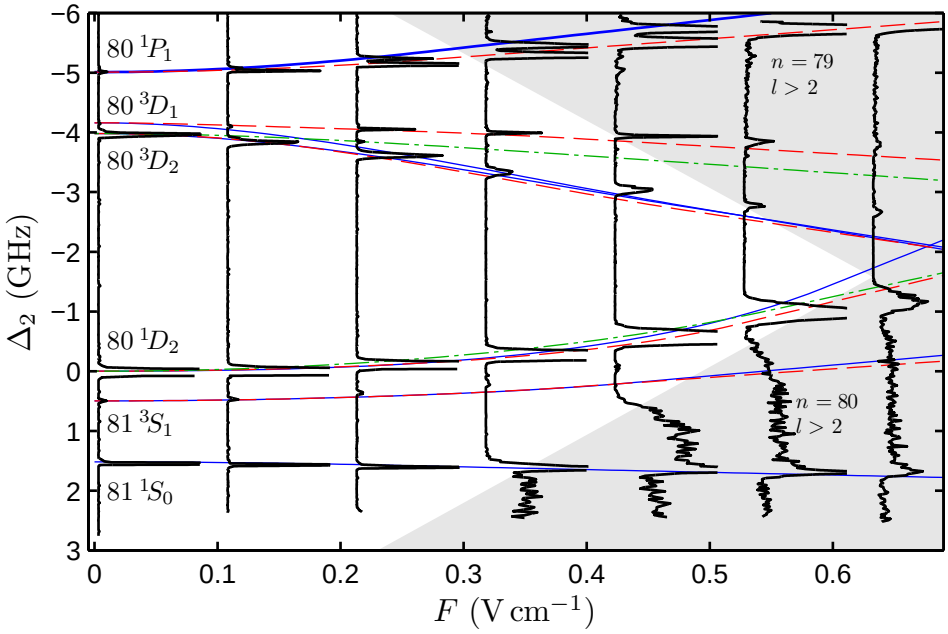

Figure 4.3: A Stark map in the region of the $5s80d\,^1D_2$ state. The experimental data (black lines) has been truncated for clarity. The simulation for the experimentally visible states have been highlighted: the blue (solid), red (dashed), green (dot-dashed) lines are the $|m_j| = 0, 1, 2$ components respectively. The grey regions mark the high angular momentum manifold. Δ_2 is the detuning of ω_2 from the measured energy of the $80\,^1D_2$ state.

are much closer in energy (energy spacings scale as n^{-3}). In low electric fields the Stark shift of state energies ΔE is given by second order perturbation theory as [134]:

$$\Delta \mathrm{E} = -\frac{1}{2}\alpha_0 F^2\,, \tag{4.9}$$

where α_0 is the scalar polarizability. α_0 scales as n^{*7}, hence the Stark shift becomes more severe at higher n. The highlighted state simulations have been linearly extrapolated once they intersect the high angular momentum manifold (grey regions).

The data has been offset to create best agreement with the $5s80d\,^1D_2$ state

in zero-field. This is the only state in this region for which the state energy is known [111], and so it is reasonable to take this as our reference point.

The zero-field energies of states other than $80\,^1D_2$ are adjusted to match the data. This is done by changing the quantum defects that go into the simulation. To get a good agreement requires a quantum defect adjustment of $< 1\%$. This is entirely reasonable, since at $n = 80$, most of the quantum defects are extrapolated, using eqn. (4.5). This extrapolation is from as low as $n = 30$ for many of the series. We believe that the relative accuracy of our frequency measurements is good, so it is justified to adjust the simulation to match the data.

The simulation reproduces all of the essential features of the data, which is remarkable considering how high in n the Stark map is taken. As a reminder, a previous study verified the single-electron model up to $n = 12$ [135]. The agreement between the simulation and the data for the singlet states is excellent. The high angular momentum manifolds (grey regions) are visible in the data, with the $n = 80$ manifold interacting much more strongly than the $n = 79$ manifold.

The model does not agree as well with the triplet states as it does for the singlet states, though the model still reproduces the general features. This worse agreement could be due to the lack of singlet-triplet mixing in the model. Unfortunately, when the quantum defects were adjusted to match the zero-field energies, it was not possible to re-optimize the core potential, for calculational reasons. General discrepancies at high-field could be due to lack of re-optimization, as a change in the core potential would alter the radial wavefunctions, and hence the dipole matrix-elements. At these high values of n it would be surprising if doubly excited states had a large effect, although the level of singlet-triplet mixing (i.e. the presence of triplet states in the Stark map), even at small electric fields, in fig. 4.3 is surprising.

Observations from other studies

In the alkali metals, Stark maps generated using dipole matrix-elements calculated from a model potential approach compare very well to experiment [136, 137]. For singly excited Rydberg states of alkaline earth metals it was argued that the the Stark shift of the inner valence electron is negligible, and that the electric field coupling between the valence and Rydberg states is small [138]. Hence, an approach where a Rydberg state of an alkaline earth metal is treated as a single electron moving in a model potential (the single-electron model) seems justified for calculating Stark maps.

Inaccuracies in simulated Stark maps for alkaline earth metal elements, using the single-electron model, have been noticed in previous studies. The presence of doubly excited states causes perturbations to the states in the Stark map [135], which can be fully accounted for by a significantly more complex multi-channel quantum defect theory [139]. Experimentally singlet and triplet states have been seen to interact in Stark maps [138] (through singlet-triplet mixing *not* caused by the Stark interaction) . Regardless, Stark maps for strontium (and other alkaline earth metals) calculated with the simple single-electron model are remarkably accurate, considering the limitations of the method.

In all, the agreement we find between the single-electron model and data is extremely encouraging, considering the simple nature of the model. Next, we will discuss how the step-scan technique is used to calibrate our electric field, and quantitatively test the single-electron model.

4.2.1 Electric field calibration

As described in appendix C, it is possible to simulate the electric field that is produced by our electrodes, with an outcome that for every ± 1 V applied to the electrodes in our standard configuration (fig. 3.1(b)), 0.36 $\mathrm{V\,cm^{-1}}$

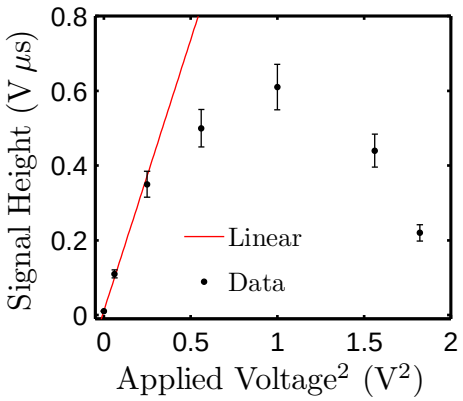

Figure 4.4: The variation in the height of the $5s80p\,^1P_1$ state peak with the voltage applied to the electrodes. Since the excitation to the Rydberg state is via the $5s5p\,^1P_1$ state using linearly polarized light, the $80\,^1P_1$ state should not be present in zero-field. The first few points are fit with a straight line, as described in the text, to identify any stray electric field in our experiment.

of electric field is produced at the position of the atoms. We verify this calculation through a quantitative comparison of the single-electron model calculated Stark maps to the data.

First, the stray electric field at the position of the atoms is estimated. In the Stark map around $n = 80$ (fig. 4.3) many states that cannot be excited in zero-field are visible. By looking at the variation in absolute size of these lines with the applied field, the stray field can be estimated.

We look at the $80\,^1P_1$ state from the Stark map in fig. 4.3. The variation in the height of this feature with the voltage applied to the electrodes is shown in fig. 4.4. The rise of the ion signal S with applied voltage V^2 is fit with a linear function $S = a\mathrm{V}^2 + b$, where a and b are free parameters, with b being the equivalent "stray voltage" to produce the stray field[3]. This works at low applied voltage, before the mixing of higher angular momentum states causes the height of the $80\,^1P_1$ line to decrease. A different function may describe

[3] The voltage axis is squared since the rise of the $80\,^1P_1$ signal appears to be quadratic with voltage.

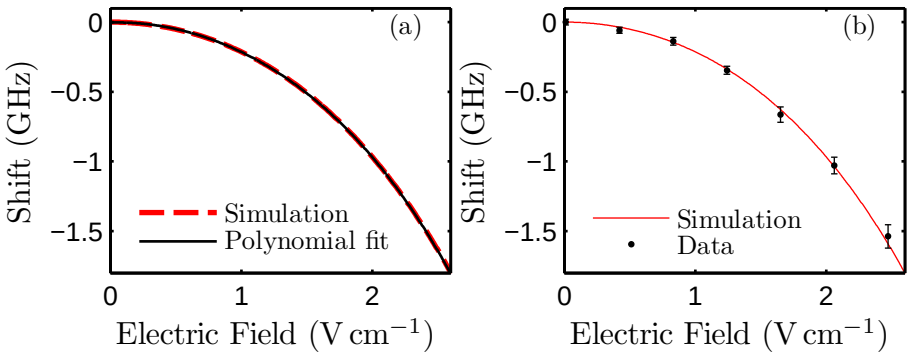

Figure 4.5: (a) The simulated variation in the $5s56d\,^1D_2$ state energy with electric field (solid red line), with a 4^{th} order polynomial fit (dashed black line). (b) The simulated (solid red line) and measured (black dots) shift in the $5s56d\,^1D_2$ state energy with electric field, after the electric field calibration has been applied to the measured data.

the overall shape of the data, but to estimate the stray field it is the initial appearance of the $80\,^1P_1$ signal that is important.

We estimate a stray voltage of $V_{\text{stray}} = 6.9 \pm 0.9$ mV. The experimental data presented in this chapter is adjusted to include this stray voltage value. This stray voltage is the equivalent voltage that would create the stray electric field.

Next, the data is compared to the simulations to determine the electric field calibration: the calibration between applied voltage and produced electric field. First, the energy shift of the $5s56d\ ^1D_2$ state from the Stark map fig. 4.2(a) is considered. To enable a comparison between the simulation and the experimental data a functional form for the numerically simulated Stark map must be known. It is found that a 4^{th} order polynomial fits the simulation well, as shown in fig. 4.5(a), and any increase in the order does not significantly improve the fit.

Another requirement for a comparison of the simulation and data, is a measure of the position of the $56\,^1D_2$ state in the data at each applied voltage. The spectra in fig. 4.2(a) are fit with a Gaussian function at each applied

voltage to find the centre and the width of the lines. The Gaussian FWHM is used as an error bar[4]. The experimentally measured line positions are shown in fig. 4.5(b). To find the electric field calibration we apply the following fit to the experimental data:

$$\Delta \mathrm{E} = c_4(a\mathrm{V})^4 + c_3(a\mathrm{V})^3 + c_2(a\mathrm{V})^2 + c_1(a\mathrm{V}) + c_0' \,, \tag{4.10}$$

where ΔE is the state energy shift, V the applied voltage, a the scaling parameter which determines the electric field calibration, and the c coefficients are the parameters yielded from the 4^{th} order polynomial fit to the simulation *except* c_0' which a new offset parameter.

To clarify, initially the simulation is fit with a 4^{th} order polynomial in electric field, and then the experimental data is fit with the same 4^{th} order polynomial in applied voltage, with a scaling parameter a, which yields the applied voltage to electric field calibration. This yields a scaling parameter $a = 0.41 \pm 0.01$; for every ± 1 V applied to the electrodes in our standard configuration (fig. 3.1(b)), 0.41 V cm^{-1} of electric field is produced at the position of the atoms.

Figure 4.5(b) shows the comparison between the experimental data and simulation once this field calibration is applied to the data, and the agreement is clearly excellent. The fact that only a single scaling parameter a is required to produce this agreement verifies the accuracy of the simulation.

As a further test, the same calibration process is applied to the $5s80d\,{}^1D_2$ state, using the data in fig. 4.3. This analysis returns a field calibration factor of $a = 0.43 \pm 0.01$, which is very similar to the $56\,{}^1D_2$ state calibration factor. By taking the average of the $56\,{}^1D_2$ and $80\,{}^1D_2$ field calibration values, we

[4] The full-width at half-maximum (FWHM) is given by FWHM $= \sqrt{8ln(2)}\sigma \simeq 2.35\sigma$, where σ is the standard Gaussian width parameter.

find a final scaling factor of 0.42 ± 0.01 V cm^{-1} per ± 1 V we apply in the standard electrode configuration, fig. 3.1(b). This calibration factor is used in all of the data presented in this chapter. Applying this to the stray voltage yields a stray field of 2.9 ± 0.4 mV cm^{-1} at the position of the atoms, which is remarkably small. The geometry of our electrodes may be shielding the atoms from stray field. This size of stray field is consistent with the electric field due to the MCP grid.

The original electrode simulation calibration factor is within 13% of the experimentally verified answer. Some possible reasons for this discrepency are discussed in appendix C.

The excellent quantitative agreement between the data and single-electron model for the $^1D_2$ states in fig. 4.5, and the qualitative agreement between the simulation and the measured Stark maps in figs. 4.2 and 4.3, means that we can have confidence in our calculated dipole matrix-elements.

4.2.2 State characters

In zero electric field, each atomic state in the single-electron model has a well defined set of quantum numbers; it is a specific $|n, s, l, j\rangle$ state. An electric field mixes the states, such that a particular resonance will be a superposition of many different $|n, s, l, j\rangle$ states (eqn. (4.8)).

The Stark map simulation orders states by energy. This makes following the state, which is (for example) labeled $80\,^1P_1$ in zero-field (fig. 4.3), impossible once it begins to interact with the high angular momentum manifold. However, the simulation calculates the field dependent mixing coefficients $c_{n,l,j}(F)$, as defined in eqn. (4.8). The fraction of a state $|n, s, l, j\rangle$ that is mixed into the zero-field state, by an electric field F, is defined as $|c_{n,l,j}(F)|^2$. A plot of the variation in the $|c_{n,l,j}(F)|^2$ with F is referred to as a "character map".

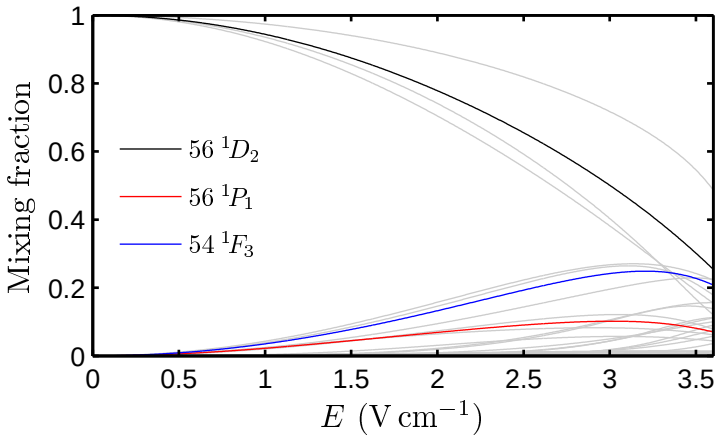

Figure 4.6: Character map for the $56\,{}^1D_2$ state. In zero electric field F the state is 100% $56\,{}^1D_2$, but as the field increases other states are mixed in. The average over the $|m_j|$ components of the $56\,{}^1D_2$ (black), $56\,{}^1P_1$ (red) and $54\,{}^1F_3$ (blue) states are highlighted. The grey lines are the characters of all states with $l < 6$ (truncated for clarity, though all states up to $l = 40$ are included in the calculation), for all allowed $|m_j|$.

The character map for the $5s56d\,{}^1D_2$ state is shown in fig. 4.6. By an electric field of 2 V cm^{-1}, the state is only 78% $56\,{}^1D_2$ in character. At this field the state contains 7% $56\,{}^1P_1$ state character, and 13% $54\,{}^1F_3$ state character. These are the most strongly dipole-coupled pair of states to the $56\,{}^1D_2$ state, and account for most of the mixing at low fields. At $\sim$ 3 V cm^{-1} many higher angular momentum states (grey lines) mix into the $56\,{}^1D_2$ state. This is comparable with the point at which the $56\,{}^1D_2$ state intersects the high angular momentum manifold in the Stark map (fig. 4.2).

The process by which an electric field mixes in states of differing characters is known as Stark mixing, and we will return to this subject in chapter 6.

4.3 The C_6 coefficients

In the introduction to this thesis, the reasons for wanting to study a gas of Rydberg atoms were discussed. One key motivation is the ability to cre-

ate many-body entangled states through the dipole blockade [32], where the interaction between Rydberg atoms shifts multiply excited states out of resonance with the driving laser field. This occurs when the interaction induced shift in the Rydberg state energies is larger than the linewidth of the Rydberg excitation. When this condition is met the Rydberg gas is said to have reached the "blockaded regime".

The relevant inter-Rydberg atom interaction in our experiment is the long-range dipole-dipole, or van der Waals, interaction. This is because our Rydberg gas is relatively low density, and we have located no "Förster resonances" [121], which would lead to resonant dipole-dipole interactions. The strength of the van der Waals interaction is encoded in the C_6 coefficient, and the ability to calculate these coefficients will enable us to determine when the Rydberg gas will reach the blockaded regime.

4.3.1 Theory

To calculate the interaction energy between Rydberg atoms we follow the approach of [140].

The dipole-dipole interaction V_{dd} between two atoms, A and B, separated by a distance R along the quantization axis z, is:

$$V_{\text{dd}} = \frac{e^2}{R^3}(\mathbf{a}\cdot\mathbf{b} - 3a_z b_z)\,, \tag{4.11}$$

where $\mathbf{a}$ is the position of the valence electron on atom A, and $\mathbf{b}$ the position of the valence electron on atom B. The atoms are labeled by their quantum numbers $|n,l,j\rangle$[5]. In the simplest case, the interacting atoms are in the same $|n,l,j\rangle$ state, so that $n_A = n_B = n$ etc. In this case the interaction can be

[5] The dipole-dipole interaction does not couple states with different spin s, so this label is not included in the notation.

written:

$$|n,l,j\rangle + |n,l,j\rangle \rightarrow |n_s,l_s,j_s\rangle + |n_t,l_t,j_t\rangle\,, \tag{4.12}$$

where s and t label the final states of the two atoms, which can be any dipole coupled states to the initial pair. The sign, and to some extent the strength, of the interaction between the two initial atoms depends on the difference in binding energy E between the initial and final pair states. This quantity is known as the energy defect δ_{st}, and is defined as:

$$\delta_{st} = \mathrm{E}(n_s,l_s,j_s) + \mathrm{E}(n_t,l_t,j_t) - 2\mathrm{E}(n,l,j)\,. \tag{4.13}$$

The sign of δ_{st} sets the sign of the interaction, with $\delta_{st} > 0$ leading to an attractive interaction, since there is a net increase in binding energy. For each initial l and j there is a series of final states that has the smallest δ_{st}. Once the energy defects and dipole matrix-elements are known, the interaction energy shifts of the initial and final states can be calculated.

Single interacting pair state

We begin by considering the simplest case, where the atoms in the initial state are identical in all of their quantum numbers n, l, j and m_j. This initial pair state is labeled $|AA\rangle$. We consider the initial pair state interacting with a single destination state $|st\rangle$. In this simplest case the Hamiltonian for the interaction between two atoms separated by R is:

$$H_{st}(R) = \begin{pmatrix} 0 & \frac{e^2 {\mu_T}^s_A {\mu_T}^t_A}{R^3} \\ \frac{e^2 {\mu_T}^s_A {\mu_T}^t_A}{R^3} & \delta_{st} \end{pmatrix}\,, \tag{4.14}$$

where μ_T is the total dipole matrix-element as defined in eqn. (4.3). By diag-

onalizing this matrix we find the eigenvectors and energy eigenvalues for the dipole-dipole interaction between the initial pair of atoms. The eigenvalues $\Delta_{\pm}(R)$ are:

$$\Delta_{\pm}(R) = \frac{1}{2}\left(\delta_{st} \pm \sqrt{\delta_{st}^2 + \frac{4e^4(\mu_{T_A^s}\mu_{T_A^t})^2}{R^6}}\right), \tag{4.15}$$

which correspond to the energy shifts of the initial and destination pair states. By simple inspection of these eigenvalues, it can be seen that if δ_{st} is small then the energies shift as R^{-3} (resonant dipole-dipole interaction), and through Taylor expansion if δ_{st} is large then the energies shift as R^{-6} (van der Waals).

Full form of the interaction

Next we consider the interaction between an initial pair state and *many* coupled destination pair states. When δ_{st} is large, the dominant interaction between the atoms is of a van der Waals type, with a R^{-6} scaling, as shown above for a single coupled pair state. When there are many destination states, the energy shifts are determined by the following operator (according to second order perturbation theory):

$$\hat{H}_{\mathrm{vdW}} = \sum_{st} \frac{V_{\mathrm{dd}}|st\rangle\langle st|V_{\mathrm{dd}}}{-\delta_{st}}, \tag{4.16}$$

where the sum is over *all* possible final states $|st\rangle$, including the sublevels m_j of the total angular momentum j for each electron. We now consider the possibility that the initial atoms are in different m_j states, and the initial pair state is written $|AB\rangle$. The operator $\hat{H}_{\mathrm{vdW}}$, acting on $|AB\rangle$, gives:

$$\hat{H}_{\mathrm{vdW}}|AB\rangle = \frac{C_6}{R^6} D_{\phi}|AB\rangle, \tag{4.17}$$

where C_6 encodes the strength of the radial part of the interaction, and D_ϕ the angular part. The D_ϕ eigenvalues take the values $0 \leq D_\phi < 1$, and their calculation is detailed in [140]. There is a value of D_ϕ, and hence an interaction strength, for each combination of initial and final $|l, j, m_j\rangle$ states.

C_6 is defined as (in atomic units):

$$C_6 = \sum_{|st\rangle} \frac{e^4}{-\delta_{st}} (\mu_{r_{nl}}^{n_s l_s} \mu_{r_{nl}}^{n_t l_t})^2 \,, \tag{4.18}$$

where μ_r is the radial matrix-element $\langle R_{n_t l_t} | \hat{r} | R_{n_s l_s} \rangle$ between the initial and final state, as calculated in the single-electron simulation (the angular part of the matrix-element is included in D_ϕ). The sum is over all coupled final states. This equation highlights the dependence of the sign of the interaction upon δ_{st}. Since the matrix elements scale as n^2, and the energy defect as n^{-3} [26], C_6 scales as $\sim n^{11}$. For an initial pair of m_j values, D_ϕ is summed over all of the destination states, yielding a single total interaction strength $D_\phi C_6$ for each initial n, l, j, m_j configuration $|AB\rangle$.

Practically, $\hat{H}_{\text{vdW}}$ is the Hamiltonian in eqn. (4.14) extended to include the coupling to all possible pair states, with the relevant δ_{st} for the diagonal elements, and couplings $\frac{\sqrt{-\delta_{st} D_\phi C_6}}{R^3}$ for the off-diagonal elements. Diagonalization of the resulting matrix yields the eigenvectors and energy eigenvalues for all of the coupled pair states.

At short range the interaction switches from being of the van der Waals type, and becomes of the resonant dipole-dipole type, which scales as R^{-3}. The separation R_c at which the interaction switches from the van der Waals to the resonant dipole-dipole regime, is [27]:

$$R_C = \left(\frac{D_\phi C_6}{\delta_{st}} \right)^{\frac{1}{6}} . \tag{4.19}$$

For two atoms in a $50\,^1S_0$ state, $R_c = 1.04\ \mu$m, which corresponds to an average atomic density of $\sim 2 \times 10^{12}$ cm^{-3}, two orders of magnitude higher than the typical *ground state* densities in our experiment. Our experiments are performed firmly in the van der Waals regime. The analysis presented above breaks down for interatomic separations much smaller than R_C, as higher order electric multipole interactions significantly perturb the total interaction strength [141].

We do not include the coupling of the destination states $|st\rangle$ to further states, which are not coupled to the initial pair state $|AB\rangle$. An example of a treatment that does consider these further couplings can be found in [141].

4.3.2 Results for the $^1S_0$ series

Calculating the interaction between strontium atoms in $^1S_0$ states is particularly simple, since this series *only* has an $m_j = 0$ state. Also, there is only one possible set of destination pair state: $n\,^1S_0 + n\,^1S_0 \rightarrow n_s\,^1P_1 + n_t\,^1P_1$. Consequently, there is a single angular coupling $D_\phi = \frac{2}{3}$.

In fig. 4.7(a) the variation in the energy defect with effective quantum number, for the dominant transition $n\,^1S_0 + n\,^1S_0 \rightarrow n\,^1P_1 + (n-1)\,^1P_1$, is shown. The energy defect is always positive, hence the interactions for the $^1S_0$ states are always attractive.

In fig. 4.7(b) the variation in C_6 with effective principal quantum number n^* is shown[6]. The scatter is most likely due to inaccuracies in the measured quantum defects for the $^1S_0$ and coupled $^1P_1$ states (note the scatter in δ_{st}, fig. 4.7(a), in the same region of n^*). It is useful to parametrize the variation of C_6 with the effective quantum number n^*, removing the dominant n^{*11} scaling, and we use a parameterization of the following form [4]:

[6] $C_6(\text{GHz}\,\mu\text{m}^6) = \frac{E_H a_0^6}{h} 10^{27} \times C_6(\text{a.u.}) \simeq (1.44 \times 10^{-19}) C_6(\text{a.u.})$.

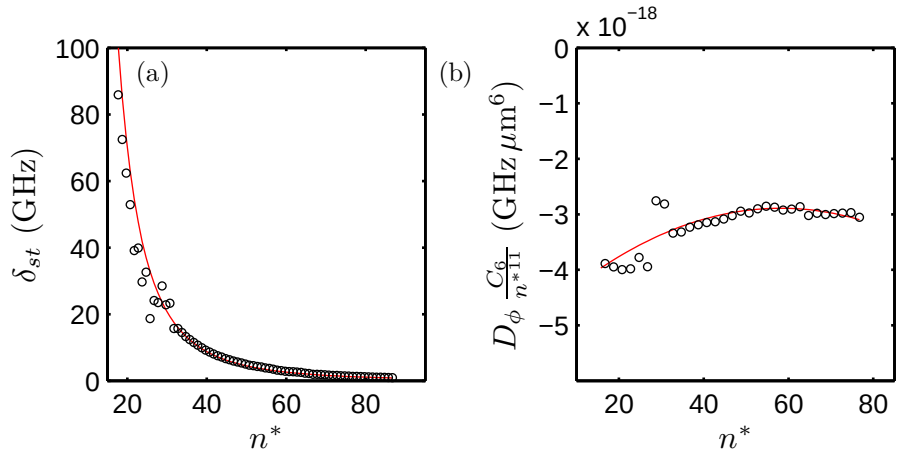

Figure 4.7: (a) The variation in the energy defect for $n\,{}^1S_0 + n\,{}^1S_0 \rightarrow n\,{}^1P_1 + (n-1)\,{}^1P_1$ with the effective principal quantum number n^* of the initial ${}^1S_0$ states. The red line is an n^{*-3} fit. (b) The variation in C_6 (including the angular term, which is n independent), scaled by n^{*11}, with n^*. The red line is a quadratic fit.

$$D_\phi\, C_6(\text{a.u.}) = (a + bn^* + cn^{*2})n^{*11}\,. \tag{4.20}$$

The results obtained by fitting the curve in fig. 4.7(b) are $a = -34$, $b = 0.5$ and $c = -0.004$[7]. Once the dominant n^{*11} scaling is taken out of $D_\phi\, C_6$, the size of the interaction strength varies by less than 10% over a range of 60 n states, indicating that $D_\phi\, C_6 \propto n^{*11}$ is a fair approximation for the ${}^1S_0$ states. These values of $D_\phi\, C_6$ for the ${}^1S_0$ states of strontium agree with values calculated through a two-electron Hartree-Fock method [1].

An example interaction curve, for two atoms in a $60\,{}^1S_0$ state, is shown in fig. 4.8, calculated using eqn. (4.14) expanded to include the nearest 400 coupled pair states. At large separations, the y-axis is the energy defect δ_{st}. The strongest interaction is with the $60\,{}^1P_1 + 59\,{}^1P_1$ pair state (solid red lines). There are many other pair states that are coupled to the initial pair (black lines on fig. 4.8), and even close in energy, but do not interact significantly

[7] Error bars are not included as it is a fit to a numerical simulation.

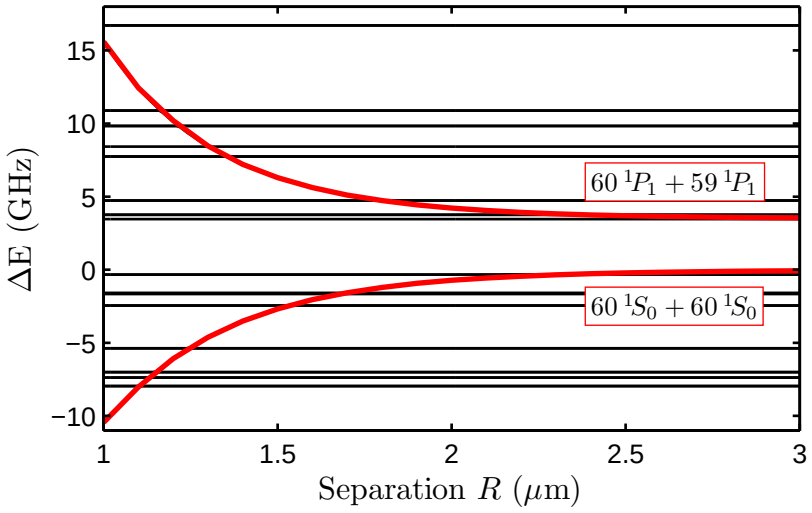

Figure 4.8: The shift in state energy with separation, for pair states in the region of $60\,{}^1S_0 + 60\,{}^1S_0$. The initial pair, and most strongly interacting pair, have been highlighted in red. The black lines are coupled pair states that are nearby in energy, but only very weakly dipole coupled to the initial pair state.

(the coupling is very weak)[8]. This graph has been plotted for separations greater than the van der Waals radius R_c, which is ~ 1 μm for the $60\,{}^1S_0$ state.

If the interaction between the atoms shifts the state energy by the linewidth of the Rydberg transition, then the excitation will no longer be resonant. This describes the dipole blockade (section 1.2), and occurs at a characteristic separation R_B, known as the blockade radius. In our experiment, the linewidth of the Rydberg transition is that of the intermediate state ($2\pi \times 32$ MHz), as shown in chapter 3. For a $60\,{}^1S_0$ pair, $R_B = 3.5$ μm, which corresponds to an average Rydberg density of 4×10^9 cm^{-3}, or $\sim 10\%$ of the ground state atom density.

[8] Since the pair states marked with the black lines do couple to the initial pair state there are avoided crossings when the energy curves intersect. The avoided crossings are masked by the solid red lines.

4.3.3 Results for the $^1D_2$ series

Calculating the interaction strengths for the $^1D_2$ states is more complex than for the $^1S_0$ states. Firstly, there are three dipole coupled sets of destination states: $n_s\,^1P_1 + n_t\,^1F_3$, $n_s\,^1P_1 + n_t\,^1P_1$ and $n_s\,^1F_3 + n_t\,^1F_3$.

The variation in energy defect for the n configuration that yields the smallest energy defect value, for each of the possible dipole couplings, is shown in fig. 4.9(a). From the figure it is clear that the coupling with the smallest defect is $n\,^1D_2 + n\,^1D_2 \rightarrow n\,^1P_1 + (n-2)\,^1F_3$. This defect is always negative, but it is *not* true to say that this implies the interaction between $^1D_2$ states is always repulsive. The defects to the $n\,^1P_1 + n\,^1P_1$ states are negative, but the defects to the $n\,^1F_3 + n\,^1F_3$ states are positive. If the coupling to the $n_s\,^1F_3 + n_t\,^1F_3$ pair dominates, through the angular term D_ϕ, then the sign of the interaction can change.

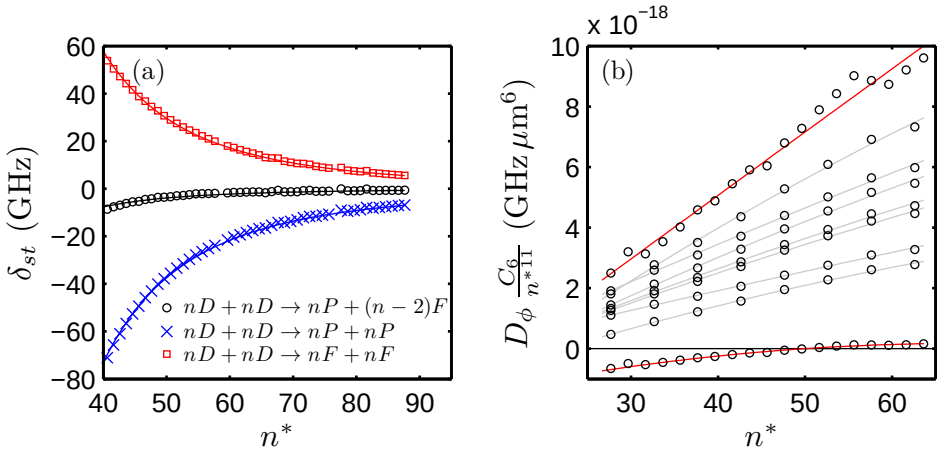

Figure 4.9: (a) The variation in the energy defects, for the different destination pair states, with the effective principal quantum number n^* of the initial $^1D_2$ states. The solid lines are n^{*-3} fits. (b) The variation in C_6 (including the angular term, which is n independent) with n^* for the $^1D_2$ states. The data (black circles) and fits (grey lines) for all of the possible initial m_j configurations are shown. The extremal cases have been highlighted with red lines.

Another complication is that are many combinations of initial m_j state. La-

	a	b	c	n_c^*
$\|-2,2\rangle$	-16	0.5	-0.004	50
$\|-1,1\rangle$	-25	1.5	-0.004	18
$\|0,0\rangle$	-17	1.1	-0.003	17
$\|0,-1\rangle$,$\|0,1\rangle$	-23	1.5	0.00	16
$\|-2,1\rangle$,$\|-1,2\rangle$	-14	0.7	-0.002	22
$\|-2,0\rangle$,$\|0,2\rangle$	-13	0.9	-0.002	16
$\|-1,-1\rangle$,$\|1,1\rangle$	-12	0.8	-0.002	16
$\|-2,-1\rangle$,$\|1,2\rangle$	-27	1.7	-0.01	18
$\|-2,-2\rangle$,$\|2,2\rangle$	-5	0.5	0.00	11

Table 4.1: This table lists the parameters for different $|m_{jA}, m_{jB}\rangle$ states, obtained from the fits (eqn (4.20)) to the C_6 curves in fig. 4.9(b). n_c^* is the value of effective quantum number at which we predict the interaction will change sign.

beling each initial atom as atom A and atom B, we designate the initial m_j configuration as $|m_{jA}, m_{jB}\rangle$. Each $|m_{jA}, m_{jB}\rangle$ state has an angular coupling D_ϕ to each destination state, yielding an interaction strength for each $|m_{jA}, m_{jB}\rangle$ state. The variation in $D_\phi C_6$ with n^*, with the dominant n^{*11} scaling removed, for all of the initial $|m_{jA}, m_{jB}\rangle$ states is plotted in fig. 4.9(b). This plot shows that, for the $^1D_2$ states, the sign of the interaction changes as n^* is varied. There are nine distinct combinations of $|m_{jA}, m_{jB}\rangle$, with the most strongly interacting being ($|-1,0\rangle$ or $|0,1\rangle$), and the least strongly interacting being $|-2,2\rangle$. The change in sign is particularly marked for the $|-2,2\rangle$ state. The variation of $D_\phi C_6$ with n^* has been parametrized, using eqn. (4.20), and the results are listed in table 4.1. Also included in this table is n_c^*, the value of n^* at which the sign of the interaction changes (as obtained by the fit).

The $|-2,2\rangle$ state is a so called "Förster zero" state [142], and two atoms in this state interact significantly less strongly than $^1D_2$ atoms in any other

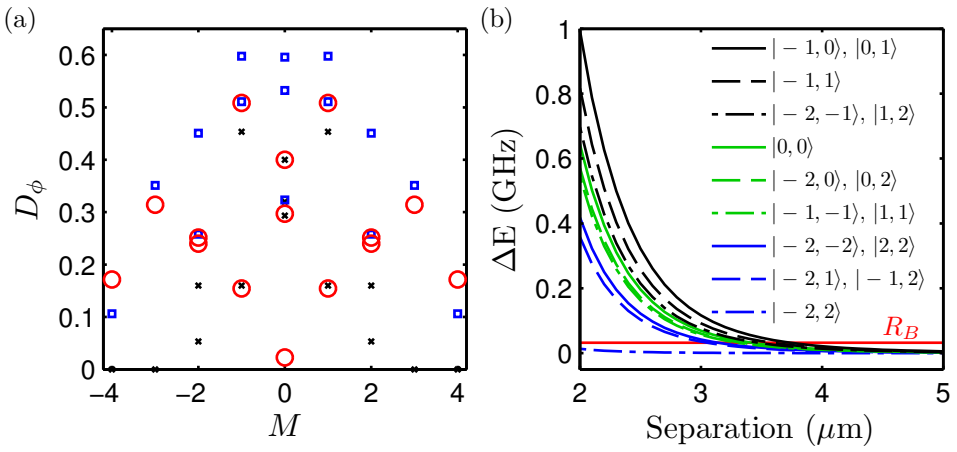

Figure 4.10: (a) The angular couplings D_ϕ, grouped by $M = m_{jA} + m_{jB}$, between a pair of $^1D_2$ state atoms and a $^1P_1$ (black crosses), $^1F_3$ (blue squares) or $^1P_1 + ^1F_3$ (red circles) pair. (b) The shift in state energy ΔE as two 56 $^1D_2$ atoms in various $|m_{jA}, m_{jB}\rangle$ states are brought together. The red line is the shift required for blockade.

$|m_{jA}, m_{jB}\rangle$ state. The spectrum of D_ϕ for the different pair state transitions, grouped by $M = m_{jA} + m_{jB}$ (M is conserved), is shown in fig. 4.10(a). The $|-2,2\rangle$ state ($M = 0$) has a very small angular coupling to the $n_s\,^1P_1 + n_t\,^1F_3$ pair (red circle near $D_\phi = 0$). This explains why the interaction strength between atoms in the $|-2,2\rangle$ state is smaller than for the other $|m_{jA}, m_{jB}\rangle$ states, as the $n_s\,^1P_1 + n_t\,^1F_3$ pairs are closest in energy. The coupling of the $M = 0$ states to the $n_s\,^1F_3 + n_t\,^1F_3$ pairs (blue squares) is always non-zero. This explains the propensity for the sign of the interaction to change, since these pairs have the opposite sign of interaction to the other pair states.

The explicit difference between the interatomic interactions for different $|m_{jA}, m_{jB}\rangle$ states is illustrated in fig. 4.10(b), for the example of two atoms in the 56 $^1D_2$ state. These curves are calculated using the eigenvalues in eqn. (4.15)[9], using values of C_6 calculated by including all pair state cou-

[9] The eigenvaules of the two pair state Hamiltonian in eqn. (4.14), in terms of C_6, are $\Delta_\pm(R) = \frac{\delta_{st}}{2} \pm \frac{1}{2}\sqrt{\delta_{st}^2 + \frac{4\delta_{st} D_\phi C_6}{R^6}}$ [140].

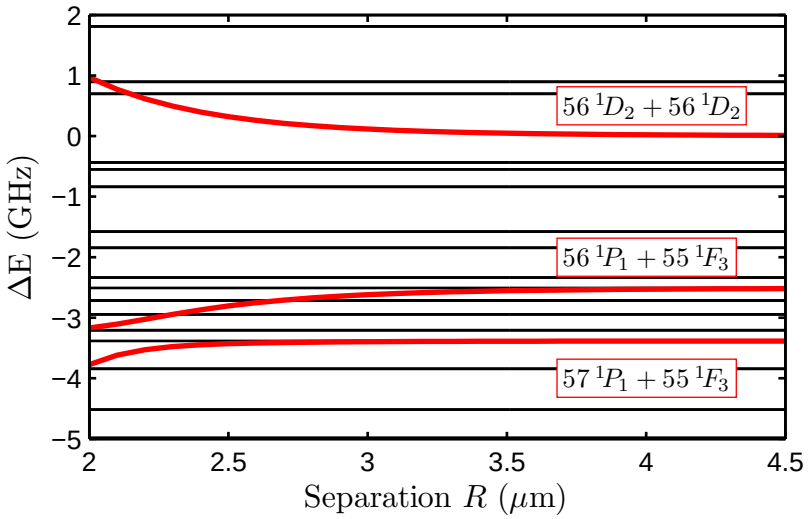

Figure 4.11: The shift in state energy with separation for pair states in the region of $56\,^1D_2 + 56\,^1D_2$. The initial pair, and most strongly interacting pairs, have been highlighted in red. The black lines are par states that are nearby in energy, but only very weakly dipole coupled to the initial pair state.

plings. This is an approximation, to highlight the initial m_j dependence of the interaction. This figure highlights the severe suppression of interaction strength for the Föster zero state $|-2, 2\rangle$.

The energy shift required for dipole blockade is marked on fig. 4.10(b). The blockade radius is $R_B \simeq 3.5$ μm for most of the $|m_{jA}, m_{jB}\rangle$ states, which corresponds to an average Rydberg density of 4×10^9 cm^{-3}. However, the $|-2, 2\rangle$ would not be blockaded at this separation. For a gas of Rydberg atoms in the $56\,^1D_2$ state to be fully blockaded would require a significantly higher Rydberg atom density.

Finally, the full interaction curve for two $56\,^1D_2$ state atoms is shown in fig. 4.11, calculated using eqn. (4.14) expanded to include the nearest 400 states. The calculation is for the $|m_{jA}, m_{jB}\rangle$ state with the largest $D_\phi\, C_6$: $|-1, 0\rangle$, $|0, 1\rangle$. Over the displayed energy range there are two pairs of states that are strongly interacting with the initial pair. The van der Waals crossover for the $56\,^1D_2$ state is $R_c \simeq 1.7$ μm.

To summarize, although the interpretation of interaction strengths between $^1D_2$ state atoms is more complex, for most regions of the Rydberg spectrum that we have studied the interactions between these atoms are repulsive. However, the presence of a Förster zero state makes it more difficult to reach the blockaded regime. Interestingly, preliminary calculations indicate that the interaction between atoms in $^3S_0$ states is always repulsive, without the issue of a Förster zero, with an interaction strength somewhat higher than for the $^1D_2$ states.

Limitations of the single-electron model

Strontium has two valence electrons, so the single-electron model can only be an approximation. One limitation of this model is that it does not account for interactions between the two valence electrons.

The single-electron model does not include doubly excited states. These states can strongly perturb the Rydberg series. This occurs in strontium at $n = 17$ for the $^1D_2$ series, and at lower n for the $^1S_0$ and $^1P_1$ and series [107]. Doubly excited autoionizing states (see chapter 5) have very large excitation cross sections, and very short lifetimes, so admixture of these states will significantly affect those properties of the singly excited states.

The presence of the doubly excited states causes mixing between the singlet and triplet series. In strontium, at $n = 15$, the $^1D_2$ and $^3D_2$ series switch character [107]. The mixing essentially adds extra decay channels, which means that, if singlet-triplet mixing is neglected, accurate state lifetimes and line-strengths cannot be calculated [143, 144]. To fully account for singlet-triplet mixing, and doubly excited states, multi-channel quantum defect theory (MQDT) must be used [107, 145].

Neither singlet-triplet nor doubly-excited state mixing should have a great affect on the calculation of dipole matrix-elements using the single-electron

model, away from the regions of strongest perturbation. If the admixture of triplet/doubly excited states is small, the probability of transition to the singlet/singly excited state will be small, and hence the effect upon the dipole transition matrix-elements will be small.

Conclusion

We have presented a method for calculating dipole matrix-elements for strontium, where the Rydberg states of a divalent atom are treated as a single electron moving in a model potential. This allows us to simulate Stark maps, which has in turn enabled us to calibrate the electric field we can create with our electrodes, and gives us confidence in the accuracy of our dipole matrix-element calculations. The agreement between the single-electron model and experiment is very good, without including interactions between the valence electrons in the model.

With the dipole matrix-elements, we have characterized the interaction potential between strontium atoms. This has shown that the interaction between $^1S_0$ states is always attractive, and that the interaction between $^1D_2$ states is repulsive for most states with $n > 15$. The interaction strengths between Rydberg atoms in $^1S_0$ states, calculated with the single-electron model, agree with values calculated with a two-electron Hartree-Fock method [1].

A knowledge of the interaction strengths is essential for the long-term goals of the strontium project, such as producing a dipole blockaded gas, and for unraveling the complicated interaction processes in a Rydberg gas.

Part II

Two-electron excitation of a strontium Rydberg gas

Chapter 5

Autoionization of a cold Rydberg gas

Introduction

The key reason for using an alkaline earth element, such as strontium, in a Rydberg gas experiment, as opposed to the more commonly used alkali metals, is the additional valence electron. The creation of our Rydberg gas involves the excitation of only one of the valence electrons to a $5snl$ state. However, the inner valence electron in the $5s$ state can also be excited.

In our experiments light at ~ 408 nm is used to excite from the $5snl$ Rydberg state to a $5p_{3/2}nl$ doubly excited state, as illustrated in fig. 5.1. This technique, where each electron is separately excited, is known as isolated core excitation (ICE) [146]. If the wavefunctions of the excited inner valence and Rydberg electrons have significant overlap then the atom ionizes, a process called "autoionization". The decay of the autoionizing state to the continuum (ionization), is very rapid, and is the dominant decay route.

For doubly excited states with angular momentum $l \gtrsim 8$ the spontaneous decay of the Rydberg electron back to the ground state is the dominant decay route [147], as the inner valence and Rydberg electron wavefunctions

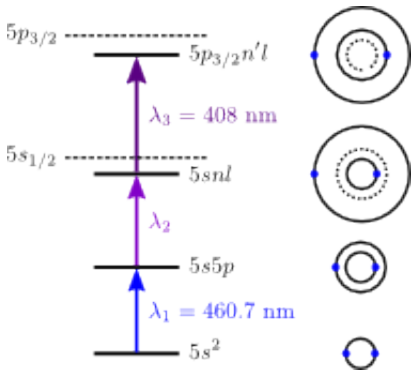

Figure 5.1: The general ICE scheme used in our experiments. The Rydberg state $5snl$ is prepared through a resonant two-step excitation $\lambda_1 + \lambda_2$, and this Rydberg series converges on the ionization limit which would produce a $5s_{1/2}$ ion. A third step λ_3 excites the atom to the $5p_{3/2}nl$ series, which converges on an ionization limit which would produce a $5p_{3/2}$ ion. On the right of the figure is a representation of the electronic excitation at each step.

no longer significantly overlap. The ability to create doubly excited states without autoionization leads to intriguing possibilities such as trapping and imaging Rydberg atoms using their inner valence electron transition. High l states can be prepared through a Stark switching technique, where a high angular momentum state is populated in an electric field, and then retained through an adiabatic lowering of the field, as proposed in [148] and shown in [146]. In this thesis we only study autoionizing states.

In this chapter we present the first study of autoionization in a cold gas. To describe autoionizing transitions, we use multi-channel quantum defect theory (MQDT), which is used to fit the spectra of the autoionizing states. A presentation of the autoionizing resonances we have studied can be found in [12], and a proposal for trapping strontium Rydberg atoms using the inner valence electron in [1]. We also use autoionization as a high time resolution probe of the Rydberg state, with excellent signal-to-noise.

This chapter will:

- Discuss **the spectra of autoionizing states**, how to describe their shape with MQDT, and a comparison of a MQDT model to spectra we have measured, in section 5.1.
- Present the use of **autoionization as a probe of the Rydberg gas**, including the measurement of Rydberg state lifetimes, in section 5.2.

5.1 The spectra of autoionizing states

Strontium atoms in a Rydberg state can be autoionized using a laser $\lambda_3 = 408$ nm, which addresses the $5snl \rightarrow 5p_{3/2}nl$ set of transitions[1]. By varying the frequency ω_3 of the autoionizing laser, the spectrum of the autoionizing transition can be measured. To understand the shape of the autoionizing resonances, they must be analyzed with multi-channel quantum defect theory (MQDT) [145].

This thesis in no way aims to present a review of MQDT (a full review can be found in [145]), nor do we use the theory to preform highly accurate multi-channel spectroscopy. Previous work has studied the $5sns$ [123] and $5snd$ [150] autoionizing series of strontium in detail. However, a short introduction to the theory is required for clarity. MQDT as a theoretical framework considers atomic resonances in terms of series of states (and their respective degenerate continua), or "channels", and the coupling between the channels, as opposed to on a state-by-state basis. In this aspect it is deeply analogous to scattering theory. The energy structure of each channel is encoded in the quantum defect, which is a powerful way of parameterizing complicated core penetration effects. It is presumed that the defects are constant in energy [151], which is true far into the Rydberg series.

[1] The $5snl \rightarrow 5p_{1/2}nl$ transitions are at ~ 422 nm [149].

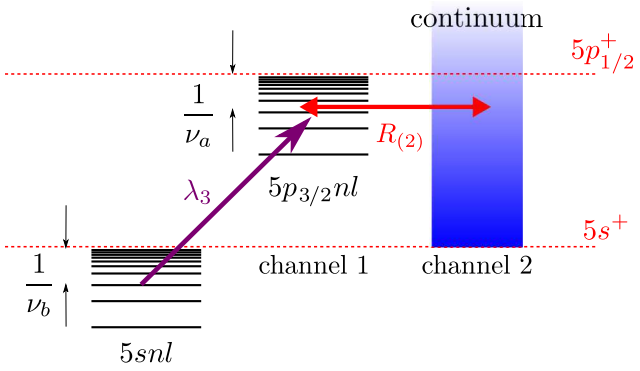

Figure 5.2: A two-channel MQDT model for ICE in strontium. The atom is excited from a Rydberg state $5snl$ to an autoionizing state $5p_{3/2}nl$, which is coupled to the continuum.

The power of MQDT in atomic physics is its ability to describe the extremely complex energy structure of multi-electron atoms. The coupling of each channel to the continuum, and the interaction between channels, has a profound effect upon autoionizing resonances. It should be noted that the parameters required in MQDT are, in general, calculated by fitting a series of the spectra under question. However, there is a body of work that calculates the parameters *ab initio* [26, 145].

Figure 5.2 illustrates the simplest MQDT picture of the ICE scheme that we use. The atom is initially in a Rydberg state $5snl$, at an energy given by the bound (Rydberg) state effective quantum number ν_b, which in turn depends upon the bound state quantum defect δ_b. This Rydberg series tends towards the ionization limit that would produce an Sr^+ ion in the $5s_{1/2}$ state.

The atom is excited from the Rydberg state, with light $\lambda_3 = 408$ nm, to the quasibound (autoionizing) series $5p_{3/2}nl$, which is the first channel. The quasibound series tends towards the ionization limit that would produce an Sr^+ ion in the $5p_{3/2}$ state. The energy of the autoionizing state is given by the quasibound channel effective quantum number ν_a, which in turn depends upon the quasibound channel quantum defect δ_a. The quasibound channel is coupled to the continuum, which is the second channel. The strength of the

coupling between the channels is encoded in the parameter $R_{(2)}$. This is a two-channel MQDT model, involving one quasibound (autoionizing) channel, and an "open" continuum channel. This simple picture depends entirely upon the quantum defects $\delta_{a,b}$ and the two-channel coupling parameter $R_{(2)}$.

Next, MQDT is used to describe the shape of autoionizing resonances.

5.1.1 The shape of the autoionization cross section

We begin by studying the form of the optical cross section σ for the autoionization process (for a full derivation of the cross section see appendix D). For a simple two-channel model (denoted by subscript (2)), with a single autoionizing state coupled to the continuum, the cross section has the form:

$$\sigma_{(2)} = \frac{4\pi^2\omega}{c}|Z_{(2)}|^2|\langle\nu_a l|\nu_b l\rangle|^2|\langle 5p||\hat{T}||5s\rangle|^2\,, \tag{5.1}$$

where ω is the optical frequency of the transition, Z the density of autoionizing states, $\langle\nu_a l|\nu_b l\rangle$ the overlap integral for the Rydberg electron, and $\hat{T}$ the transition dipole operator. The reduced dipole matrix-element for the inner valence electron transition, $\langle 5p||\hat{T}||5s\rangle$, is a constant. Hence, the cross section can be rewritten as:

$$\sigma_{(2)} = A_{(2)}|Z_{(2)}|^2|\langle\nu_a l|\nu_b l\rangle|^2\,, \tag{5.2}$$

where all of the constant terms for a given transition are characterized by the two-channel amplitude $A_{(2)}$.

For the two-channel model illustrated in fig. 5.2 the form of $Z_{(2)}$ is simple [26]:

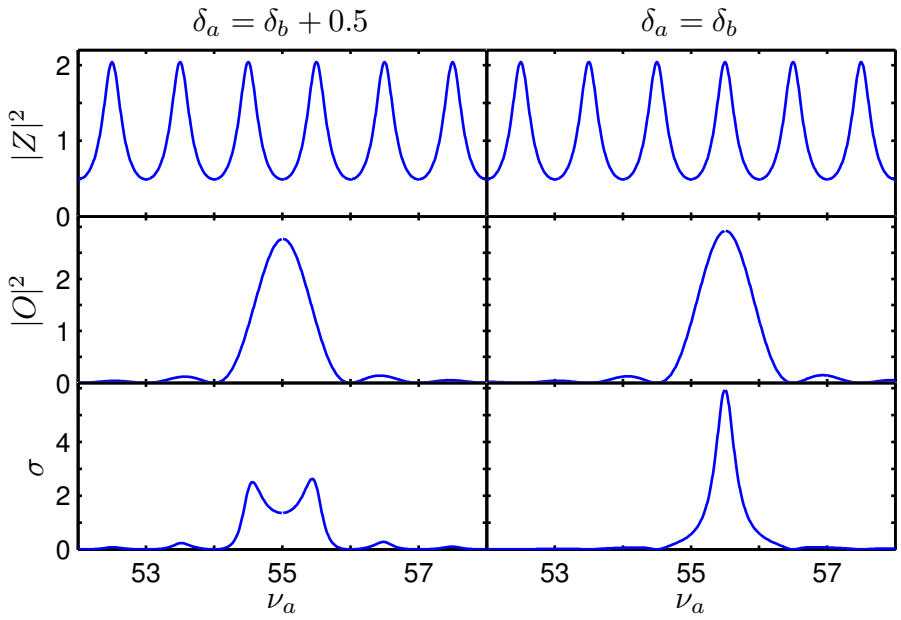

Figure 5.3: The density of states Z, ovelap integral O, and autoionization cross section σ for a two-channel MQDT model. The x-axis ν_a is the effective quantum number for the autoionizing series. The left hand column shows the case where the the quantum defect of the autoionizing series (δ_a) differs from that of the bound series (δ_b) by 0.5. In the right hand column the defects are the same. The effect of this difference on the cross section is clear. The y-axis units are all arbitrary, but comparable to each other.

$$Z^2_{(2)} = \frac{R^2_{(2)}\left(1 + \tan^2\left[\pi(\nu_a + \delta_a)\right]\right)}{R^4_{(2)} + \tan^2\left[\pi(\nu_a + \delta_a)\right]}\,, \tag{5.3}$$

where $R_{(2)}$ is the coupling between the quasibound (autoionizing) channel and the continuum, $\nu_{a,b}$ the effective principal quantum number of the autoionizing and bound states respectively, and $\delta_{a,b}$ the respective quantum defects. The squared density of states $Z^2_{(2)}$ has a series of peaks at the position of the $5p_{3/2}nd$ states (top row of fig. 5.3), and is the probability of finding an autoionizing state at a particular energy (encoded in ν_a). The FWHM Γ_a of the peaks are set by the coupling parameter $R_{(2)}$, and for a two-channel model is given by:

$$\Gamma_a = \frac{2R^2_{(2)}}{\pi\nu_a^3}\,. \tag{5.4}$$

The width Γ_a sets the autoionization rate. The overlap integral between the initial and final state of the Rydberg electron has an analytic form [152]:

$$\begin{aligned}\langle \nu_a d|\nu_b d\rangle &= \frac{2\nu_a^2\nu_b^2}{\pi(\nu_a^2-\nu_b^2)}\sin\left[\pi(\nu_a-\nu_b)\right] \\ &\equiv O(\delta_b,\nu_a)\,.\end{aligned} \tag{5.5}$$

The position of this function, relative to the peak at ν_a in $Z_{(2)}$, is set by the quantum defect of the bound state, δ_b, as is highlighted in the rewriting of the overlap integral as a function $O(\delta_b,\nu_a)$. The shape of O is shown in the middle panels of fig. 5.3.

The shape of the autoionization cross section σ is found through eqn. (5.2), and shown in the bottom row of fig. 5.3. If the quantum defect of the autoionizing series δ_a differs by 0 (mod 1) from the quantum defect of the bound Rydberg state δ_b, then there is a single dominant peak (bottom right pane of fig. 5.3). In this case the outer electron wavefunction for a $5snl$ Rydberg state only has significant overlap with one $5p_{3/2}nl$ autoionizing state. If the quantum defects differ by 0.5 (mod 1) then there is a double peaked structure (bottom left pane of fig. 5.3). This is because the outer electron wavefunction now has overlap with two $5p_{3/2}nl$ states, and the transition strength is consequently weaker [146]. The series of smaller peaks in the wings of the cross section are due to the presence of the other $5p_{3/2}nd$ states, and are known as shake-up satellites [26].

In practice, to fully describe the autoionization process, more than two channels are required, which is discussed below and again in more detail in appendix D.

The width of the autoionization cross section

The autoionization rate Γ_a is given by a simple formula for a two-channel model (eqn. (5.4))[2]. It is useful to know the scaling of Γ_a with the atomic state properties. The width scales with principal quantum number as n^{-3} [26], as can be seen in eqn. (5.4)[3]. This is illustrated in fig. 5.4(a), which shows six-channel MQDT simulations of the autoionization cross section for various $5snd \rightarrow 5p_{3/2}nd$ autoionizing transitions.

The width of the autoionization spectrum depends critically upon the angular momentum state l of the Rydberg electron, as shown in the experimentally measured decay rates in fig. 5.4(b), but there is no simple scaling law. At $l < 3$ the decay rate is suppressed, as the Rydberg electron has a significant probability of penetrating the core, and hence interacts less with the inner valence electron. By $l = 3$ the probability of penetrating the core is minimal (the quantum defect is small), and there is an enhanced probability for the Rydberg electron to scatter from the inner valence electron (autoionization). For $l > 3$ the orbit of the Rydberg electron becomes increasingly circular, and the probability of autoionization drops exponentially. By $l = 8$ the Rydberg electron is more likely to decay through spontaneous emission of a photon than by autoionization, hence the leveling out of the decay rate in fig. 5.4(b), and this becomes the dominant decay rate [147].

The exact point at which these regimes of different autoionization rate scaling are reached depends upon the atom, and the data presented in fig. 5.4(b) is for barium. As an example, the quantum defect for the $6s50d\,^1D_2$ state in Ba is 2.69 [153], and in Sr the $5s60d\,^1D_2$ state quantum defect is 2.37 [109]. This implies that the autoionization width should start decreasing in Sr at *lower* l than in Ba because there will be less core-penetration (smaller quan-

[2] For models with more channels, the two channel coupling parameter $R_{(2)}$ is replaced by a sum over all of the R coupling parameters (see appendix D).

[3] This is only true for $n >> l$ [26].

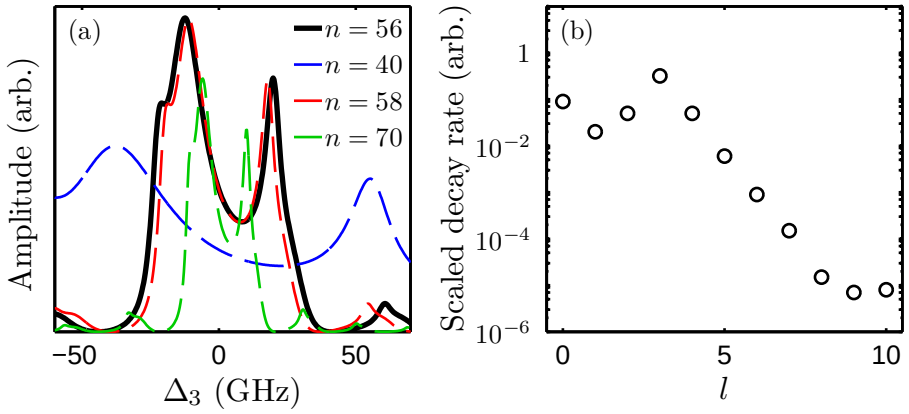

Figure 5.4: (a) Simulated autoionization spectrum for strontium $5snd\,{}^1D_2$ states, for various n. The models use MQDT parameters for the $56\,{}^1D_2$ state (solid black line), with arbitrary amplitude scaling. (b) Variation in the autoionization decay rate with the angular momentum l of the Rydberg electron, scaled to remove n dependence, for barium. Reproduced from fig. 10 in [147].

tum defect). A preliminary study, considering our measured autoionization spectra, suggests that the turning point is at $l = 2$ in Sr, as compared to $l = 3$ in Ba.

5.1.2 Fitting the spectra

Only considering a single autoionizing channel and it's coupling to the continuum (a two-channel MQDT model) is over simplistic. It has been found that a total of six channels are required to reproduce the autoionization spectra of the ${}^1S_0$ and ${}^1D_2$ series in strontium [150]. The additional channels are other doubly excited configurations and their respective continua. The above conclusions as regards to the shape and width of the autoionization spectra remain broadly true for the six-channel model, however there is now interference between the spectral densities Z for the different quasibound channels, leading to more complicated lineshapes, and larger cross sections due to the presence of additional decay routes. The six-channel model is fully discussed and derived in appendix D.

The standard unit of autoionization laser frequency we use is the detuning Δ_3 from the ion line $5s_{1/2} \rightarrow 5p_{3/2} = 407.88$ nm [149]. To acquire the spectrum of the autoionizing states the level of ionization that is produced at each detuning Δ_3 is recorded. The autoionization signal $S(\Delta_3)$ is related to the autoionization cross section for a specific angular momentum state σ_L through

$$S(\Delta_3) = \eta N_L \sigma_L(\Delta_3)\,, \tag{5.6}$$

where η is a constant factor that accounts for the detection efficiency and signal-per-ion conversion factor, and N_L is the number of atoms in the Rydberg state. Hence, the autoionization signal $S(\Delta_3)$ is directly proportional to the autoionization cross section $\sigma(\Delta_3)$, and in this way the experimental data can be fit.

The full form of the autoionization cross section $\sigma(\Delta_3)$, the required fitting parameters, and a comparison of these fitting parameters to previous studies can be found in appendix D.

5.1.3 Results

We have studied the autoionizing resonances of three states: $5s19d\,^1D_2$, $5s20s\,^1S_0$ and $5s56d\,^1D_2$. The autoionizing laser λ_3 for experiments on the first two states is a pulsed dye laser, and for the latter a diode laser. The experimental techniques for performing measurements using autoionization will be discussed in section 5.2.

A study of the $5s56d\,^1D_2$ autoionization spectrum at high Rydberg densities reveals the presence of interactions in the Rydberg gas, as will be the subject of chapter 6. The data in this chapter is taken in the non-interacting regime.

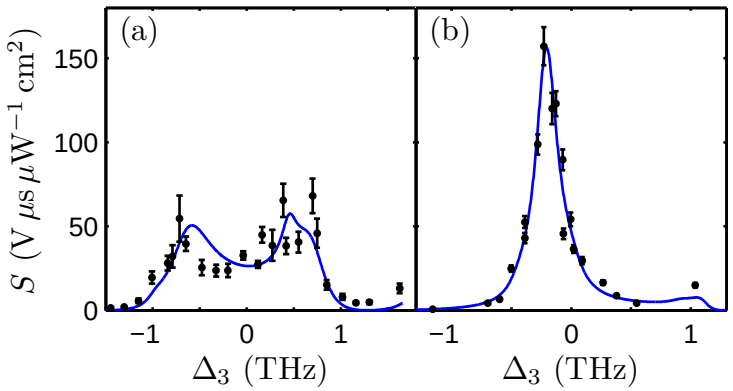

Figure 5.5: (a) The autoionization spectrum of the $5s19d\,^1D_2$ state. (b) The autoionization spectrum of the $5s20s\,^1S_0$ state. Solid lines are six-channel MQDT model fits, and the fit parameters are listed in tables D.2 and D.1.

The autoionization spectra of the $5s19d\,^1D_2$nd $5s20s\,^1S_0$tates

Figures 5.5(a) and (b) show the experimentally measured autoionization spectra (black points) of the $5s19d\,^1D_2$ and $5s20s\,^1S_0$ states. As can be seen, these spectra are extremely broad, $\sim$ 1 THz, and could only be acquired by exploiting the tunability of a dye laser system. These spectra are measured Δt = 0.5 μs after the end of the Rydberg excitation, with a Rydberg excitation laser power of $P_2 = 5.5$ mW (for more detail see section 5.2).

The solid blue lines on fig. 5.5 are the six-channel MQDT model fits to the data, as detailed in appendix D. Note the similarity between the measured spectra in fig. 5.5 and the autoionization cross sections in the lower panel of fig. 5.3. For the $^1D_2$ states the difference between the autoionizing and bound state quantum defects $\delta_a - \delta_b \approx 0.43$, so a double peaked autoionization spectrum is expected by the analysis in section 5.1.1. For the $^1S_0$ state $\delta_a - \delta_b \approx 0.15$, so a predominantly single peaked, slightly asymmetric autoionization spectrum is expected. These measured spectra and MQDT models are presented in [12].

The agreement between the data and the models in fig. 5.5 is good, particularly for the $20\,^1S_0$ state. A major cause of disagreement will be amplitude

noise in the data, since the pulsed laser exhibits large intensity fluctuations. The six-channel model for the $^1D_2$ states may be incorrect, due to the inclusion of an unweighted sum over $|J, M_J\rangle$ components (see appendix D).

The autoionization spectrum of the $5s56d\,^1D_2$tate

Figure 5.6 shows the experimentally measured autoionization spectrum (black points) of the $5s56d\,^1D_2$ state. This spectrum is broad, $\sim$ 50 GHz, and was acquired through course tuning[4] of the diode laser that provides λ_3. This spectrum is measured Δt = 0.5 μs after the end of the Rydberg excitation, with a Rydberg excitation laser power of $P_2 = 1$ mW (for more detail see section 5.2).

For comparison, fig. 5.6(a) includes a two-channel MQDT model fit, and fig. 5.6(b) a six-channel fit (solid blue lines). The six-channel model is clearly in better agreement with the data. In particular the difference in width of the two peaks in the measured spectrum is reproduced in the six-channel model through interference between the density of states Z for the different quasibound channels.

The spectrum in fig. 5.6 has the expected shape, since the difference between the autoionizing and bound state quantum defects is $\delta_a - \delta_b \approx 0.43$. A difference of 0.5 leads to an exactly symmetric double-peaked spectrum, as discussed in section 5.1.1.

Discrepancies between the data and the six-channel model in fig. 5.6(b) may be due to frequency measurement uncertainty caused by the coarse tuning of the autoionization diode laser, and the inclusion of an unweighted sum over $|J, M_J\rangle$ components in the model (see appendix D). The six-channel MQDT model is optimized to reproduce the $56\,^1D_2$ state autoionization spectrum, hence the fit is better than to the $19\,^1D_2$ state spectrum in fig. 5.5(a). To

[4] The diode laser is tuned through large adjustments of the feedback grating, and adjustment of the diode supply current and temperature

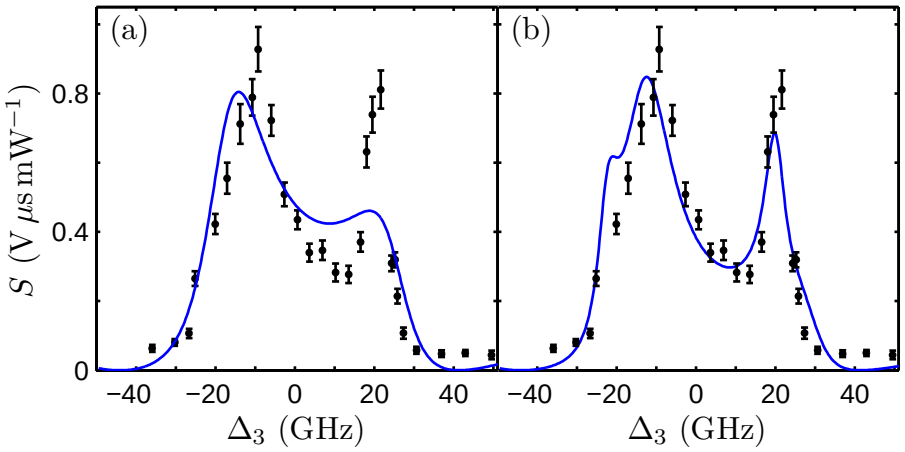

Figure 5.6: The autoionization spectrum of the 56 $^1D_2$ Rydberg state, taken with$P_2 = 1\ mW$. (a) includes a two-channel MQDT model fit (blue line) with a quasi-bound state quantum defect for the autoionizing $5p_{3/2}56d$ state $\delta_a = 2.77$, and a single two-channel $R_{(2)} = 0.77 \pm 0.02$. (b) includes the full six-channel MQDT model fit (blue line). The fit parameters can be found in table D.2.

perform a full and proper analysis a whole series of autoionizing spectra must be analyzed, as in [123, 150].

Conclusion

We are able to describe the shape of the autoionization spectra reasonably well. This will prove to be essential when investigating interactions in our Rydberg gas, as will be the subject of chapter 6.

It is important to note the width of these spectra, which is on the order of 50 GHz to 1 THz. The width indicates that autoionization is an extremely likely process, and that the lifetimes of the quasibound autoionizing states are extremely short. In the next section we show that autoionization can be used as a probe of the Rydberg state with high signal-to-noise, and that by using the pulsed laser measurements can be made with a high time-resolution. Due to the large width of the autoionization spectra the large bandwidth of a pulsed laser is not an issue.

5.2 Autoionization as a probe of the Rydberg gas

In chapter 3, atoms in the Rydberg state are detected by observing their spontaneous ionization. By using isolated core excitation (ICE) the atoms in the Rydberg state can be autoionized. The number of ions that are created due to autoionization are proportional to the number of atoms in the Rydberg state, through eqn. (5.6). The cross section for autoionization is large; the consequence of this being that far more ions are produced through autoionization (in general) than through spontaneous ionization.

By using autoionization the time at which the Rydberg state population is probed is well defined as the time at which the atoms are exposed to the autoionizing light. As in the previous section, the $5s19d\,^1D_2$, $5s20s\,^1S_0$ and $5s56d\,^1D_2$ states are investigated. In this section, the autoionization technique is characterized, and time-dependent measurements of the Rydberg state population are made. We also consider what conclusions can be drawn on the exact population of the Rydberg state.

5.2.1 General technique

Atoms are prepared in the Rydberg state using the step-scan technique described in chapter 3. In all of the experiments presented in this chapter $\lambda_1 = 461$ nm is set to a power $P_1 = 0.6$ mW ($0.6I_{\text{sat}}$). To access the $5s19d\,^1D_2$ and $5s20s\,^1S_0$ states the laser $\lambda_2 = 420$ nm is used, with a power $P_2 = 5.5$ mW, and a $1/e^2$ beam waist of ~ 0.5 mm. The $20\,^1S_0$ state is the closest singlet state in energy to the $19\,^1D_2$ state, and is 63 GHz higher in energy. To access the $5s19d\,^1D_2$ state the laser $\lambda_2 = 413$ nm is used, with a power $P_2 = 26$ mW, and a $1/e^2$ beam waist of 0.8 mm parallel to the optical bench, and 0.4 mm normal to the bench. All of the states are located using the line positions from [111].

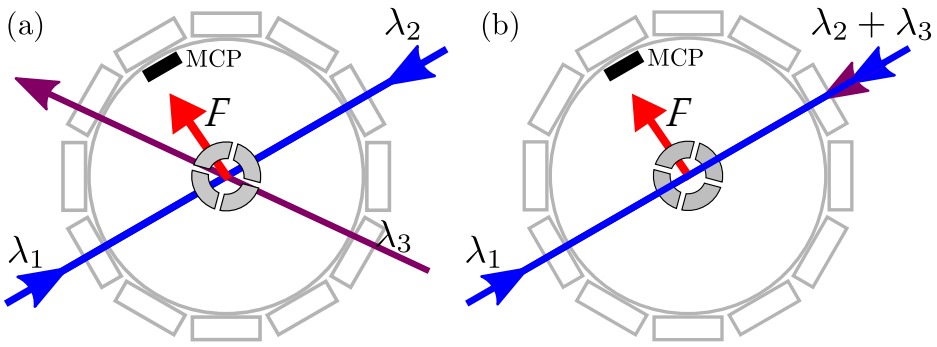

Figure 5.7: Geometry of the beams through the main chamber, for (a) the experiments on the $19\,^1D_2$ and $20\,^1S_0$ states, and (b) the experiments on the $56\,^1D_2$ state. Not to scale. The angle between each viewport is 30°.

The singly excited Rydberg state is excited to the doubly excited autoionizing state using a third laser $\lambda_3 = 408$ nm, as illustrated in fig. 5.1. The spectrum of the autoionizing transition is very broad (see section 5.1.2), so λ_3 does not need to be frequency stabilized. For the $19\,^1D_2$ and $20\,^1S_0$ states λ_3 is provided by a tunable pulsed dye oscillator/preamplifier. The pulse width is 10 ns, with a repetition rate of 10 Hz, and a non-transform limited bandwidth of ~ 2 GHz. The pulse energy varied significantly over the course of these experiments, but ranged from $0.1 - 20$ μJ per pulse. The size of the beam at the chamber was resized over the course of these experiments, but ranged from a $1/e^2$ waist of $1.3 - 2.1$ mm. For the $56\,^1D_2$ state λ_3 is provided by a grating stabilized diode. This diode gives a maximum power at the chamber of ~ 1.6 mW, with a beam waist of 0.9 mm parallel to the optical bench, and 1.3 mm normal to the bench. The geometry of the beams $\lambda_{1,2,3}$ relative to the main chamber is shown in fig. 5.7.

The timing diagram for the autoionization experiments on the $19\,^1D_2$ and $20\,^1S_0$ states is shown in fig. 5.8(a). Data is acquired with the step-scan technique, as illustrated in fig. 3.5, and the additions for the autoionization experiments are as follows:

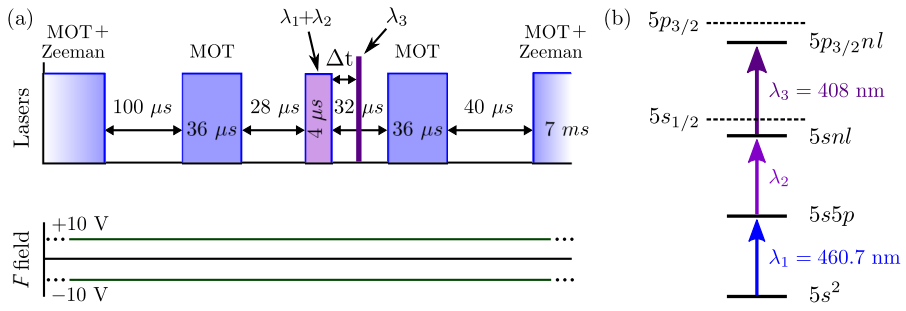

Figure 5.8: (a) Timing diagram for the excitation sequence in the step-scan technique, using autoionization. The electric field is constantly applied for the $19\,^1D_2$ and $20\,^1S_0$ states, and pulsed for the $56\,^1D_2$ state. The autoionization pulse λ_3 is delayed from the end of the Rydberg excitation by a delay Δt. (b) Level diagram for the autoionization experiments. Atoms are transferred to the Rydberg state with the pulse $\lambda_1 + \lambda_2$. The Rydberg atoms are autoionized with a pulse λ_3.

- The autoionizing laser pulse λ_3 arrives at a time Δt after the end of the Rydberg excitation $\lambda_1 + \lambda_2$.
- The Stark shifts of the $19\,^1D_2$ and $20\,^1S_0$ states with an applied field of ~ 4 V cm^{-1} are ~ 5 MHz and ~ 2 MHz respectively. These are small compared to the Rydberg excitation linewidth (which we measure to be $2\pi \times 32$ MHz), so an electric field of 4.2 V cm^{-1} is left on *continuously* to accelerate ions to the micro-channel plate detector (MCP).
- The MCP grid is held at a constant -25 V for these experiments.

There are some minor differences from fig. 5.8(a) when using the diode laser to autoionize the $56\,^1D_2$ state. These are as follows:

- The autoionizing laser pulse λ_3 is 4 μs long, as opposed to the 10 ns dye laser pulse, and arrives at a delay Δt after the end of the Rydberg excitation $\lambda_1 + \lambda_2$.
- The Stark shift of the $56\,^1D_2$ state is significant, and so a 4 μs long, 4 V cm^{-1} pulse of electric field is applied 500 ns after the end of the autoionizing pulse to accelerate ions to the MCP.

- The $56\,^1D_2$ state has a much longer lifetime than the lower n states (~ 25 μs as opposed to ~ 1 μs). Practically this means we are unable to use a second MOT light pulse, and the loss fraction cannot be measured. The longer excitation sequence means that the MOT is refilled for 30 ms.

- The MCP grid is held at a constant -40 V for these experiments.

The process of measuring the MOT population and density is identical to the step-scan technique presented in chapter 3. When an atom is excited to an autoionizing state it ionizes. These ions are directed to the MCP using an electric field. Autoionization produces, in general, significantly more ions than the spontaneous ionization from the Rydberg gas, as can be seen in fig. 5.9(a).

An example step-scan spectrum, with (blue crosses) and without (black dots) autoionization is shown in fig. 5.9(b). The frequency offset between these spectra is due to a drift in the wavemeter calibration. These two step-scan spectra show that autoionization can be used to perform Rydberg state spectroscopy, but with much greater signal-to-noise than by observing spontaneous ionization (the noise floor is the same with either technique).

The peak autoionization signal on the step-scan spectrum is taken as the on-resonance autoionization signal. Standard functions such as a Gaussian or Lorentzian do not, in general, fit the data well, so a fitted maximum is not taken. The peak ion signal is normalized by the ground state atom number. For the $19\,^1D_2$ and $20\,^1S_0$ states the peak ion signal is also normalized by the pulse laser intensity[5] I_3 (not the power P_3 because the beam was resized in the course of these experiments), yielding a standard autoionization signal

[5] The power of the pulsed laser λ_3 is measured over several seconds, and converted to intensity. After passing through the main chamber the pulse intensity is measured on a photodiode, and averaged over the 100 cycles of the excitation sequence. The ion signal is also normalized by this step-to-step intensity fluctuation.

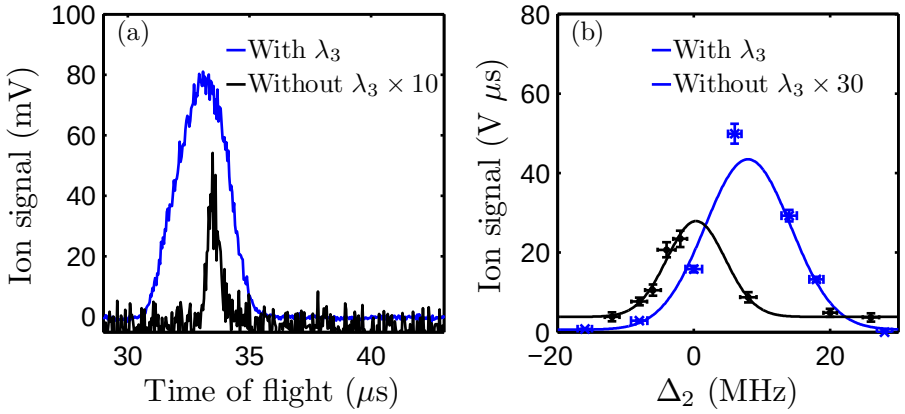

Figure 5.9: (a) Example averaged (×100) ion signals as they arrive on the oscilloscope, with (blue) and without (black) the autoionizing light λ_3, for the $56\,^1D_2$ state. The spontaneous ionization signal has been multiplied by 10 for clarity. (b) The spectra taken by stepping the Rydberg laser frequency ω_2 over the $56\,^1D_2$ resonance, with (blue crosses) and without (black points) λ_3, including Gaussian fits (solid lines). The detuning is relative to our measured state energy. The signal from the spontaneous ionization has been multiplied by 30 for clarity.

S with units $\mathrm{V}\,\mu\mathrm{s}\,\mu\mathrm{W}^{-1}\,\mathrm{cm}^2$ per 10^6 atoms. For the $56\,^1D_2$ state the peak autoionization signal is normalized by the power P_3 of the autoionizing laser, yielding a standard signal S with units $V\,\mu\mathrm{s}\,\mathrm{mW}^{-1}$ per 10^6 atoms.

It should be noted that both the ground state atom number and density fluctuate between experiments, and some of the signals in this part of this thesis depend non-linearly on the Rydberg atom density (which will depend upon the ground state density). In general the ground state atom number was $1-4\times10^6$, and the density $2.5-4.5\times10^{10}$ cm^{-3}, unless otherwise stated.

For the experiments on the $56\,^1D_2$ state, each experiment is repeated with and without the autoionization pulse λ_3, so that the spontaneous ionization contribution can be subtracted from the total ionization signal. This is not necessary for the experiments on the $19\,^1D_2$ and $20\,^1S_0$ states since, for $\Delta\mathrm{t} < 1\ \mu$s, the autoionization signal is ~ 200 times larger than the spontaneous ionization signal.

Now that the experimental sequence has been fully described, the results of using autoionization as a probe of the Rydberg state population will be presented.

5.2.2 Variation of the autoionizing laser power

The $5s19d\,^1D_2$nd $5s20s\,^1S_0$tates

The effect of varying the autoionizing laser intensity I_3 upon the level of autoionization of the $19\,^1D_2$ and $20\,^1S_0$ states is presented. To perform these experiments the autoionizing laser λ_3 is set to $\Delta_3 \approx -710$ GHz for the $19\,^1D_2$ state, and $\Delta_3 \approx -150$ GHz for the $20\,^1S_0$ state (these seem like large detunings, but note the width of the autoionization spectra in fig. 5.5). The delay is set to $\Delta t = 0$.

The intensity I_3 of the autoionizing pulsed laser λ_3 is varied using neutral density filters. Figure 5.10(a) and (c) show the variation in the autoionization signal with I_3 for the two Rydberg states (black crosses). The signal seems to saturate rapidly in both cases. This could suggest all of the Rydberg atoms are autoionized.

However, evidence against this conjecture is provided by figs. 5.10(b) and (d). In these figures the ground state population of the MOT is varied by varying the power of the Zeeman slower beam[6]. As the number of ground state atoms increases one would expect a linear increase in the number of Rydberg atoms (interaction effects between the Rydberg atoms are negligible for experimentally feasible Rydberg atoms densities in this region of n); for fixed I_3 one would expect the autoionization signal to increase linearly with ground state population. However, this signal also saturates, suggesting that the MCP is saturating, which seems very likely when looking at the severely

[6] We do not measure a significant change in size of the trapped cloud using when varying the Zeeman slowing beam power.

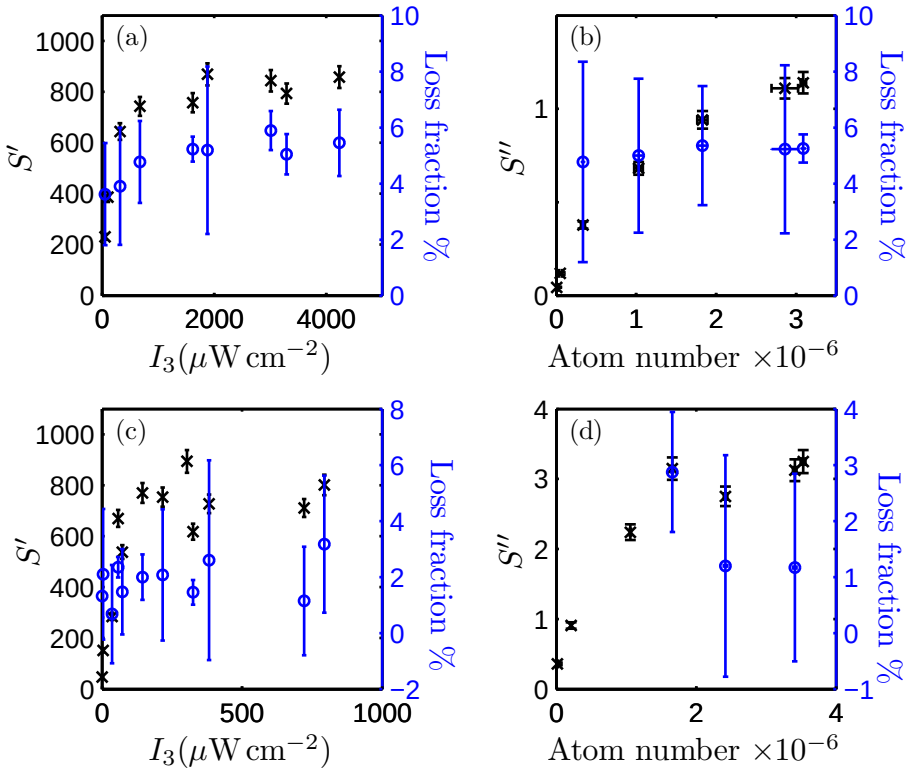

Figure 5.10: (a,c) Variation in the autoionization signal (black crosses) and loss fraction (blue circles) with the autoionizing laser intensity I_3 for the (a) $19\,^1D_2$ and (c) $20\,^1S_0$ state. (b,d) Variation in the autoionization signal and loss fraction with the initial ground state atom number for the (b) $19\,^1D_2$ and (d) $20\,^1S_0$ state. S' is not normalized by I_3, so has units of V μs per 10^6 atoms, S'' is not normalized by the atom number, and so has units of V μs μW^{-1} cm^2. All taken at a delay Δt = 0.

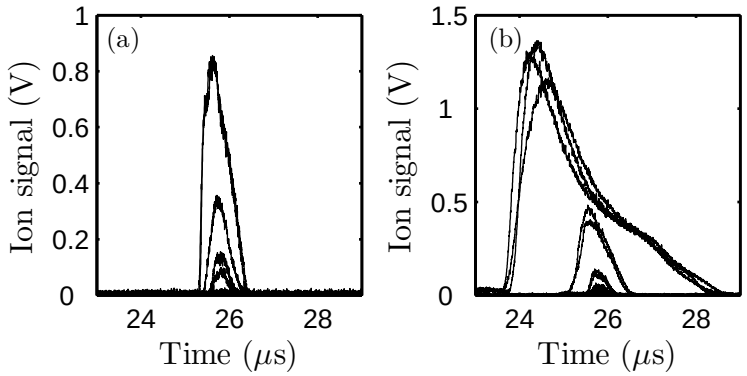

Figure 5.11: The autoionization signal for the $19\,^1D_2$ state, for an initial MOT population of (a) $5{\times}10^4$ and (b) $1{\times}10^6$ atoms and $I_3 = 2250\ \mu\mathrm{W\,cm^{-2}}$. The multiple black lines are the different signals as ω_2 is stepped across resonance. There is clearly a drastic change in the shape of the signal when the population is higher, which we attribute to detector saturation.

distorted ion signals in fig. 5.11.

Saturation of micro-channel plate detectors has been extensively studied in [154], and can be adjusted for [38]. We do not carry out this adjustment here, and ensure that we are below the saturated regime in the experiments below.

The fraction of ground state atoms lost during the Rydberg excitation is also measured in these experiments (blue circles on fig. 5.10). Interestingly, there is no strong evidence of the loss fraction depending *at all* upon the presence of the autoionizing laser λ_3. By the time the loss fraction measurement is made (Δt = 32 μs) $>$ 99% of the Rydberg state population has decayed, presumably to the ground state (as confirmed in [125]). The lack of variation in the loss fraction suggests that only a small fraction of the Rydberg atoms are ionized. Note that these loss fraction measurements are fundamentally different to those analyzed in chapter 3, where the loss fraction was measured while the Rydberg state population was still decaying.

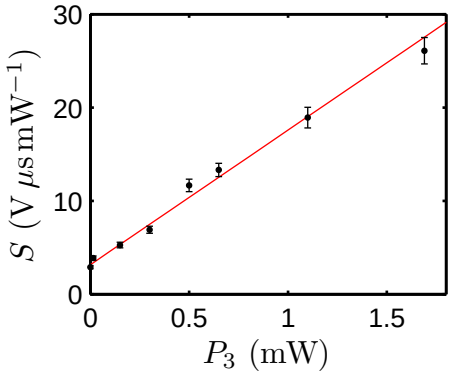

Figure 5.12: The variation in the autoionization signal S, for the 56 $^1D_2$ state, with the power P_3 of the autoionizing laser. The relationship is linear, and there is no evidence of saturation as there was for the lower n states. Δt = 0.5 μs.

The $5s56d\,^1D_2$tate

The variation in the autoionization signal of the 56 $^1D_2$ state with the power P_3 of λ_3 is shown in fig. 5.12. The power P_3 is varied with neutral density filters. The laser λ_3 is set to $\Delta_3 \approx -10$ GHz, and the data is taken at a time Δt = 0.5 μs.

The variation of the autoionization signal with P_3 is linear, unlike the case at lower n (figs. 5.10(a) and (c)). The data in fig. 5.12 was tested for saturation behavior through a χ^2 analysis, and a straight line was found to be a better fit than a saturation curve. There is no evidence of saturation in the time resolved ion signals for this state, as there were for the lower n states (fig. 5.11).

The y-axis offset is the spontaneous ionization from the Rydberg gas. The level of this ionization depends critically upon the power P_2 of the Rydberg excitation laser, and will be considered in chapter 6. The loss fraction was not measured for the 56 $^1D_2$ state.

Time evolution measurements

The analysis of the time evolution of the $5s56d\,^1D_2$ Rydberg state population proves to be essential in understanding interactions in the Rydberg gas, and will be considered in chapter 6.

Autoionization of the $5s19d\,^1D_2$ and $5s20s\,^1S_0$ states is performed in the presence of a continuous electric field, as illustrated in fig. 5.8(a). If the autoionizing pulse is well separated in time from the Rydberg excitation pulse then the continuous field allows the ions created through autoionization to be differentiated from those created by spontaneous ionization. An example where this condition is met is shown in fig. 5.13. The spontaneous ionization signal (marked A on fig. 5.13) is spread in time over ~ 4 μs, corresponding to the 4 μs Rydberg excitation. At a delay $\Delta t = 2.2$ μs, the atoms are autoionized. The autoionization signal (marked B on fig. 5.13) arrives as a ~ 1 μs burst.

By varying the delay Δt the time evolution of the Rydberg state population can be mapped [12]. The delay Δt is defined relative to the Rydberg excitation pulse, as shown in fig. 5.8, with $\Delta t = 0$ being defined as autoionization pulse arriving at the end of the Rydberg excitation (more exactly, at the time when the intensity of the $\lambda_1 = 461$ nm pulse has fallen to 50%). Since the autoionization and spontaneous ionization signals are separable, and the spontaneous ionization signal is independent of Δt, the spontaneous ionization signal is subtracted from the *total* ionization signal, leaving *just* the signal due to the autoionization of the Rydberg atoms. Hence, the time evolution measurements solely reflect the time evolution of the Rydberg state population.

Figure 5.14(a) shows an example of the change in autoionization signal as Δt is varied, for the $19\,^1D_2$ state. Initially the autoionization signal increases as λ_1 and λ_2 are pulsed on simultaneously (for 4 μs, marked at the grey region

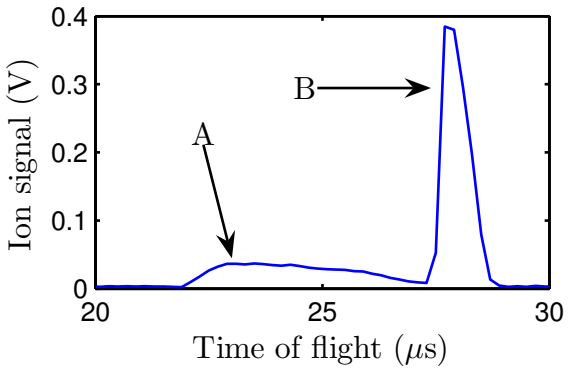

Figure 5.13: An example of the ion signal (after 100 averages), for the 19 $^1D_2$ state. The delay $\Delta t = 2.2$ μs. The low hump A is the spontaneous ionisation from the 4 μs long Rydberg excitation, and the spike B is the autoionization from the 10 ns long autoionizing pulse.

on fig 5.14[7]). The signal reaches an equilibrium value, and then at $\Delta t = 0$, when λ_1 and λ_2 are switched off, begins to decay.

By fitting an exponential to the decay of the autoionization signal the lifetime of the Rydberg state can be extracted (see fig. 5.14(b)). For the 19 $^1D_2$ state we measure a lifetime of 880 ± 30 ns. A previous measurement found a lifetime of 738 ± 37 ns [155] for this state. We do not understand the discrepancy between our measurement and the previous work. An explanation may be imperfect background spontaneous ionization subtraction, which would boost the signal at longer times, enhancing our lifetime measurement. Another explanation could be that the previous study [155] measured the fluorescence from the decay of the Rydberg state, and if a range of Rydberg states were populated then multiple decays will have been recorded simultaneously, distorting the lifetime measurement.

We measure a lifetime of 3.1 ± 0.1 μs for the 20 $^1S_0$ state. The lifetimes of the $^1S_0$ series have not measured this far in n [156]. The lifetime of the 20 $^1S_0$ state is consistent with recent theoretical work [1] that considers spontaneous

[7] There is a small delay of ~ 200 ns between triggering the Rydberg excitation pulse, and it arriving at the chamber, due to the AOM response and rise time.

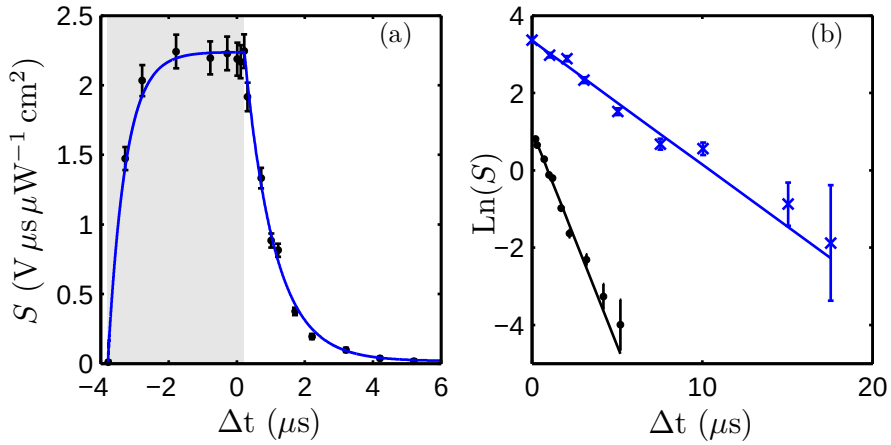

Figure 5.14: (a) The variation in the autoionization signal (black dots) with Δt, for the 19 $^1D_2$ state. The grey region marks the Rydberg excitation pulse, the blue solid line is the solution to the optical Bloch equations. (b) The decay of the 19 $^1D_2$ (black dots) and 20 $^1S_0$ (blue crosses) autoionization signals, with single exponential fits (solid lines). The data in this figure was taken at $\Delta_3 \approx -840,\ -150$ GHz for the 19 $^1D_2$ and 20 $^1S_0$ states respectively.

and blackbody induced decay.

We use the measured lifetime for the 19 $^1D_2$ state, the measured laser intensities of λ_1 and λ_2, and the oscillator strength for the Rydberg transition from [157], to solve the three level optical Bloch equations for the scheme $5s^2\,{}^1S_0 \rightarrow 5s5p\,{}^1P_1 \rightarrow 5s19d\,{}^1D_2$. The result is shown as the solid blue line on fig. 5.14(a). The model is matched to the data using a single fitting parameter: an absolute signal height scaling. The agreement is excellent. This indicates that the autoionization signal follows the Rydberg state population.

The ability to map the Rydberg excitation in such temporal detail highlights a real strength of using autoionization as a probe. The time resolution is set by the length of the laser pulse, which is only 10 ns in these experiments. The large bandwidth of the pulse is not important, since (as shown in section 5.1) the autoionization resonances are THz wide in this region of n. Other experiments have used fs autoionizing pulses to observe the exact inter-electron interaction effects in alkaline earth metal elements [158].

Conclusion

In this chapter we have constructed six-channel multi-channel quantum defect models that describe the autoionization spectra that we measure, and we have understood their shape. By creating Rydberg atoms in high angular momentum states, doubly excited states that do not autoionize can be created. These inner valence electron, non-autoionizing transitions could be used to image or even laser cool Rydberg atoms.

We have shown that autoionization can be used as an extremely effective probe of the Rydberg state population, with high signal to noise. This enables us to study states that are only weakly excited, such as the $5s54f\ ^1F_3$ state in fig. 4.2(b). The autoionization technique can be used to make measurements with high time-resolution (as opposed to the spontaneous ionization technique, which is not time-resolved), which enables us to map the variation is Rydberg state population with time. We have confirmed that the autoionization signal is proportional to the Rydberg state population.

In the next chapter we will show that autoionization can be used to probe the population dynamics and state distribution in the Rydberg gas, through an analysis of the autoionization spectra.

Chapter 6

Using autoionization to study an interacting Rydberg gas

Introduction

In the last chapter autoionization was used as a probe of the Rydberg state population. The autoionization spectrum, and the theoretical framework to reproduce it (multi-channel quantum defect theory, MQDT), was introduced. The spectrum was shown to be dependent upon the *state* of the Rydberg atom.

We have developed a new use for MQDT. In this chapter, it will be shown that autoionization can provide state selective information about a gas of Rydberg atoms, and that a careful analysis of the autoionization spectra yields quantitative information about state mixing processes in the gas. It has been previously observed that a gas of atoms initially prepared in a well defined Rydberg state undergoes mixing into states of different angular momentum l [159] and principal quantum number n [58]. There are various mechanisms which can cause this mixing, which will be discussed.

We find strong evidence that atoms initially prepared in the $5s56d\,^1D_2$ state are transferred to the nearest dipole-coupled states, through a density-

dependent mechanism which we identify as being the formation of a cold plasma. We probe state mixing at the very onset of plasma formation. The work in this chapter is presented in [11].

This chapter will:

- Present **evidence for state mixing in the Rydberg gas** in section 6.1.
- Present a **comparison with nearest dipole-coupled states**, to discern if these states have been populated, in section 6.2.
- Present an **analysis of the autoionization spectra**, with a quantitative measure of state mixing, in section 6.3.
- Discuss the possible **state mixing processes** in a Rydberg gas, and identify the relevant mechanism in our experiment, in section 6.4.

6.1 Evidence for state mixing in the Rydberg gas

As was shown in the last chapter, the shape of the autoionization spectrum depends upon the state of the atom as a whole, in particular upon the angular momentum state of the Rydberg electron. By carrying out autoionization spectroscopy on the Rydberg gas as a whole, information can be gathered about which states the Rydberg atoms are in.

This is an extremely attractive method of spectroscopy. The scattering rate of the inner valence electron transition is large as compared to that of the Rydberg transition. Any change in the *shape* of the autoionization spectrum can be attributed to a change in *state* of the Rydberg electron.

In this chapter we consider experiments performed upon a gas of atoms

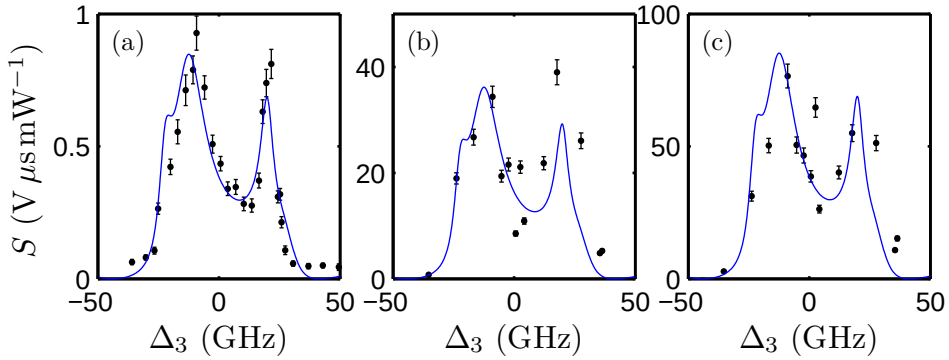

Figure 6.1: Autoionization spectrum of the $5s56d\,^1D_2$ state at $\Delta t = 0.5$ μs for a Rydberg laser power P_2 of (a) 1 mW, (b) 5 mW and (c) 10 mW. The blue line is the six-channel MQDT model for the $56\,^1D_2$ state, optimized to the data in (a), rescaled to fit (b) and (c).

initially excited to the $5s56d\,^1D_2$ state, using the techniques described in chapter 5.

Variation in the autoionization spectrum with Rydberg density

The number and density of Rydberg atoms that are excited can be varied by varying the power P_2 of the Rydberg excitation laser λ_2. It is difficult to know exactly how many Rydberg atoms have been created, the number can be estimated by considering the loss fraction measurements presented in fig. 5.12(a).

The autoionization spectrum of the $5s56d\,^1D_2$ state was presented in the last chapter (fig. 5.6), and found to be well described by a six-channel MQDT model, as can be seen in fig. 6.1(a). This spectrum was taken at $P_2 = 1$ mW, which corresponds to a Rydberg density of $\sim 5 \times 10^8$ cm^{-3}. Since the six-channel MQDT model agrees with the data so well, we can be confident that at this Rydberg atom density the atoms are all in the $56\,^1D_2$ state.

The agreement between the model and the data becomes worse as the density of the Rydberg atoms is increased. In figs. 6.1(b) and (c) the Rydberg atom

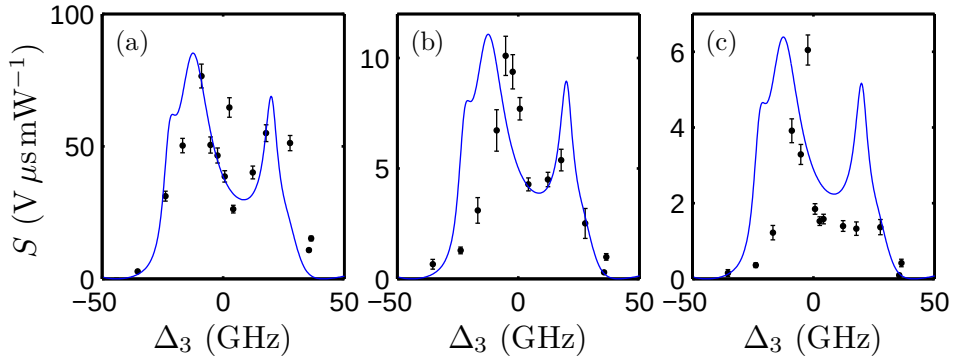

Figure 6.2: Autoionization spectrum of the $56\,^1D_2$ state with $P_2 = 10$ mW for a delay Δt of (a) 0.5 μs, (b) 60 μs and (c) 100 μs. The blue line is a six-channel MQDT model for the $56\,^1D_2$ state.

density is $\sim 3 \times 10^9$ cm^{-3} and $\sim 5 \times 10^9$ cm^{-3}, for powers $P_2 = 5$ mW and $P_2 = 10$ mW respectively. The six-channel $56\,^1D_2$ state MQDT model is compared to the data in each case, with a new amplitude scaling. Although the agreement is worse in general at the higher Rydberg atom density, due in part to the autoionization spectra being acquired with a lower spectral resolution than at the lowest density, there is a systematic deviation at the centre of the spectra. As the power P_2, and hence the density of Rydberg atoms, increases a narrow feature appears at the centre of the autoionization spectrum; this is evidence that the spectrum is dependent upon the Rydberg atom density.

Time evolution of the autoionization spectrum

By taking the autoionization spectrum at different delays Δt, the time evolution of the Rydberg gas can be studied. Figure 6.2 shows the autoionization spectrum at delays of $\Delta t = 0.5, 60$ and 100 μs. The change in the shape of the spectrum is dramatic. The spectrum is initially predominantly double-peaked (the characteristic shape of the $56\,^1D_2$ state autoionization spectrum). As the Rydberg gas is left to evolve the autoionization spectrum loses its double peaked structure and becomes singly peaked.

To highlight this change in shape, the MQDT model for the $56\,^1D_2$ state is marked on the spectra in fig. 6.2 (solid blue lines), and the deviation from this model is clear. The Rydberg gas clearly evolves from mainly being in the $56\,^1D_2$ state to having some other mixture of states. The long-lived peak in this time-evolution data coincides with the density-dependent peak that emerges in fig. 6.1. There is a Rydberg atom density-dependent feature which persists for a longer time than the double-peaked $56\,^1D_2$ state autoionization spectrum.

Variation of state lifetime with spectral position

The decay rate of the autoionization signal varies across the autoionization spectrum[1], as can be clearly seen in fig. 6.2. By fitting a single exponential to the data at each spectral point Δ_3, a lifetime can be extracted. The variation in this lifetime across the autoionization spectrum is shown in fig. 6.3(a). There is a clear peak in the data near $\Delta_3 = 0$. This coincides with the peak visible in the autoionization spectrum of the Rydberg gas at late times, fig. 6.2(c). By taking an average of the lifetimes away from the peak in the data, we ascribe a lifetime of $\tau_{56D} = (24.7 \pm 0.9)\ \mu$s to the $56\,^1D_2$ state. This lifetime is marked on fig. 6.3(a).

Further information is gathered by studying the decay of the autoionization signal in detail. At point A on fig. 6.3(a), the signal is seen to decay exponentially, as shown by the red line on fig. 6.3(b), until it hits the noise floor. A single exponential fit yields the lifetime $24.9 \pm 0.5\ \mu$s at this spectral point, the lifetime ascribed to the $56\,^1D_2$ state.

The decay of the autoionization signal at position B, on the long-lived density-dependent peak, looks markedly different. At short times the signal at point B decays at the same rate as the signal at point A, but at later

[1] These observations are at $P_2 = 10$ mW, and the same was seen at $P_2 = 5$ mW. We did not perform the experiment at lower Rydberg excitation laser powers.

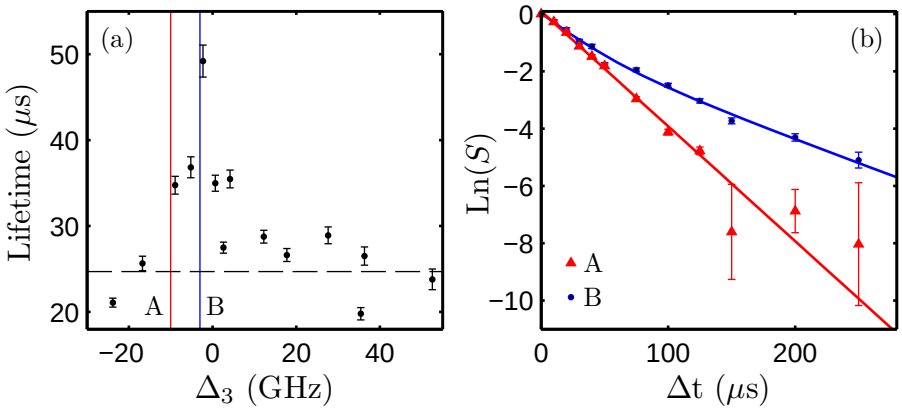

Figure 6.3: (a) Variation in autoionization signal lifetime across the autoionization spectrum, calculated by fitting a single exponential to the decay of the signal. The $56\,^1D_2$ state lifetime is marked with the dashed line. (b) The decay of the autoionization signal (normalized) at the points A and B, as marked on (a). At point A the data (red triangles) is fit with a single exponential decay (red line), and the data hits the noise floor at $\Delta t \approx 150$ μs. At point B the data (blue dots) is fit with a sum of two exponentials (blue line). The data in (a) and (b) is taken with $P_2 = 10$ mW.

times the decay curves diverge. The data at point B exhibits two decay rates, and is fit with the sum of two exponentials (blue line on fig. 6.3(b)). This fit yields a fast decay lifetime of 24.0 ± 1.1 μs, consistent with the lifetime of the $56\,^1D_2$ state, and a slow decay lifetime of 60.2 ± 6.6 μs.

Conclusion

We have observed that: (a) the shape of the autoinization spectrum is density-dependent, with a narrow peak around $\Delta_3 = 0$ appearing at higher Rydberg densities; (b) the shape of the autoionization spectrum evolves over time, with the density-dependent peak persisting for much longer than the wings of the spectrum; (c) the wings of the autoionization spectrum decay at a constant rate, whereas on the long-lived peak the signal decays with a double exponential decay.

These observations are clear evidence that the state of the Rydberg atoms in the gas is changing at high Rydberg atom densities. At low Rydberg density a gas excited to the $56\,^1D_2$ state remains in that state. At higher density there are other, longer-lived states present in the gas. We attribute this to a change in the angular momentum state of the atoms in the gas.

To justify this statement it should be considered that the width of the autoionization spectrum scales with principal quantum number n (as n^{-3} [147]), but scales must more rapidly with angular momentum l. These scalings are illustrated in fig. 5.4. To reproduce anything like the autoionization spectrum narrowing we see at late times in fig. 6.2, without changing l, would require transfer of population to a state of $n \sim 70$. This transfer would also have to be *selective*; population of the n states in between would "smear" the spectra, which we do not observe.

In conclusion, the data strongly suggests that a Rydberg gas of strontium initially excited to the $5s56d\,^1D_2$ state undergoes population transfer to a longer-lived state of different angular momentum, through a Rydberg atom density-dependent process.

6.2 Comparison to the nearest dipole coupled states

When considering state mixing, it makes sense to look at the nearest dipole coupled states. For our system strongest dipole-dipole interaction is $56\,^1D_2 + 56\,^1D_2 \rightarrow 54\,^1F_3 + 56\,^1P_1$ (see section 4.3). The locations of these states are shown on fig. 6.4. The energy defect (see section 4.3) in zero field for this interaction is -2.51 GHz[2]. We measure a state energy of

[2] Figure 6.4 suggests that the energy defect can be tuned with an electric field, which can increase population transfer between states [160, 161]. For the $56D + 56D \rightarrow 54F + 56P$ interaction a field of $\sim 4.3\ \mathrm{V\,cm^{-1}}$ is required to bring the energy defect to zero.

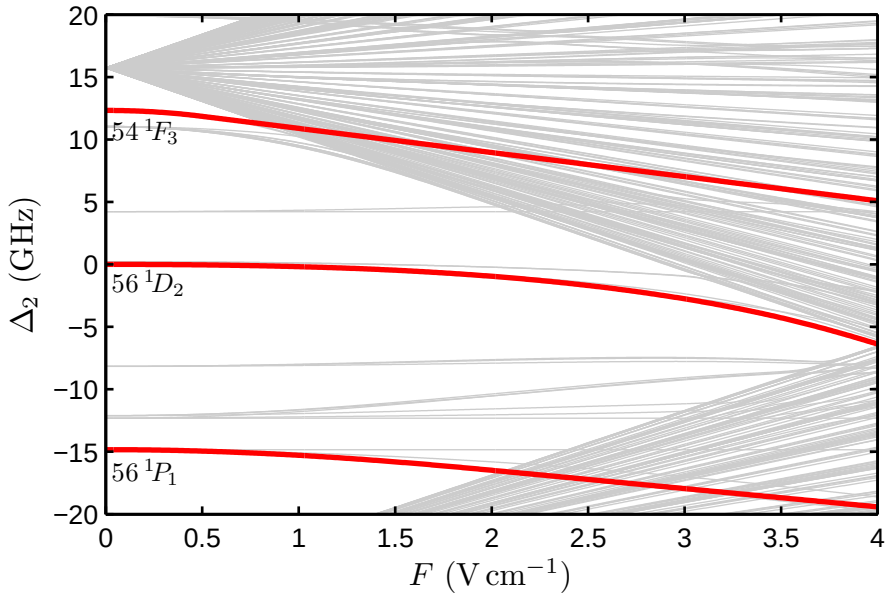

Figure 6.4: Simulated Stark map around the $5s56d\,^1D_2$ state. The nearest dipole coupled states, $5s54f\,^1F_3$ and $5s56p\,^1P_1$, have been highlighted. The energies of these states have been extrapolated once they hit the high angular momentum manifolds. Gaps in the manifolds are solely due to the finite resolution of the simulation (up to $l = 40$).

45893.539±0.013 cm^{-1} for the $5s56p\,^1P_1$ state, and 45894.464±0.013 cm^{-1} for the $5s54f\,^1F_3$ state (using a 200 MHz error bar from the wavemeter absolute measurement accuracy).

The $54\,^1F_3$ and $56\,^1P_1$ states cannot be excited in zero electric field, since the excitation to the Rydberg state is via the $5s5p\,^1P_1$ intermediate state. However, the presence of a small electric field mixes some of the $54\,^1F_3$ and $56\,^1P_1$ state character into the $56\,^1D_2$ state (see fig. 4.6). In this way atoms in the $54\,^1F_3$ and $56\,^1P_1$ states can be detected using autoionization. This has already been illustrated in fig. 4.2, where a stark map was acquired for the $54\,^1F_3$ state using the step-scan technique with autoionization.

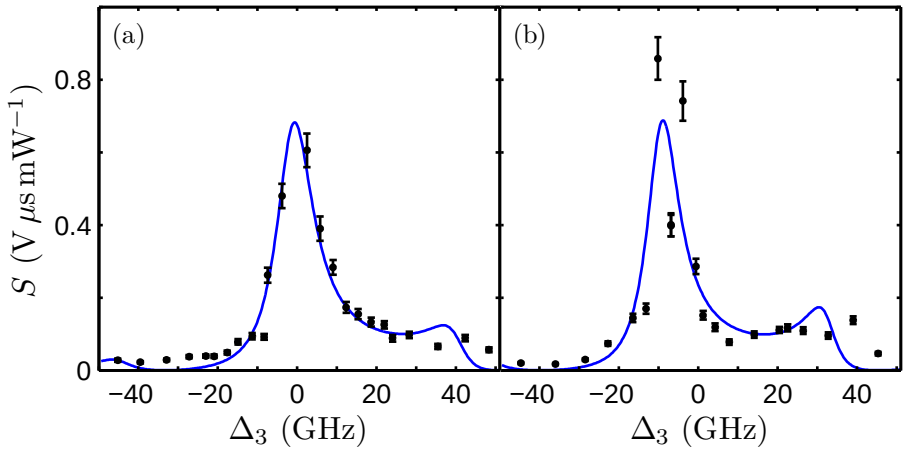

Figure 6.5: Autoionization spectra for the (a) $5s54f\ ^1F_3$ and (b) $5s56p\ ^1P_1$ states, with two-channel MQDT model fits (blue solid lines). $P_2 = 21$ mW, $\Delta t = 0$.

6.2.1 Experiments on the $5s54f\ ^1F_3$ and $5s56p\ ^1P_1$ states

We will now measure the lifetimes and autoionization spectra of the $54\,^1F_3$ or $56\,^1P_1$ states, and see if this sheds any light on the evolution of a Rydberg gas initially excited to the $56\,^1D_2$ state, and if we can identify population transfer to these nearest dipole coupled states.

Autoionization spectra

The autoionization spectra of the $54\,^1F_3$ or $56\,^1P_1$ states are acquired using the step-scan technique with autoionization. In both cases an electric field of 0.1 V cm^{-1} is applied during the Rydberg excitation (but *not* during the autoionization). The autoionization spectra for both states are acquired with $P_2 = 21$ mW and $\Delta t = 0$.

The results are shown in fig. 6.5. The data is fit with simple two-channel (see section 5.1.1) MQDT models (blue solid lines on fig. 6.5). A model with more channels is not used since: the $^1F_3$ autoionizing series has not been studied before in strontium (a study of the $^1P_1$ can be found in [162]), so it is unclear how many channels to use; the various MQDT parameters are unknown, and

a complex multi-variate fit is not accurate without having many members of each series to study; the simple two-channel model will enable a quantitative study later.

The agreement between the two-channel MQDT models and the $54\,^1F_3$ or $56\,^1P_1$ state autoionization spectrum data is reasonable, particularly for the $54\,^1F_3$ state. There may be some evidence of splitting in the $56\,^1P_1$ state data, which could be explained by interference between channels in a full MQDT model.

Lifetime measurements

The decay of the autoionization signal after atoms are excited to the $54\,^1F_3$ or $56\,^1P_1$ state, measured using the step-scan with autoionization technique (fig. 5.8), is shown in fig. 6.6. A static field of $0.2\ \mathrm{V\,cm^{-1}}$ is applied during the Rydberg excitation to perform the decay measurement on the $56\,^1P_1$ state, with $P_2 = 20$ mW and $\Delta_3 = -9.8$ GHz. The $56\,^1P_1$ state data is shown as the black dots on fig. 6.6.

The stray field in our main chamber was sufficient to excite atoms to the $54\,^1F_3$ state for the decay measurement; no additional electric field was applied. The $54\,^1F_3$ state data is shown on fig. 6.6 (blue crosses), and taken with $P_2 = 26$ mW and $\Delta_3 = -2.3$ GHz.

The spontaneous ionization from the $54\,^1F_3$ and $56\,^1P_1$ states is barely visible above noise in these experiments, suggesting that very few Rydberg atoms are created. In chapter 3, the sensitivity of the step-scan technique was shown, and this decay data illustrates how autoionization can be used as an extremely sensitive probe of the Rydberg state population. The decay of the $54\,^1F_3$ and $56\,^1P_1$ state populations are well described by single exponential fits (solid lines on fig. 6.6), yielding state lifetimes of $\tau_{54F} = 64^{+4}_{-5}$ μs and $\tau_{56P} = 85^{+3}_{-4}$ μs.

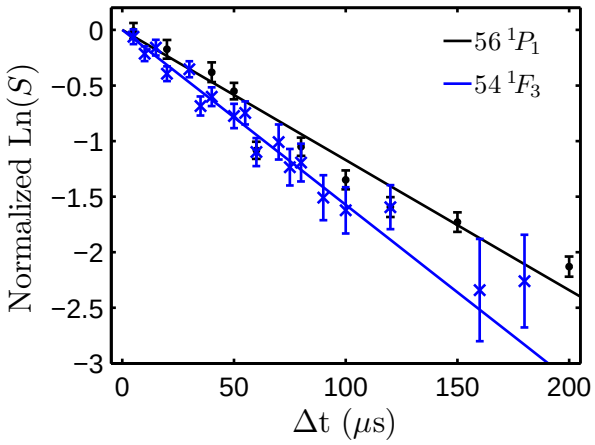

Figure 6.6: Decay of the normalized autoionization signals S for the $54\,^1F_3$ (blue crosses) and $56\,^1P_1$ (black dots) states. The solid lines are exponential decay fits to the data. The $54\,^1F_3$ state data hits the noise floor at $\Delta t \approx 150$ μs.

6.2.2 Comparison to the $5s56d\,^1D_2$ state data

Now that properties of the nearest dipole coupled states to the initially prepared $56\,^1D_2$ state are known, it can be decided whether the $54\,^1F_3$ and $56\,^1P_1$ states are the destination of population transfer in the Rydberg gas.

Figure 6.7 shows a comparison of the $54\,^1F_3$ and $56\,^1P_1$ state autoionization spectra (solid lines) to the autoionization spectrum of the gas initially prepared in the $56\,^1D_2$ state after $\Delta t = 150$ μs (black points, dashed line), at which point all of the $56\,^1D_2$ atoms will have decayed out of this state ($\tau_{56D} \approx 25$ μs). Hence, the Rydberg states that are probed at this time will be the states to which population has been transferred.

It is not immediately clear from fig. 6.7 which modeled autoionization spectrum, $54\,^1F_3$ or $56\,^1P_1$, best agrees with the late-time data. Both of the modeled spectra have roughly the correct width, and reproduce a shoulder to the positive detuning side of the data. The $54\,^1F_3$ state spectrum better coincides with the peak in the late-time data than the $56\,^1P_1$ state spectrum. It should be noted that further narrowing and structure could be reproduced with a MQDT model involving more than two channels.

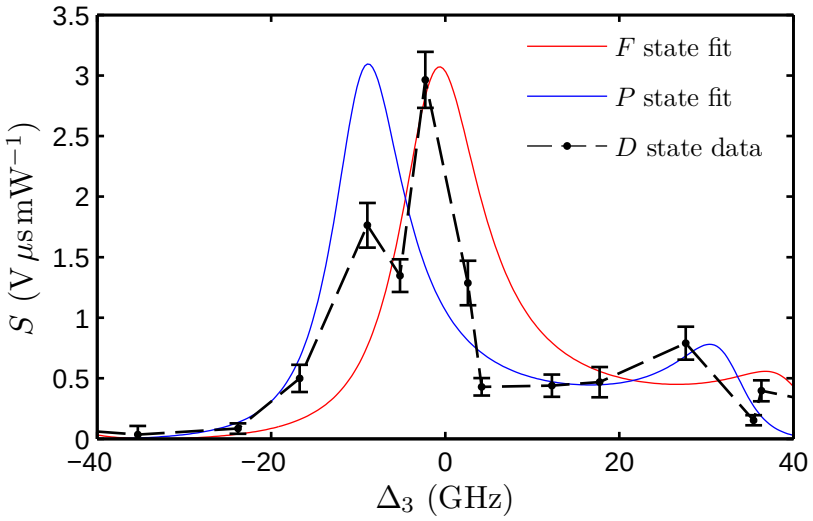

Figure 6.7: The autoionization spectrum of the 56 $^1D_2$ state at Δt = 150 μs (black dots), and the MQDT model fits for the 54 $^1F_3$ (red line) and 56 $^1P_1$ (blue line) states. The MQDT models have been arbitrarily scaled for comparison with the data.

More compelling evidence as to the destination of population transfer is provided by comparing the state lifetimes. Figure 6.8 shows the decay of the 56 $^1P_1$ (black plus signs) and 54 $^1F_3$ (blue crosses) state data, along with the decay of the autoionization signal from the gas initially prepared in the 56 $^1D_2$ state at the position of the long-lived peak (green triangles) and in the wings of the autoionization spectrum (red squares).

This latter decay is attributed to the decay of the 56 $^1D_2$ state alone, and is clearly the fastest decaying signal ($\tau_{56D} \approx 25$ μs). The decay at the spectral position of the long-lived peak in the 56 $^1D_2$ autoionization spectrum has a double exponential decay, as discussed above. The slower component of the decay has $\tau'_{56D} = 60.2 \pm 6.6$ μs, which matches the decay of the 54 $^1F_3$ state $\tau_{54F} = 64^{+4}_{-5}$ μs. The lifetime of the 56 $^1P_1$ state is $\tau_{56P} = 85^{+3}_{-4}$ μs, which is considerable longer than τ'_{56D}. The decay rate of the 56 $^1P_1$ state is not evident at any point on the autoionization spectrum of the Rydberg gas initially prepared in the 56 $^1D_2$ state (see fig. 6.3(a)).

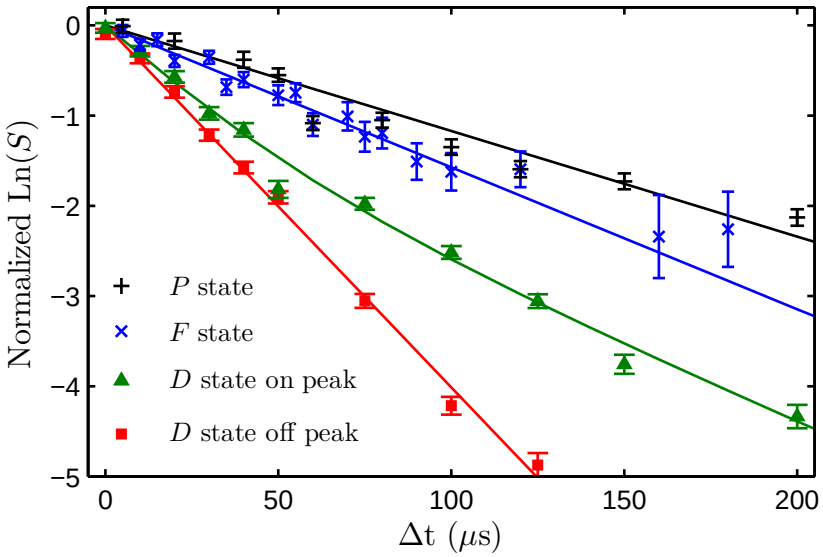

Figure 6.8: The normalized decay of the autoionization signals for the $56\,^1P_1$ state (black plus signs), the $54\,^1F_3$ state (blue crosses), and the $56\,^1D_2$ state in the wings (green triangles) and on the density-dependent peak (red squares) of the autoionization spectrum. The fits (solid lines) are as described in figs. 6.3 and 6.6.

Conclusion

From the data presented in this section we conclude that a gas initially excited to the $5s56d\,^1D_2$ Rydberg state undergoes population transfer, predominatly to the $5s54f\,^1F_3$ state, which is the nearest dipole coupled state of higher angular momentum. There is no evidence of mixing to the $5s56p\,^1P_2$ state, which is the nearest dipole coupled state of lower angular momentum.

There is the potential for transfer to even higher angular momentum states $l > 3$. These states would appear as a longer-lived, narrower features in the autoionization spectrum, close to $\Delta_3 = 0$. This signal was searched for, but not found, though this could be due to the coarse spectral resolution of the autoionization laser. There is certainly evidence of mixing to higher angular momentum states at vary high Rydberg density, as will be discussed in section 6.4.

6.3 Analysis of the autoionization spectra

With the knowledge that population is transferred from the $5s56d\,^1D_2$ state to the $5s54f\,^1F_3$ state a model can be constructed to fully describe the autoionization spectrum. As has been shown, the $56\,^1D_2$ state is well described by a six-channel MQDT model, and the $54\,^1F_4$ state by a two-channel model. The following time dependent total autoionization signal $S_{\mathrm{T}}(\Delta_3, \Delta\mathrm{t})$ is constructed:

$$S_{\mathrm{T}}(\Delta_3, \Delta\mathrm{t}) = A\sigma_D^{(6)}(\Delta_3)\mathrm{e}^{-\Delta\mathrm{t}/\tau_{56D}} + B\sigma_F^{(2)}(\Delta_3)\mathrm{e}^{-\Delta\mathrm{t}/\tau_{54F}}\,, \tag{6.1}$$

where the dependence on the frequency ω_3 of the autoionizing laser is represented by the detuning Δ_3; $\sigma_{D,F}$ are the autoionization cross sections for the $56\,^1D_2$ and $54\,^1F_4$ states respectively, with the superscript denoting the number of channels in the MQDT model; A, B are amplitude scaling parameters; and τ are the measured state lifetimes. The only free parameters are A and B, which are optimized so that S_{T} describes the data for all Δt.

The variation in the autoionization spectrum with the Rydberg atom density (varied with P_2) is shown in fig. 6.9. The combined model S_{T} is indicated by the solid red lines. At $P_2 = 1$ mW, B is set to zero, i.e. there is no $54\,^1F_3$ state component. The agreement is not overwhelming, in particular the narrowness of the density-dependent peak is not reproduced. There are several possible explanations for this lack of agreement. A six-channel MQDT model for the $54\,^1F_3$ state would be narrower, and a two-channel model has been used. The six-channel fit to the $56\,^1D_2$ state data is complex, and includes an unweighted sum over $|J, M_J\rangle$ states (see appendix D), which may not be the correct model. Also, the frequency axis is not particularly fine, and a more tunable autoionizing laser would allow a more accurate analysis of the autoionization spectra.

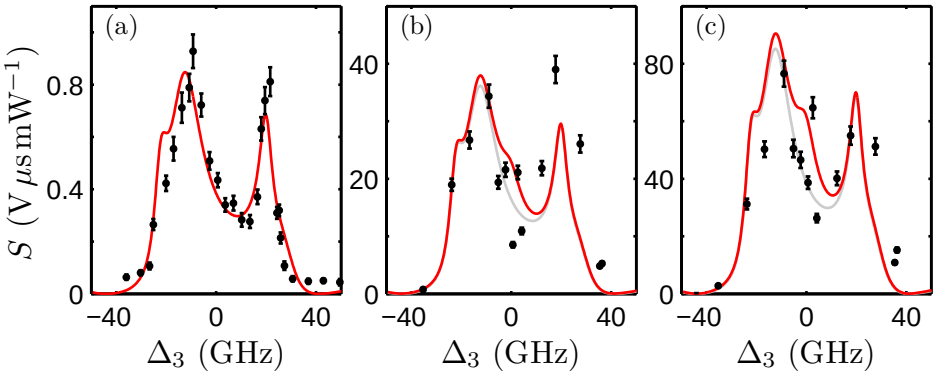

Figure 6.9: The autoionization spectra of a gas initially excited to the 56 $^1D_2$ state for a Rydberg excitation laser power of (a) $P_2 = 1$ mW, (b) $P_2 = 5$ mW and (c) $P_2 = 10$ mW. The solid red lines are the combined 56 $^1D_2$ and 54 $^1F_3$ state MQDT models, and the grey lines are the models for the 56 $^1D_2$ state alone.

However, the combined model S_T reproduces the time evolution of the autoioniziation spectrum remarkably well, as is shown in fig. 6.10. Each component (56 $^1D_2$ and 54 $^1F_3$) is allowed to evolve with its respective state lifetime, as in eqn. (6.1). It is clear from a comparison with the single-state models (marked in grey on fig. 6.10), that the combined model is superior for describing the structure of the spectra.

In future, a comparison of the combined model S_T to the data would undoubtedly be helped by a finer autoionization laser frequency ω_3 resolution, which is poor since, in this experiment, ω_3 could only be varied through gross adjustment of the laser feedback grating, the diode supply current, and the diode temperature.

6.3.1 Quantitative analysis of state mixing

The combined autoionization model can be used to make a quantitative statement about the population transfer in the Rydberg gas. The autoionization signal S_L due to atoms of a particular angular momentum L, at a time Δt, can be expressed as:

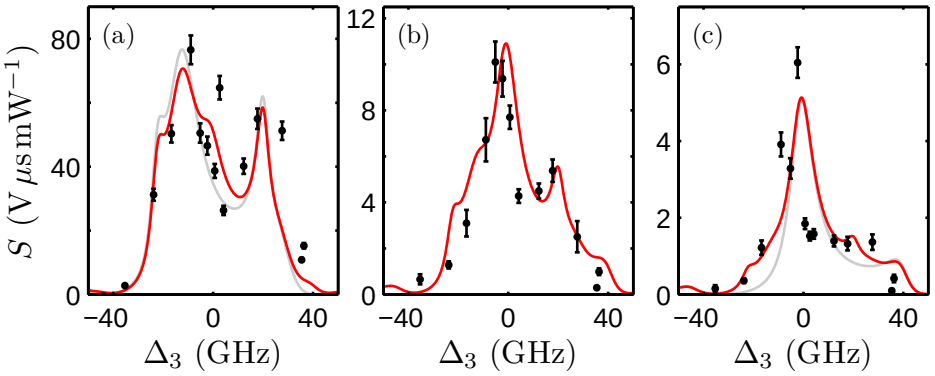

Figure 6.10: The autoionization spectra of a gas initially excited to the $56\,^1D_2$ state acquires at (a) $\Delta t = 0.5$ μs, (b) $\Delta t = 60$ μs and (c) $\Delta t = 100$ μs. The solid red lines are the combined $56\,^1D_2$ and $54\,^1F_3$ state MQDT models. (a) and (c) include the single $56\,^1D_2$ and $54\,^1F_3$ state models respectively, marked in grey. $P_2 = 10$ mW.

$$S_L(\Delta_3, \Delta t) = \eta N_L(\Delta t)\sigma_L(\Delta_3)\,, \tag{6.2}$$

where η is a constant detection efficiency/signal-per-ion factor, $N_L(\Delta t)$ the number of atoms in a state L at a time Δt, and $\sigma_L(\Delta_3)$ the autoionization cross section for an atom in a state L. It should be noted that, through our choice of normalization, S_L is adjusted for the power P_3 of the autoionizing laser λ_3, otherwise the photon flux due to this laser would have to be included in the above expression. Equation 6.2 is used to express the ratio of the number of atoms in each L state, to remove the unknown factor η:

$$\frac{N_F(\Delta t)}{N_D(\Delta t)} = \frac{S_F(\Delta_3, \Delta t)}{S_D(\Delta_3, \Delta t)}\frac{\sigma_D(\Delta_3)}{\sigma_F(\Delta_3)}\,, \tag{6.3}$$

which must be evaluated at a certain Δ_3, which is taken to be the point at which the signal due to the $54\,^1F_3$ state atoms is the greatest: $\Delta_3 = -0.54$ GHz $\equiv \Delta_3^F$. The transfer at $\Delta t = 0$ will be calculated, so the exponential decay terms from eqn. (6.1) do not appear.

To find the autoionization signal S_L due to the atoms in each state, the total signal S_T from eqn. 6.1 is split into the contribution from each state. From the autoionization spectra taken with $P_2 = 10$ mW this yields $S_D(\Delta_3^F) = (33 \pm 5)\ \mathrm{V}\,\mu\mathrm{s}\,\mathrm{mW}^{-1}$, and $S_F(\Delta_3^F) = (20 \pm 3)\ \mathrm{V}\,\mu\mathrm{s}\,\mathrm{mW}^{-1}$[3].

To directly compare the autoionization cross sections σ_L the MQDT models describing them must be directly comparable. This requires that each model uses the same number of channels. Since we cannot construct a six-channel model for the $^1F_3$ states, a two-channel model $\sigma_D^{(2)}$ must be used to describe the $56\,^1D_2$ state. The two-channel $56\,^1D_2$ MQDT model $\sigma_D^{(2)}$ is shown in fig. 5.6(a). Although $\sigma_D^{(2)}$ does not accurately reproduce the structure of the autoionization spectrum, it does accurately reproduce the width. The two-channel MQDT models yield $\sigma_D^{(2)}(\Delta_3^F)/\sigma_F^{(2)}(\Delta_3^F) = 0.30 \pm 0.03$. The error bars come directly from the fit.

To clarify, the combined MQDT model S_T is used to evaluate the level of autoionization signal due to each state, since S_T best predicts the absolute size of the autoionization signal. Two-channel MQDT models are used to evaluate the autoionization cross section for each state, since these models are directly comparable.

Through this analysis we calculate $N_F/N_D = 0.15 \pm 0.03$ at $\Delta\mathrm{t} = 0$. If one presumes that all of the autoionization signal is due to either the $56\,^1D_2$ or $54\,^1F_3$ state[4] then it can be stated that $18 \pm 3\%$ of the Rydberg gas is transferred to the $54\,^1F_3$ state after a 4 μs long excitation to the $56\,^1D_2$ state, with a Rydberg excitation laser power of $P_2 = 10$ mW, which is estimated to correspond to a Rydberg atom density of $\sim 5 \times 10^9$ cm^{-3}. A similar analysis

[3] The error bars are evaluated by comparing $A\sigma_D^{(6)}(\Delta_3)e^{-\Delta\mathrm{t}/\tau_{56D}}$ to the autoionization data at $\Delta\mathrm{t} = 0$, where the $56\,^1D_2$ state dominates the shape of the autoionizing spectrum, and by comparing $B\sigma_F^{(2)}(\Delta_3)e^{-\Delta\mathrm{t}/\tau_{54F}}$ to the autoionization data at $\Delta\mathrm{t} = 150$ μs, where the $54\,^1F_3$ state dominates.

[4] i.e. $N_T/(N_F + N_D) = 1$, where N_T is the total number of Rydberg atoms in the gas.

of our work [11], using a "by eye" minimization, concluded that 13 ± 3 of the total Rydberg gas population was transferred to the $54\,^1F_3$ state, which gives an indication as to the level of accuracy of this analysis.

It should be noted that all of these autoionization spectra were acquired using a diode laser λ_3 that was not frequency stabilized, and that the frequency of this laser was varied through coarse adjustments of the diode feedback grating, the supply current, and the diode temperature. The data acquisition sequence was very time consuming, as the Rydberg excitation laser λ_2 was also not frequency stabilized, and was stepped over the Rydberg state resonance for each data point on the autoionization spectra (the step-scan technique). If λ_2 and λ_3 were frequency stabilized we are confident that the accuracy of this quantification of population transfer could be greatly improved.

6.4 State Mixing processes

We have shown that there is population transfer between Rydberg states in a cold gas of strontium, but have not attempted to identify the mechanism that causes the transfer. In this section various state mixing phenomena will be considered, and observations from the experiment will allow an identification of the dominant transfer mechanism.

Figure. 6.9 shows that whatever the population transfer mechanism is, it is density-dependent. In fig. 6.11 the autoionization laser is tuned to a point in the wings of the autoionization spectrum, as indicated on fig. 6.11(a). At this spectral point the autoionization signal is predominantly from atoms in the $56\,^1D_2$ state. The power P_2 of the Rydberg excitation laser (and hence the Rydberg density) is varied, and the autoionization signal at $\Delta t = 0.5\ \mu s$ monitored. The results are shown in fig. 6.11(b). There is perhaps some non-linear behaviour at very low Rydberg densities, but otherwise the increase in

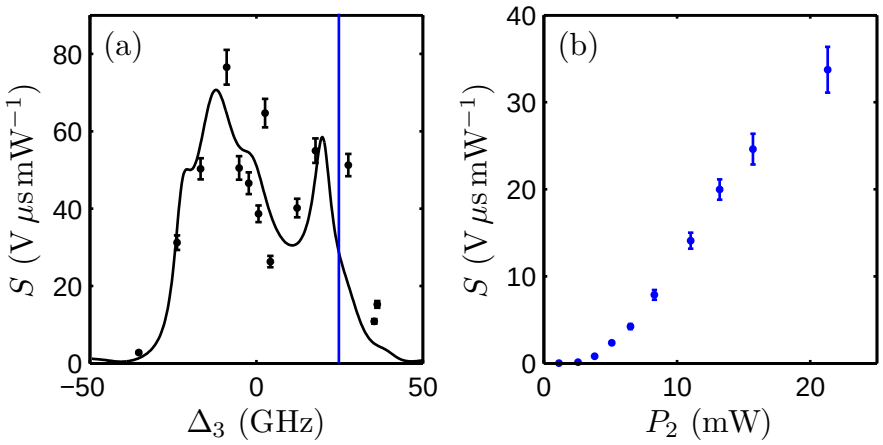

Figure 6.11: (a) Autoionization spectrum of the $56\,^1D_2$ state, with $P_2 = 10$ mW and $\Delta t = 0.5$ μs. (b) Variation in the autoionization signal with P_2, taken at the point marked in (a), at Δt = 0.5 μs.

autoionization signal is linear.

In fig. 6.12 the autoionization laser is tuned to the long-lived peak in the autoionization spectrum, as indicated on fig. 6.12(a). The power P_2 is varied, and the autoionization signal at Δt = 100 μs monitored. At this spectral point and delay time the signal is dominated by atoms in the $54\,^1F_3$ state. In this case the dependence of the autoionization signal upon the Rydberg atom density (varied with P_2) is drastically different from the signal due to the $56\,^1D_2$ state, as shown in fig. 6.12(b). At low Rydberg densities the signal increases linearly; possibly due to the residual signal from the $56\,^1D_2$ state atoms. At $P_2 \approx 12$ mW there is a clear threshold in the signal, and the signal due to the $54\,^1F_3$ state begins to increase more rapidly.

With the information we have gathered so far as to the nature of the population transfer mechanisms, we will now consider different state mixing processes.

These graphs show that the signal due to the $56\,^1D_2$ and $54\,^1F_3$ state atoms do not behave in the same way as the Rydberg density is varied, and that transfer to the $54\,^1F_3$ state is clearly density-dependent.

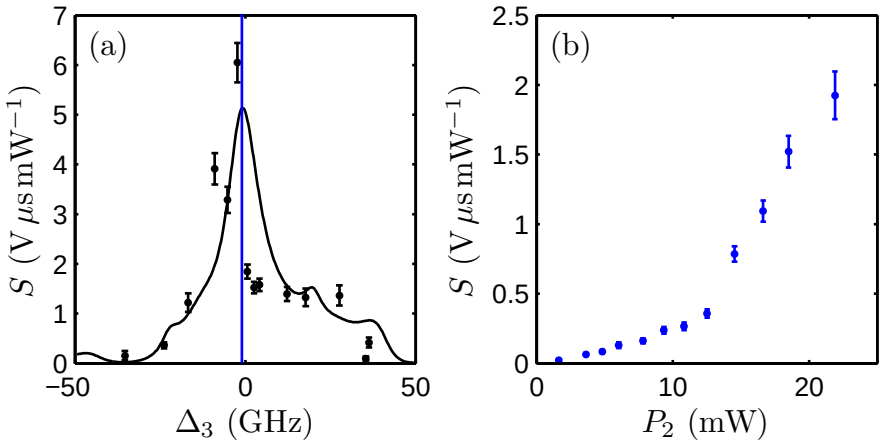

Figure 6.12: (a) Autoionization spectrum of the 56 $^1D_2$ state, with $P_2 = 10$ mW and $\Delta t = 100$ μs. (b) Variation in the autoionization signal with P_2, taken at the point marked in (a), at Δt = 100 μs.

Black-body radiation

Although Rydberg states themselves cannot be populated from the ground state by blackbody radiation (BBR) at room temperature, the energy spacings between Rydberg states are often less than k_BT at 300 K, and the dipole matrix-elements for transitions between Rydberg states are large [26]. Hence, BBR can transfer population between Rydberg states, preferentially to the states closest in energy [104] with the value of l allowed to vary by ± 1.

The total depopulation of a Rydberg state due to BBR was discussed in section 3.1. The equation in that section gives the total depopulation rate at $n = 56$ as ~ 6 kHz, which sets an absolute upper limit of the population transfer rate due to BBR. It is evident from fig. 6.9 that population transfer has occurred by the end of the 4 μs Rydberg excitation, since the 54 $^1F_3$ state peak has appeared in the autoionization spectrum by this point. Hence, blackbody induced population transfer is far too slow to explain this data. BBR would populate the 56 $^1P_1$ state, which is not observed. Also, the population transfer is Rydberg atom density-dependent, which one would not expect if BBR was the cause.

Blackbody radiation may cause mixing into very high angular momentum states, over a longer timescale. We rule out BBR as a driver of population transfer in our experiment, though it should be noted that BBR has a dramatic effect upon the spontaneous decay rate of Rydberg states at high n [1, 26].

Super-radiant population transfer

Super-radiant decay is a coherent emission phenomenon [163], which occurs if the gas that is emitting has a size comparable to the wavelength of the emitted radiation. This is true for transitions between Rydberg states, and one finds that the rate of transfer between these states is enhanced by a factor of N^2, where N is the number of Rydberg atoms in the gas [125]. By comparison with [125], the total super-radiant decay rate would be ~ 1 MHz. This is rapid enough to explain population transfer in our experiment.

However, a couple of features of super-radiant decay rule it out. Firstly, the presence of super-radient decay *increases* the decay rate out a Rydberg state [164], and we do not observe any decrease in state lifetime with Rydberg density in our experiment. Also, vitally, super-radient decay is to states of *lower* energy than the initial state [125], and the $54\,^1F_3$ state is higher in energy than the $56\,^1D_2$ state.

Three-body recombination

Three-body recombination in ultra-cold plasmas leads to the formation of Rydberg atoms [55]. If there are free ions and electrons in our Rydberg gas, which there certainly are, then population could be transferred into Rydberg states other than the initially excited one by three-body recombination. However, as shown in [55], three-body recombination would populate a range of n states, which we do not observe.

Stark mixing

An electric field causes state mixing, as discussed in section 4.2.2. This mechanism has been used to prepare atoms in states of high angular momentum l [148], by laser exciting to a state of high l in an electric field, and then adiabatically ramping the field to zero [146].

The stray static field in our experiment is small ($< 10\,\mathrm{mV\,cm^{-1}}$), far too small to cause any significant state mixing (see fig. 4.6). However, there is rapid spontaneous ionization of our Rydberg gas, which creates static ions (the ions remain cold since the atoms were cold). If we consider the highest Rydberg density observed in this experiment, $\sim 5 \times 10^9$ cm^{-3}, this corresponds to an average nearest neighbour spacing of ~ 3 μm. The field due to an ion at this distance would be $\sim 20\,\mathrm{mV\,cm^{-1}}$. According to the character map in fig. 4.6 this would mix in less than 1% of any other angular momentum state.

This estimate of mixing into the $54\,^1F_3$ state is far too low to explain our observations. It would also require population of the $56\,^1P_1$ state, which we do not observe. It becomes even more insignificant when it is considered that only a few Rydberg atoms would be exposed to this field. By comparing the spontaneous ionization and autoionization signals at $\Delta t = 0$ we estimate that only 1% of the Rydberg gas spontaneously ionizes. Hence, the electric field due to spontaneously created ions cannot be a major contributor to population transfer in our experiment.

Dipole-dipole interactions

Population transfer in cold Rydberg gases due to the dipole-dipole interaction has been observed and studied in several experiments [40, 160, 165]. This state mixing process is interesting, since it is not collision-mediated, and is a collective phenomena; it cannot be described as an interaction between individual atoms [160]. This behaviour is more akin to interactions in

an amorphous solid than the usual collisional processes in a gas [165]. The amount of state mixing depends strongly upon the size and sign of the interaction between the initially excited atoms, and becomes strongly enhanced near Förster resonances [121]. Our system is not near the resonant case, since the most strongly coupled pair state is -2.5 GHz separated in energy.

The work presented in chapter 4 can be used to calculate the level of state mixing due to dipole-dipole interactions. By considering the case where there is a single dominant pair state interacting with the initial pair state, with a Hamiltonian given by eqn. (4.14), the eigenstates of the dipole-dipole interaction between two atoms in a $n\,^1D_2$ state are [140]:

$$\begin{aligned} \psi_- &= \cos\theta|n\,^1D_2, n\,^1D_2\rangle - \sin\theta|n\,^1P_1, (n-2)\,^1F_3\rangle \\ \psi_+ &= \sin\theta|n\,^1D_2, n\,^1D_2\rangle + \cos\theta|n\,^1P_1, (n-2)\,^1F_3\rangle\,, \end{aligned} \tag{6.4}$$

where $\tan 2\theta = -2\sqrt{\frac{D_\phi C_6}{\delta_{st}}}R^{-3}$, where R is the separation between the atoms in the initial pair. Considering the most strongly interacting pair of initial m_j states, this would cause a mixing of 5% at $R = 3$ μm. This means that the dipole-dipole interaction will mix 5% $54\,^1F_3$ and $56\,^1P_1$ state character into the initial $56\,^1D_2$ state pair.

This mixing is too small to explain our data on its own. It certainly is density-dependent, though does not explain the presence of a threshold in the mixing, as seen in fig. 6.12. Also, this interaction would mix $56\,^1P_1$ state character into the $56\,^1D_2$ state, which we do not observe. Hence dipole-dipole interactions cannot be the sole driver of population transfer in our experiment.

6.4.1 Cold plasma formation

Early evidence of angular momentum state l mixing in a cold Rydberg gas was provided in [159]. In that experiment, a discreet Rydberg state was

excited at high Rydberg atom density (10^{8-9} cm^{-3} for Rydberg states of $n = 80 - 20$ respectively) in a cold gas of Rubidium. They observed spontaneous electron emission over timescales of $\sim$ 20 ms, whereas the initial state lifetime was only of the order $\sim$ 100 μs. This long-timescale electron emission was attributed to l state mixing, since higher l states have longer lifetimes, and the state mixing process was attributed to electron-Rydberg atom collisions. However, to explain the observed level of state mixing it was found to be essential that the number of collisions between electrons and Rydberg atoms was enhanced through the formation of an ultra-cold plasma, where the electrons oscillate back and forth through the gas, undergoing many collisions with Rydberg atoms.

Below we present evidence for the formation of a cold plasma in our experiment.

Evidence for the formation of a cold plasma

We have performed a similar experiment to the one discussed above. Atoms are prepared in the $5s56d\,^1D_2$ state using the step-scan technique, with $P_2 =$ 15 mW, and a ground state density of $(3.7 \pm 0.4) \times 10^{10}$ cm^{-3}. Under these conditions we can estimate a Rydberg atom density of at most $\sim 6{\times}10^9$ cm^{-3}, estimating that $\sim$ 12% of the ground state atoms are excited to the Rydberg state (see section 3.3). In this experiment, there is a delay $\Delta\tilde{t}$ between the end of the Rydberg excitation pulse and the electric field pulse, which directs the spontaneous ionization to the MCP detector. Autoionization is *not* used in this experiment.

The results are shown in fig. 6.13. We observe ionization up to 20 ms after the Rydberg excitation, at which point we are limited by our experimental set-up. Even at these long times the spontaneous ionization is clearly visible above the noise floor, as shown in the sub-plot on fig. 6.13(a). Figure. 6.13(b) provides evidence for the state-mixing mechanism. The spontaneous ioniza-

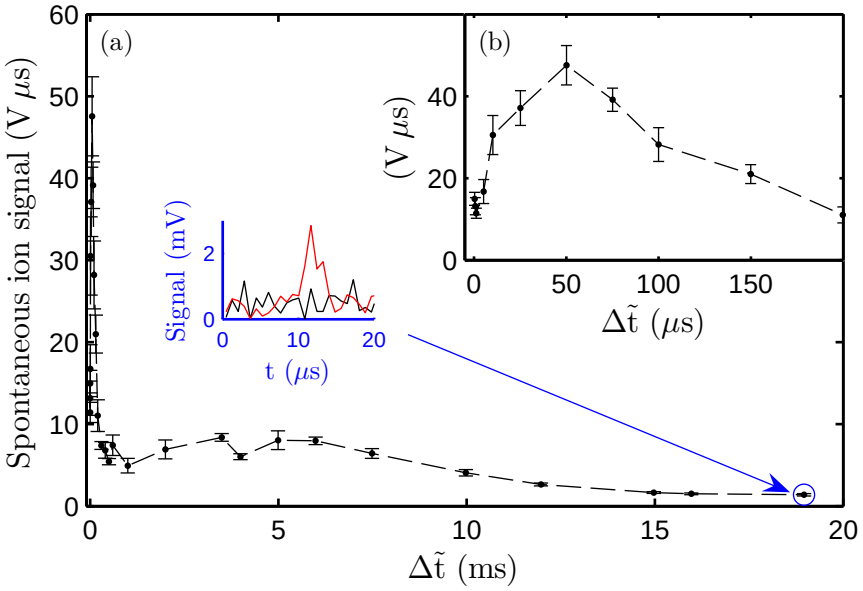

Figure 6.13: (a) Variation in spontaneous ionization signal from a gas of 56 $^1D_2$ state atoms with the delay $\Delta\tilde{t}$ between the end of the Rydberg excitation and the electric field pulse. Ionization is visible for almost 20 ms. The time-resolved ion signal for the last data point is shown; the resonant spontaneous ion signal (red) is clearly visible above the background noise (black). (b) The spontaneous ionization in the first 200 μs. We attribute the hump at ~ 50 μs to the formation of a cold plasma.

tion signal rises at $\Delta\tilde{t} \approx 50$ μs, and then falls away again. We attribute this to the formation of a cold plasma, as will be discussed is more detail below (c.f. fig. 3 in [105]).

As discussed in section 1.3, Rydberg gases can spontaneously evolve into ultra-cold neutral plasmas [56]. When measuring the emission of ions from the Rydberg gas, when a plasma is formed, a marked density-dependent increase in spontaneous ionization is observed [56].

Figure 6.14 shows the time evolution of the total ionization (spontaneous and autoionization, black dots), and spontaneous ionization (red crosses) from the Rydberg gas, for different initial Rydberg atom densities. Figure 6.14(a) is at an estimated Rydberg atom density of 3×10^9 cm^{-3}. There is a low hump of

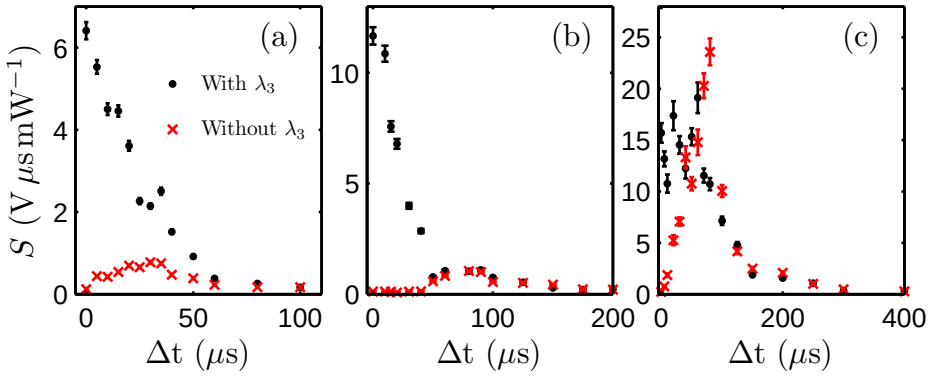

Figure 6.14: The variation in the autoionization (black dots) and spontaneous ionization signals (red crosses) with the delay Δt after the Rydberg excitation, for (a) $P_2 = 5$ mW, (b) $P_2 = 10$ mW and (c) $P_2 = 20$ mW. $\Delta_3 = -1.44$ GHz.

spontaneous ionization signal. This can be explained if it is presumed that a plasma is formed. There is an initial spontaneous ionization mechanism, after which ions remain in the gas (since the atoms are cold) and electrons leave. If this level of ionization is high enough to bind further escaping electrons, then a plasma forms. The electrons oscillate back and forth through the plasma, causing ionization and state mixing. Initially, the binding energy of the plasma is high enough that we do not extract ions by applying a field pulse, hence the initial low spontaneous ionization signal. As the plasma expands it becomes more weakly bound, hence the level of spontaneous ionization signal increases as ions are extracted with the field pulse. Eventually the plasma fully dissipates, and there are no ions to extract. The timescales we observe for these ion signals are comparable to [55]. Still, in this low density case, the autoionization signal is dominant, which means that most of the Rydberg atoms are not ionized by the formation of a plasma.

Figure 6.14(b) shows the ionization from a gas with an initial Rydberg density of approximately 5×10^9 cm^{-3}. The features are very similar as for the lower density case in fig. 6.14(a). At higher initial Rydberg densities one would expect a greater amount of initial ionization, and so a more strongly bound plasma, hence ions cannot be extracted from the plasma until later

than in fig. 6.14(a). In the higher Rydberg density case in fig. 6.14(b), the autoionization signal no longer dominates after ~ 50 μs, and all of the ionization is due to electron-Rydberg atom collisions in the plasma.

The situation is more dramatic in fig. 6.14(c), where the Rydberg atoms are initially excited at a high density of 7×10^9 cm^{-3}. There is a lot of scatter in the data, since at this density the level of spontaneous ionization is very sensitive to fluctuations in the Rydberg density. Here we see avalanche ionization after ~ 40 μs, as the oscillating electrons ionize the vast majority of the Rydberg atoms [58], and no more can be ionized through autoionization. Note that the spontaneous ionization signal persists for much longer than at lower Rydberg densities, suggesting mixing into higher angular momentum states, as shown in fig. 6.13.

The formation of a cold plasma from a Rydberg gas requires a certain initial level of ionization; there must be enough ions present to bind the electrons. This leads to a *threshold* in the plasma ionization signal as the Rydberg density is increased [49, 56]. In fig. 6.15 the variation in spontaneous ionization with initial Rydberg density is shown (red crosses). The abscissa in this figure is the signal S_D in the wings of the autoionization spectrum at Δt $= 0.5$ μs, which is the signal due to the autoionization of $56\,^1D_2$ state atoms, and therefore proportional to the initial number of atoms in that state. Hence, the red crosses on fig. 6.15 show the variation in spontaneous ionization signal S_{BG} with initial the Rydberg state population. There is a clear threshold in this data, as would be expected due to the formation of a plasma. Once there is enough initial spontaneous ionization (i.e. a large enough initial Rydberg state population $\propto S_D$), a plasma will form causing avalanche ionization, and drastically enhancing the spontaneous ionization signal.

Does the position of the plasma formation threshold that we observe make sense? The number of initial ions required to form a plasma can be estimated

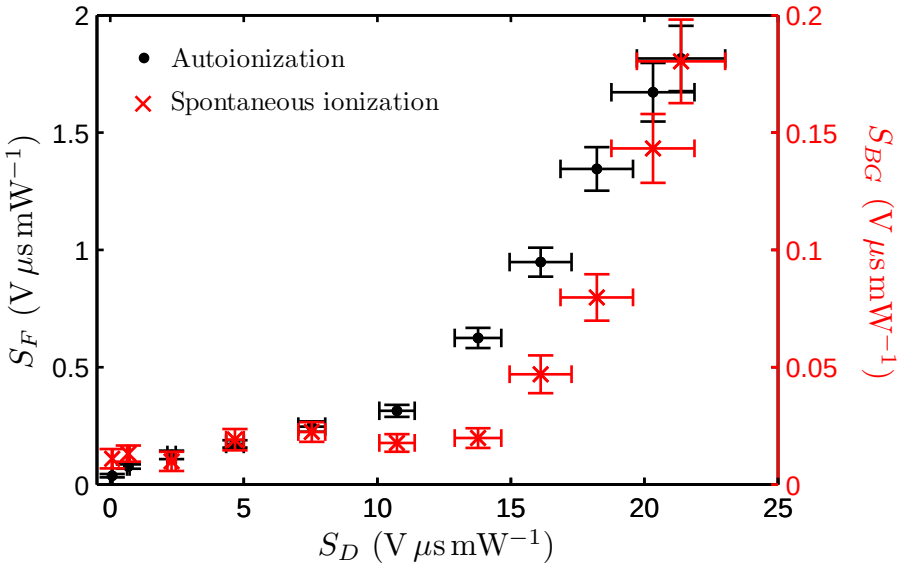

Figure 6.15: The black dots show the variation in the $54\,^1F_3$ state autoionization signal S_F with the $56\,^1D_2$ state autoionization signal S_D. The red crosses show the variation in the background spontaneous ionization signal S_{BG} with S_D. There is a clear threshold in each set of data, and the thresholds coincide.

by considering the maximum binding energy U_i due to a Gaussian cloud of N_i ions [49]:

$$U_i = \sqrt{\frac{2}{\pi}}\frac{N_i e^2}{4\pi\epsilon_0 r}\,, \tag{6.5}$$

where r is the radius of the atomic cloud. The potential U_i must be large enough to bind the electrons, which will have an energy at least equal to the binding energy of the initial Rydberg state. The binding energy of the $5s56\,^1D_2$ state is 1.144 THz (U_i must be at least equal to this value), and the cloud radius is ~ 300 μm. Substituting these values into the above expression requires the minimum number of initially created ions to be ~ 1200. At Δt $= 0$ the level of spontaneous ionization is $\sim 1\%$ of the autoionization signal, which means, as an absolute minimum, the number of initially excited Rydberg atoms must be $\sim 1.2 \times 10^5$, which is $\sim 10\%$ of the typical

ground state population. According to fig. 5.12 this fraction is created with a Rydberg excitation laser power of $P_2 \approx 12$ mW, and from fig. 6.11 this power produces an ion signal of $\sim 15\ \mathrm{V}\,\mu\mathrm{s}\,\mathrm{mW}^{-1}$. This coincides with the threshold in the spontaneous ionization signal seen in fig. 6.15.

There is clear evidence in this experiment of highly density-dependent cold plasma formation, where the binding of electrons by ions created during the initial spontaneous ionization of a Rydberg gas causes avalanche ionization.

State mixing through the formation of a cold plasma

Does the formation of a cold plasma explain state mixing in our Rydberg gas? The black dots on fig. 6.15 show the variation in the autoionization signal due to the $54\,^1F_3$ state atoms, $S_F \propto N_F$ with the autoionization signal due to the $56\,^1D_2$ state, $S_D \propto N_D$. There is a clear threshold in this data as well, and the threshold *coincides* with the threshold in the spontaneous ionization signal. There is little population in the $54\,^1F_3$ state, and hence little state mixing, until the population of the $56\,^1D_2$ state is large enough to enable a cold plasma to form.

To summarize, we observe population transfer to the $54\,^1F_3$ state from the $56\,^1D_2$ state, and the transfer is dependent upon the formation of a cold plasma. State mixing due to this process has been seen in [58], and attributed to collisions between electrons and Rydberg atoms. It was found to be essential that the electrons were bound by plasma formation, otherwise there were too few collisions to cause appreciable state-mixing. However this study observed mixing into a wide range of n and l states.

We have probed Rydberg gas dynamics at the very threshold of plasma formation, where mixing is only into the nearest dipole coupled state of higher angular momentum. This is a fundamentally different regime to that presented in [58], where there are very high levels of ionization and state mixing into many different states. We have also observed this regime of

large amounts of state mixing at higher Rydberg atom density, as shown in fig. 6.13.

Conclusion

We have shown that autoionization is a high yield, state selective probe, which is extremely sensitive to changes in the angular momentum of the Rydberg atom. Through an analysis of the autoionization spectrum of an interacting Rydberg gas we have been able to identify and quantitatively measure population transfer. We have also been able to identify the state mixing mechanism, in this case electron-Rydberg collisions enhanced by the formation of a cold plasma. We have probed the very onset of plasma formation, where population is transfered to the nearest dipole-coupled state of higher angular momentum.

This is a method of studying an interacting Rydberg gas that is unique to an alkaline earth metal like strontium. We probe interactions, which are mediated by the outer valence Rydberg electron, with the inner valence electron. With more stable lasers, and greater tunability, it will be possible to acquire autoionization spectra with much greater accuracy, and look for much narrower autoionization features than we are currently able to. By focusing the autoionization laser we can study state mixing with *spatial* resolution, and understand where in the Rydberg gas the cold plasma forms, and if there are regions of the gas that do not undergo state mixing.

Chapter 7

Discussion

We have designed and built an experiment to study Rydberg states in a cold gas of strontium, and can create a magneto-optical trap (MOT) containing $> 10^6$ atoms at a temperature of ~ 6 mK. This has involved developing equipment and techniques unique to working with an alkaline earth metal. We have developed a strontium dispenser cell [74], which is a simple, cheap and compact apparatus for performing spectroscopy of a thermal gas of strontium. This design is useful for any future experiments using strontium. We have performed polarization spectroscopy in the dispenser cell [87], and use the resultant signal to stabilize the frequency of our cooling laser. This method of polarization spectroscopy is different to the equivalent process in the alkali metals. In the future, the experiment will use the dispenser cell to perform spectroscopy of the Rydberg states of strontium, which will enable frequency stabilization of Rydberg excitation lasers. The experimental apparatus as a whole is robust and flexible; it will be possible to implement a second stage of cooling, and even to mount lenses inside the main chamber to create an optical lattice, or to create focused beams with a waist of less than 1 μm.

We have studied a wide range of Rydberg states excited from the cold gas of strontium. Many Rydberg states that have not been previously identified have been located. A unique method of Rydberg state spectroscopy has been

developed: the "step-scan" technique [12], where the spontaneous ionization of the Rydberg atoms is used as the spectroscopic signal. The high relative accuracy and sensitivity of the step-scan method enables us to detect minimally populated Rydberg states belonging to many different series. Experimentally, this is a simple method to implement, and does not require the ability to produce large electric fields, as in the commonly used technique of field ionization. The step-scan technique can also be used to measure loss from the MOT, from which the population of each Rydberg state can be estimated.

A single-electron model, where the Rydberg states of strontium are modeled as a single electron moving in the potential of the ion core, has been used to calculate dipole transition matrix-elements. The matrix-elements have been tested by simulating Stark maps with the single-electron model, and comparing them to data measured with the step-scan technique [12]. We find a good level of agreement between experiment and theory, and so are confident that the dipole matrix-elements are correct. They can be used to calculate interaction strengths between strontium Rydberg atoms. We find that $^1S_0$ states in strontium exhibit isotropic attractive interactions [1], and that $^1D_2$ states exhibit anisotropic repulsive interactions.

The inner valence electron of a strontium Rydberg atom can be excited, through a process known as isolated core excitation (ICE). We use ICE to create autoionizing states, where the excitation of the inner valence electron causes the atom to rapidly ionize. We have studied and understood the spectra of the autoionizing states of strontium [12], and modeled them with multi-channel quantum defect theory (MQDT). In our experiment autoionization is used as a sensitive probe of the Rydberg state. We find that the Rydberg state population can be studied with high signal-to-noise and high time-resolution, revealing the evolution dynamics of the Rydberg state [12]. This is the first study of autoionizing states in a cold gas, and instantly

highlights an advantage of using an alkaline earth metal, as opposed to an alkali metal with a single valence electron.

We have used autoionization to investigate interactions in our cold strontium Rydberg gas [11]. State mixing in the gas is clearly discernible in the spectra of the autoionizing states. An analysis of these spectra, and the utilization of MQDT models, enables us to identify which states have been populated, quantify the amount of state mixing, and identify the dominant state mixing process. We see clear evidence for the formation of an ultra-cold plasma in our Rydberg gas, which drives the transfer of population between different angular momentum states. This is the first study of state mixing at the onset of plasma formation, where population is transferred to the nearest state of higher angular momentum. We could use strontium ion transition to probe the spatial distribution of the plasma as it forms.

To summarize, we have built the first experiment to create a cold Rydberg gas of strontium, and have shown that the inner valence electron of the Rydberg atom can be exploited to study the Rydberg gas in a unique way. Autoionization can be used as a state selective probe of Rydberg states, with temporal- and spatial-resolution. These facts mean that future experiments can use autoionization to study the dipole blockade at the level of a single blockade sphere, or spatially probe crystallization effects in ultra-cold plasmas.

The divalent nature of strontium means that ground and Rydberg state atoms could be simultaneously trapped in an optical lattice [1]. This will enable future experiments to study many-body crystalline states, using the repulsive $^3S_0$ series, or many-body entangled GHZ states, using the attractive $^1S_0$ states.

The ability to manipulate and probe Rydberg states using the inner valence electrons of divalent atoms has already produced theoretical interest, and there are several groups setting up alkaline earth metal Rydberg gas experiments. We have performed the first study of a cold two-electron Rydberg

gas, and shown that such a system can contribute to the field of Rydberg physics.

Part III

Appendices

Appendix A

Important numbers

Atomic number	38
Ground state configuration	$1s^2 2s^2 2p^6 3s^2 3p^6 3d^{10} 4s^2 4p^6 5s^2\ {}^1S_0$
First excited state energy $5s5p\ {}^1P_1$	21698.452 cm^{-1} [156]
R_{Sr}	109736.627 cm^{-1} [111]
Ionization limit $5s_{1/2}$	45932.1982 cm^{-1} [111]
Ionization limit $5p_{1/2}$	69647.38 cm^{-1} [150]
Ionization limit $5p_{3/2}$	70448.84 cm^{-1} [150]
Sr^+ $5s_{1/2} \rightarrow 5p_{1/2}$ transition	23715 cm^{-1} [149]
Sr^+ $5s_{1/2} \rightarrow 5p_{3/2}$ transition	24517 cm^{-1} [149]

Table A.1: Properties of ^{88}Sr.

Energy	21698.452 cm^{-1} [156] 460.73 nm (air) [166] 650.69 THz (air)
Decay rate	$2\pi \times 32.0$ MHz [166]
State lifetime	5.0 ns
Saturation intensity	43 $mW\,cm^{-1}$
Doppler cooling limit	0.77 mK

Table A.2: Properties of the principal transition of ^{88}Sr, $5s^2 \rightarrow 5s5p\,^1P_1$.

Isotope	**Abundance (%)**	I	F	**Shift (MHz)**	**Relative strength**
^{84}Sr	0.56	0	-	-270.8	1
^{86}Sr	9.86	0	-	-124.5	1
			7/2	-9.7	4/15
^{87}Sr	7.00	9/2	9/2	-68.9	1/3
			11/2	-51.9	2/5
^{88}Sr	82.58	0	-	0	1

Table A.3: Properties of the naturally occurring isotopes of strontium. The isotope shifts and hyperfine splittings are for the $5s^2\,^1S_0 \rightarrow 5s5p\,^3P_1$ transition, relative to ^{88}Sr, and taken from [167, 168].

	a	b	c		A	B
$^1S_0$	3.762	-6.33	1.07		3.27	-0.22
$^1P_1$	3.49	-1.86	1.10		2.72	-3.23
$^1D_2$	2.78	-9.06	2.31		2.37	-10.00
$^1F_3$	9.22	-6.35	1.00		0.08	-0.96
$^3S_1$	2.93	-5.28	1.22		3.36	0.68
$^3P_0$	3.45	-6.02	-6.13		2.89	-0.17
$^3P_1$	3.35	-6.13	1.12		2.90	-0.43
$^3P_2$	3.23	-6.20	1.19		2.89	-1.00
$^3D_1$	3.41	-6.02	1.27		2.66	-10.00
$^3D_2$	3.12	-4.52	1.24		2.66	-10.00
$^3D_3$	2.86	-9.71	2.20		2.66	-10.00
$^3F_{2,3,4}$	1.18	-9.04	1.06		0.11	-0.34

Table A.4: Fitting parameters a, b, c for the model potential, and A, B for the quantum defect extrapolation, used in the single electron model.

Appendix B

Circuit diagrams

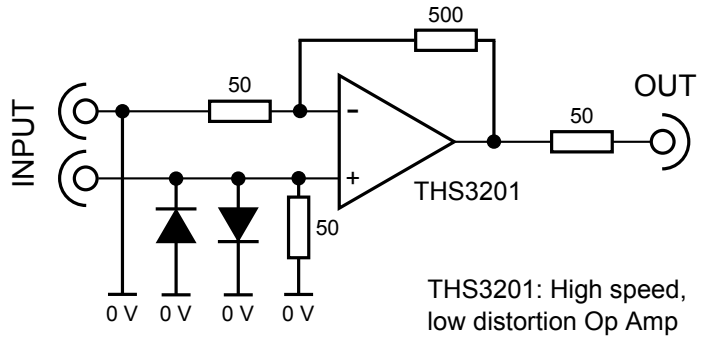

Figure B.1: MCP pre-amplifier circuit.

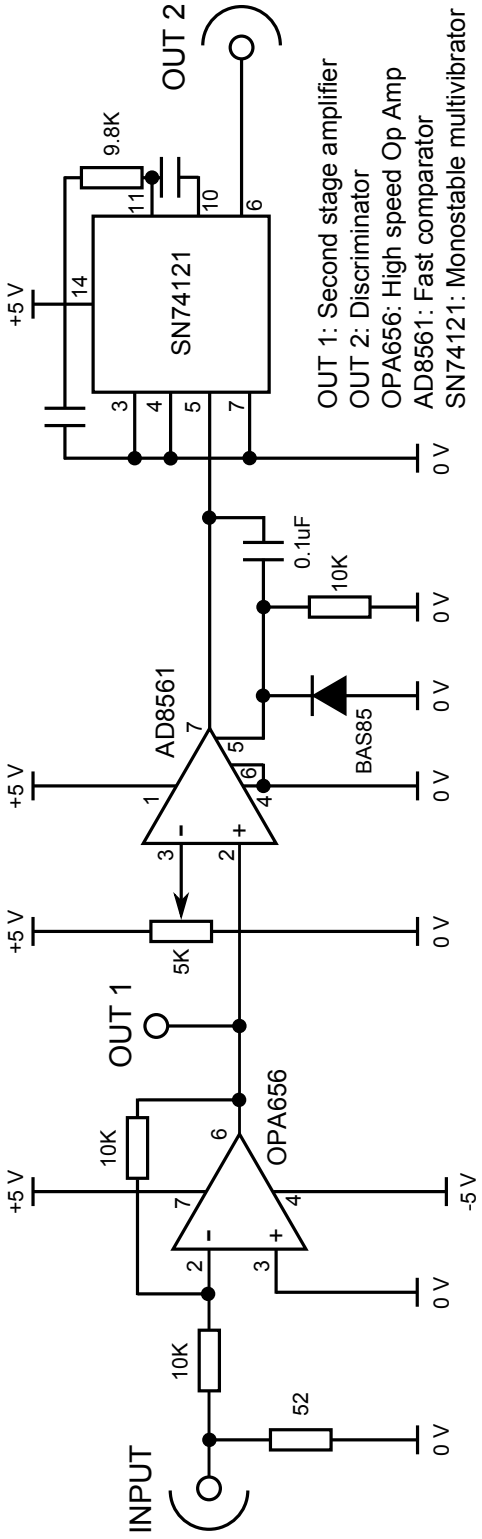

Figure B.2: MCP second stage amplification/discrimininator circuit.

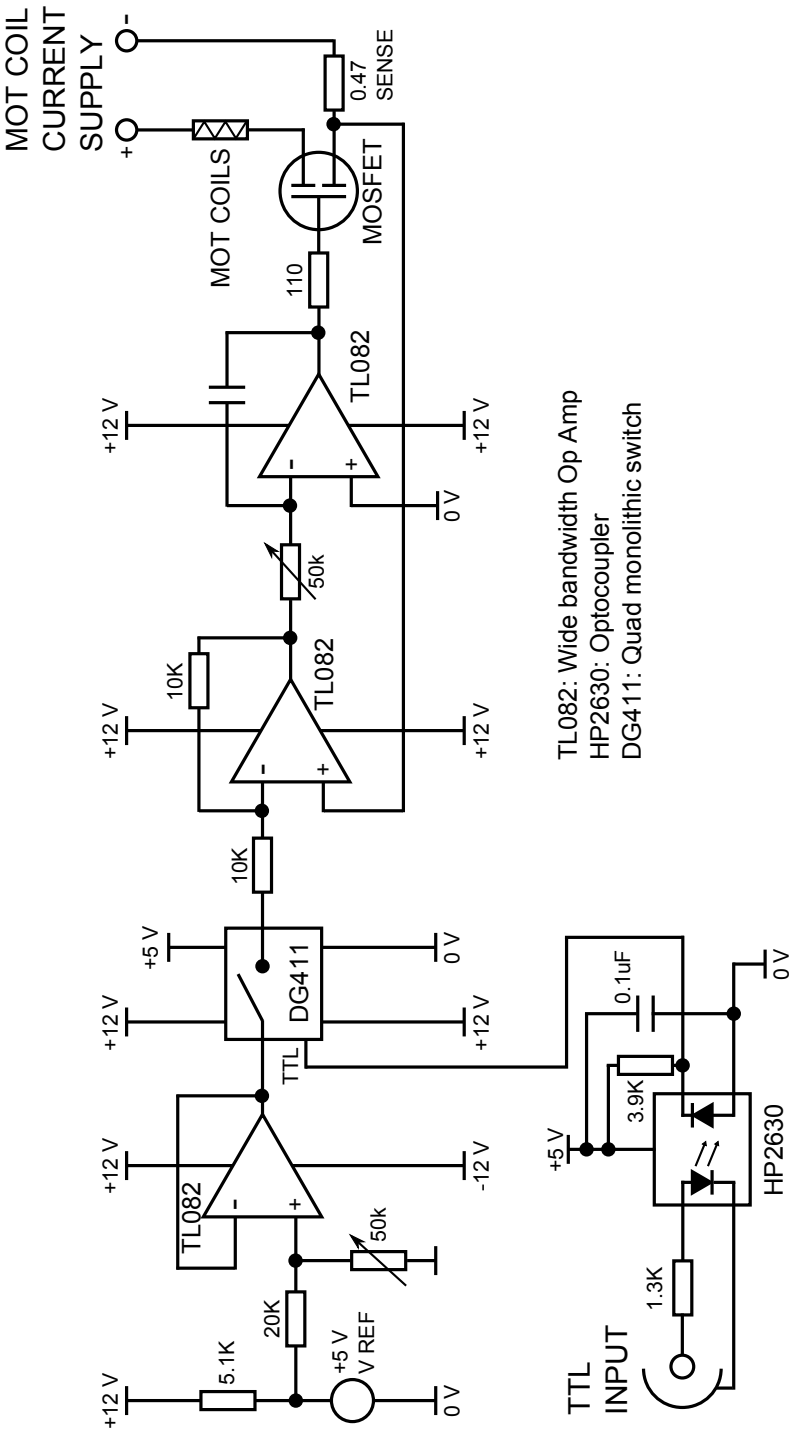

Figure B.3: MOT coil current switching circuit.

Notes on the circuits

The MCP pre-amplifier, fig. B.1, acts as a non-inverting amplifier with a gain of 11 for the output of the MCP. There is a diode bridge to protect against voltage surges.

The output of the pre-amp goes directly to the input of the discriminator circuit, fig. B.2. If OUTPUT 1 of the discriminator circuit is used then the circuit only acts as a secondary (inverting) stage of amplification. If OUTPUT 2 is used then the circuit acts as a discriminator, generating a voltage pulse if the input is over a certain voltage.

The MOT coil switch, fig B.3, allows for switching of the MOT coil supply current, controlled by a TTL. If the switch is opened then the current is dumped across the 0.47 Ω power (sense) resistor. There is a short in the MOT coils. To overcome this the circuit is floated, and the TTL input earth line is isolated from the rest of the circuit using an optocoupler. All of the circuits are capacitively decoupled from ground.

Appendix C

Electric field simulation

The electrodes, as described in section 2.1, are connected to an arbitrary function generator, and driven with up to ±10 V. The typical applied voltage configuration is shown in the inset to fig. C.1(a). One facing pair have a positive voltage applied, another a negative voltage, and all other electrodes are grounded. It is useful to define a set of coordinates. The centre of the coordinate system is the center of the chamber. The line from the positive electrodes to the negative defines the y-axis, and points towards the micro-channel plate detector (MCP). The z-axis points upwards, from one set of electrodes to the other. The x-axis is orthogonal to both of these axes.

The electric field produced by the electrodes is simulated. A three-dimensional coordinate system is set up, with the electrodes represented by regions held at a constant potential. Laplace's equations are solved repeatedly, ensuring that the value of the potential at the electrodes cannot change. For a 100×100×100 pixel grid, with each pixel representing 0.5 mm, it takes about 200 iterations to converge on a solution. The region included in the simulation must be significantly larger than the electrodes, since the first pixel in each dimension wraps onto the last pixel.

The results of the electric field simulation are shown in fig. C.1. For the configuration described, with the positive electrodes held at +1 V and the nega-

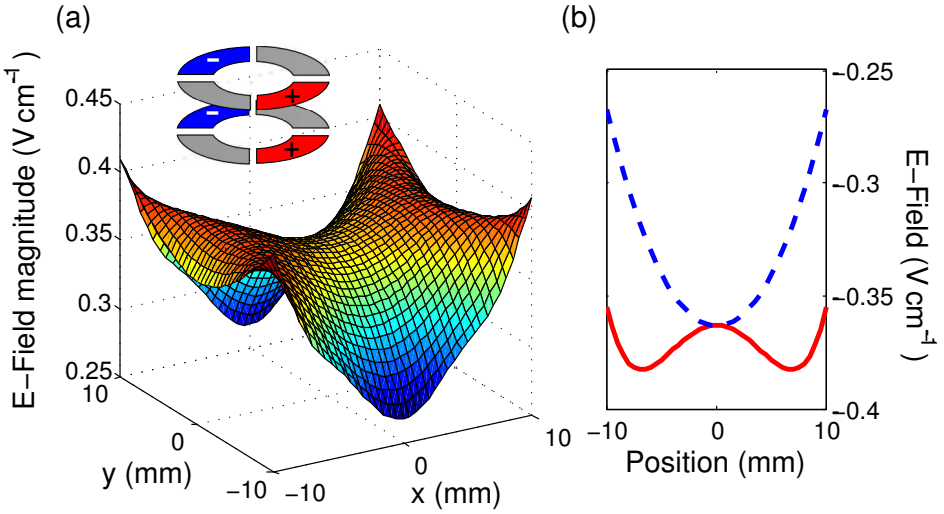

Figure C.1: Simulations of the electric field produced by the electrodes, when charged in the configuration shown in the sub-plot of (a). The y-axis points towards the MCP. (a) The electric field *magnitude* at the center of the chamber, showing that the field is uniform at the position of the atoms. (b) The x (blue dashes) and y (red solid line) components of the electric field along the y-direction in the centre of the chamber.

tive electrodes at -1 V, the field at the centre of the chamber is 0.36 V cm^{-1}, as illustrated by the plot of electric field magnitude in fig. C.1(a). This value varies by less than 1% over a 2mm cube, which easily encompasses the trapped atom cloud. A slice along the y-direction, fig. C.1(b), shows that the electric field points towards the MCP.

As is shown in section 4.2, the applied voltage to electric field calibration factor is measured by comparing a simulated Stark map to data, and the calibration factor is found to be (0.42 ± 0.01) V cm^{-1}. There is a clear discrepancy between this calibration factor, and the one simulated in this appendix. The most likely reason for the lack of agreement is that we do not include any of the vacuum apparatus in the simulation, and there is a large amount of metal (in the form of the MOT coil formers) near to the electrodes. We believe that the conclusions about the *shape* of the electric field drawn from the simulation are correct.

Appendix D

Full derivation of the autoionization cross section

To model our data the optical cross section for the autoionizing transition must be calculated. The cross section σ is related to the autoionizing Ψ_A and bound state Ψ_B wavefunctions [150]:

$$\sigma = \frac{4\pi^2\omega}{c}|\langle\Psi_A|\hat{T}|\Psi_B\rangle|^2\,, \tag{D.1}$$

where ω is the optical frequency of the transition, and $\hat{T}$ the transition dipole operator. Each wavefunction will be considered in turn.

D.1 Derivation

Rydberg state wavefunction

First we consider the $5snd \rightarrow 5pnd$ autoionizing transitions.

The initial Rydberg state can be expressed as a combination of singlet and triplet coupled states, with a mixing angle θ

$$|\Psi_B\rangle = |5snd\rangle = -\sin\theta|^1D_2\rangle + \cos\theta|^3D_2\rangle\,. \tag{D.2}$$

Note that in strontium $5snd$ states, the singlet and triplet state characters cross at $n \simeq 15$ [107], and that at $5s56d\,^1D_2$ state θ will be close to $-\pi/2$. The LS coupled basis can be decoupled into the jj basis:

$$\begin{aligned} |^1D_2\rangle &= a|5s_{1/2}nd_{3/2}\rangle + b|5s_{1/2}nd_{5/2}\rangle \\ |^3D_2\rangle &= c|5s_{1/2}nd_{3/2}\rangle + d|5s_{1/2}nd_{5/2}\rangle\,. \end{aligned} \tag{D.3}$$

The a, b, c, d coefficients are calculated through 9-j symbols. Explicitly, for example

$$\begin{aligned} &\left|5s, nd, s_1 = \tfrac{1}{2}, s_2 = \tfrac{1}{2}, j_1 = \tfrac{1}{2}, j_2 = \tfrac{3}{2}, J = 2, M_J = 2\right\rangle \\ &= \alpha \begin{Bmatrix} l_1 & s_1 & j_1 \\ l_2 & s_2 & j_2 \\ L & S & J \end{Bmatrix} \left|5s, nd, j_1 = \tfrac{1}{2}, j_2 = \tfrac{3}{2}, D, S = \text{Singlet}, J = 2, M_J = 2\right\rangle \\ &\alpha = \sqrt{(2L+1)(2S+1)(2j_1+1)(2j_2+1)}\,, \end{aligned} \tag{D.4}$$

where 1 labels the inner valence electron, and 2 labels the electron in the Rydberg state. Transforming into a jj uncoupled basis best describes isolated core excitation (ICE) [146], where the j of the inner valence electron changes, but the j of the Rydberg electron does not. Combining eqns. (D.2) and (D.3), the bound Rydberg state can be written as

$$\begin{aligned} |\Psi_B\rangle = &(\sqrt{3/5}\cos\theta - \sqrt{2/5}\sin\theta)|5s_{1/2}nd_{3/2}\rangle \\ &- (\sqrt{2/5}\cos\theta + \sqrt{3/5}\sin\theta)|5s_{1/2}nd_{5/2}\rangle\,. \end{aligned} \tag{D.5}$$

Autoionizing state wavefunction

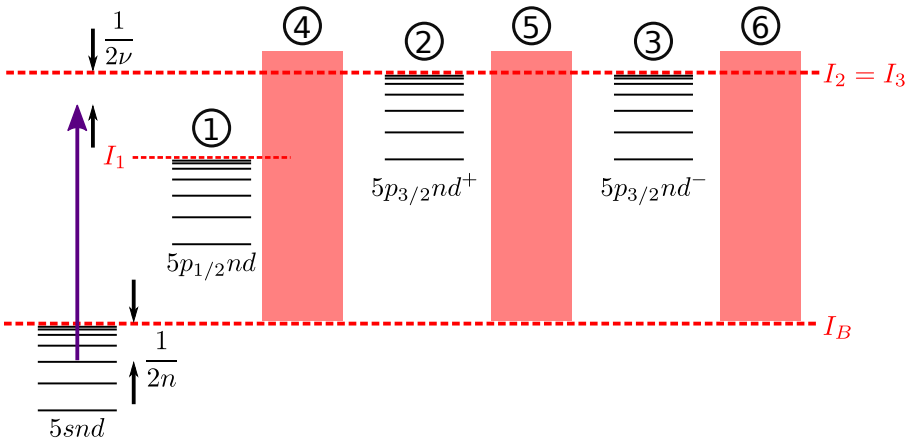

Figure D.1: Energy level diagram describing the autoionization of the $5snd$ series by ICE. The shaded areas are continuum (open) channels, and the number in the circle labels the channel. The dotted lines denote the channel limits. The bound ($5snd$) state limit I_B is the limit for the open channels. $|5p_{3/2}nd\rangle^+ = \cos\phi|5p_{3/2}nd_{3/2}\rangle + \sin\phi|5p_{3/2}nd_{5/2}\rangle$ and $|5p_{3/2}nd\rangle^- = -\sin\phi|5p_{3/2}nd_{3/2}\rangle + \cos\phi|5p_{3/2}nd_{5/2}\rangle$ [150]. The angle ϕ characterizes the mixing between the m_j states.

The analysis by [150] found that six channels were enough to describe the the $5snd \rightarrow 5pnd$ autoionizing transitions. These channels are illustrated in fig. D.1. Each channel has a limit. For channels 1-3, shown in the figure, this is the series limit of the autoionizing series. For the continuum channels this is the limit of the bound $5snd$ Rydberg series. A channel is called "open" if the excitation is higher in energy than the channel limit, otherwise it is "quasibound". The continuum channels are all open. The autoionizing state wavefunction is given by

$$|\Psi_A\rangle = \sum_i Z_i \psi_i \,, \tag{D.6}$$

where i labells the channel, Z is the density of autoionizing states, and ψ

is the channel wavefunction. The sum need only be over the quasibound channels, as the continuum wavefunctions are (by convention) normalised per unit energy: $Z^2_{open} \equiv 1$ [169]. However, the coupling to the open channels plays a critical role in the determination of Z for the quasibound channels, so open channels are still important.

In our experiments, a laser at 408 nm addresses states in the $5p_{3/2}nd$ channels, higher in energy than the limit of channel 1 ($5p_{1/2}nd$), so channel 1 is open and only two quasibound channels need be considered in the autoionization wavefunction

$$\begin{aligned} |\Psi_A\rangle &= Z_2|5p_{3/2}nd\rangle^+ + Z_3|5p_{3/2}nd\rangle^- \\ &= (Z_2\cos\phi - Z_3\sin\phi)|5p_{3/2}nd_{3/2}\rangle \\ &\quad + (Z_3\cos\phi + Z_2\sin\phi)|5p_{3/2}nd_{5/2}\rangle\,. \end{aligned} \tag{D.7}$$

Transition matrix element

Equations (D.5) and)D.7) are combined to find the autoionization transition matrix element:

$$\begin{aligned} &\langle\Psi_A|\hat{T}|\Psi_B\rangle \\ &= (Z_2\cos\phi - Z_3\sin\phi)(\sqrt{3/5}\cos\theta - \sqrt{2/5}\sin\theta)\langle 5p_{3/2}nd_{3/2}|\hat{T}|5s_{1/2}nd_{3/2}\rangle \\ &\quad - (Z_3\cos\phi + Z_2\sin\phi)(\sqrt{2/5}\cos\theta + \sqrt{3/5}\sin\theta)\langle 5p_{3/2}nd_{5/2}|\hat{T}|5s_{1/2}nd_{5/2}\rangle \\ &= Z_-(\phi,\theta)\langle 5p_{3/2}nd_{3/2}|\hat{T}|5s_{1/2}nd_{3/2}\rangle - Z_+(\phi,\theta)\langle 5p_{3/2}nd_{5/2}|\hat{T}|5s_{1/2}nd_{5/2}\rangle\,, \end{aligned} \tag{D.8}$$

which assumes that the j of the Rydberg electron does not change during the transition. As a reminder, θ is the mixing angle between singlet and triplet states, and ϕ the mixing angle between m_j states. This expression is valid for $|J=2, M_J=2\rangle \rightarrow |J=3, M_J=3\rangle$ transitions only. Equation (D.8) is split

into an uncoupled $|(n_1 l_1)\, j_1, m_{J1}\rangle|(n_2 l_2)\, j_2, m_{J2}\rangle$ basis, so that each electron can be considered independently. To uncouple, Clebsch-Gordan coefficients C are used, and a sum is made over the allowed values of m_j:

$$|J, M_J\rangle = C^{j_1,m_{j1}}_{j_2,m_{j2},J,M}|(n_1, l_1)\, j_1, m_{j1}\rangle|(n_2, l_2)\, j_2, m_{j2}\rangle\,, \tag{D.9}$$

e.g.

$$\begin{aligned}|5s_{1/2}nd_{5/2}\rangle = C^{1/2,1/2}_{5/2,3/2,2,2}\left|(5s)\,\tfrac{1}{2}, \tfrac{1}{2}\right\rangle|(nd)\,\tfrac{5}{2}, \tfrac{3}{2}\rangle \\ + C^{1/2,-1/2}_{5/2,5/2,2,2}\left|(5s)\,\tfrac{1}{2}, -\tfrac{1}{2}\right\rangle|(nd)\,\tfrac{5}{2}, \tfrac{5}{2}\rangle\ .\end{aligned}$$

If it is assumed that $\hat{T}$ only acts on the inner valence electron (ICE), driving the ion transition, then

$$\begin{aligned}&\langle\Psi_A|\hat{T}|\Psi_B\rangle \\ &= \Bigg[Z_-\left\langle(5p)\,\tfrac{3}{2}, \tfrac{3}{2}\right|\hat{T}\left|(5s)\,\tfrac{1}{2}, \tfrac{1}{2}\right\rangle - Z_+\Bigg(\tfrac{1}{4}\left\langle(5p)\,\tfrac{3}{2}, \tfrac{3}{2}\right|\hat{T}\left|(5s)\,\tfrac{1}{2}, \tfrac{1}{2}\right\rangle \\ &\quad + \frac{5}{4\sqrt{3}}\left\langle(5p)\,\tfrac{3}{2}, \tfrac{1}{2}\right|\hat{T}\left|(5s)\,\tfrac{1}{2}, -\tfrac{1}{2}\right\rangle\Bigg)\Bigg] \times \langle\nu_a d|\nu_b d\rangle\,,\end{aligned} \tag{D.10}$$

where terms in which the m_j of the Rydberg electron changes are discarded (since it is the inner valence electron that is excited). The term $\langle\nu_a d|\nu_b d\rangle$ is the overlap integral for the Rydberg electron, which doesn't depend on j_2 or m_{j2}. Principal quantum number n has been replaced by the effective quantum number ν for clarity, since the overlap integral depends on the bound series $5s\nu_b d$ and the autoionizing series $5p_{3/2}\nu_a d$. Note that if channel 1 ($5p_{1/2}\nu_a d$) was not open one would have to consider $\nu_a(5p_{1/2})$ and $\nu_a(5p_{3/2})$ separately.

Next, the Wigner-Eckart theorem is used to calculate the reduced matrix-elements for the ion transition, which removes any m_j dependence from the matrix-element. The Wigner-Eckart theorem yields:

$$\langle j, m_j|\hat{T}|j', m_j'\rangle = (-1)^{j'-m_j'} \begin{pmatrix} 1 & j & j' \\ q & m_j & -m_j' \end{pmatrix} \langle j'||\hat{T}||j\rangle \,, \tag{D.11}$$

where $q = m - m'$, and the term in parentheses is a 3-j symbol. The double pipes indicate a reduced matrix-element. As an explicit example

$$\left\langle (5p)\, \tfrac{3}{2}, \tfrac{3}{2}\right| \hat{T} \left|(5s)\, \tfrac{1}{2}, \tfrac{1}{2}\right\rangle = -\tfrac{1}{2}\langle (5p)\ {}^2P_{3/2}||\hat{T}||(5s)\ {}^2S_{1/2}\rangle \,. \tag{D.12}$$

Finally, the j dependence is removed from the matrix-element completely, using 6-j symbols:

$$\begin{aligned} &\langle S, L, J||\hat{T}||S, L', J'\rangle = \alpha \begin{Bmatrix} L & J & S \\ J' & L' & 1 \end{Bmatrix} \langle L||\hat{T}||L'\rangle \,, \\ &\alpha = \sqrt{(2J+1)(2J'+1)} \,. \end{aligned} \tag{D.13}$$

Again, explicitly:

$$\langle (5p)\ {}^2P_{3/2}||\hat{T}||(5s)\ {}^2S_{1/2}\rangle = \sqrt{8} \begin{Bmatrix} 1 & 3/2 & 1/2 \\ 1/2 & 0 & 1 \end{Bmatrix} \langle 5p||\hat{T}||5s\rangle \,. \tag{D.14}$$

Equation D.10 can now be simplified:

$$\langle \Psi_A|\hat{T}|\Psi_B\rangle = \left[\frac{1}{\sqrt{3}} Z_- + \frac{2}{3\sqrt{3}} Z_+\right] \langle 5p||\hat{T}||5s\rangle \langle \nu_a d|\nu_b d\rangle \,. \tag{D.15}$$

The prefactors to the Z coefficients come from the decompositions that have been made, for a $|J = 2, M_J = 2\rangle \rightarrow |J = 3, M_J = 3\rangle$ transition. Since the polarization of our autoionizing laser is not well defined, in the final expression an average is made over all possible J and M_J, which gives the following for the $5snd \rightarrow 5p_{3/2}nd$ transitions:

$$\langle \Psi_A | \hat{T} | \Psi_B \rangle = [0.36 Z_- + 0.24 Z_+] \langle 5p || \hat{T} || 5s \rangle \langle \nu_a d | \nu_b d \rangle \,. \tag{D.16}$$

The $5sns \rightarrow 5pns$utoionizing transitions

Six channels are required to describe the $5sns \rightarrow 5pns$ autoionizing transitions [123]. The three quasibound channels are: channel 1: $5p_{3/2}\nu_a s$; channel 2: $5p_{1/2}\nu_a s$; and channel 3: $5p_{1/2}\nu_a d_{3/2}$. For our experiment channels 2 and 3 are open, so channel 1 is the only quasibound channel. This means that any factors due to angular momentum algebra etc. can be absorbed into an arbitrary amplitude scaling, and we have a simple expression for the autoionizing transition:

$$\langle \Psi_A | \hat{T} | \Psi_B \rangle \propto Z \langle 5p || \hat{T} || 5s \rangle \langle \nu_a s | \nu_b s \rangle \,. \tag{D.17}$$

Calculation of the density of states

The density of states Z can be found by solving the following set of equations [170], where i, k label each of the channels:

$$\begin{aligned} [R_{ik} + \tan(\pi\eta_i)\tilde{\delta}_{ik}] a_k &= 0 \\ a_k &= Z_k \cos(\pi\eta_k) \,. \end{aligned} \tag{D.18}$$

For quasibound channels $\eta_i = \delta_i + \nu_i$ (δ_i is the quantum defect of channel i), and for open channels it is the relative phase divided by π, which is the same for every open channel, and is constrained by the following determinant condition [170]:

$$|\tan(\pi\eta_i)\tilde{\delta}_{ik} + R_{ik}| = 0 \,, \tag{D.19}$$

so should not be considered a fitting parameter. **R** is a symmetric matrix whose entries R_{ik} describe the coupling between channels i and k, and $\tilde{\delta}_{ik}$ is the Kronecker delta (marked with a tilde to distinguish it from the quantum defect). The entries R_{ii} can be set to zero, as can any continuum-continuum couplings [171].

For the $^1D_2$ autoionizing series channels 2 and 3, $|5p_{3/2}nd\rangle^{\pm}$, are orthogonal, so in this particular case $R_{23} = 0$ [150]. For the $^1S_0$ autoionizing series channels 2 and 3, $5p_{1/2}\nu_a s$ and $5p_{1/2}\nu_a d_{3/2}$, are also orthogonal, so again $R_{23} = 0$ [123]. Hence, in our experiment, the non-zero **R**-matrix parameters are $R_{12}, R_{13}, R_{14}, R_{25}, R_{36}$.

The density of states Z_i is a series of peaks positioned at the energies of the $5pnl$ states particular to the quasibound channel i. When there is more than one quasibound channel the density of states of the different channels add. The width of the peaks is strongly related to the values of the entries in the **R**-matrix, in particular addition of more open channels broadens the line shapes.

D.2 Fitting the autoionization cross section to data

The cross sections for the autoionizing $^1S_0$ and $^1D_2$ states, σ_S and σ_D respectively, can be expressed as:

$$\begin{aligned} \sigma_S &= A_S|Z|^2|\langle\nu_a s|\nu_b s\rangle|^2 \\ \sigma_D &= A_D|[0.36Z_- + 0.24Z_+]|^2|\langle\nu_a d|\nu_b d\rangle|^2 , \end{aligned} \tag{D.20}$$

where the constant terms, including the reduced matrix-element for the core transition, have been adsorbed into amplitude scaling factors.

The overlap integral $\langle \nu_a l | \nu_b l \rangle$ and density of states Z both depend upon the effective quantum number ν. This effective quantum number is a *continuous* variable, and is defined through

$$\nu = \sqrt{\frac{R_{\mathrm{Sr}}}{\mathrm{E_{ion}} - \mathrm{E}}}\,, \tag{D.21}$$

where R_{Sr} is the Rydberg constant for strontium, $\mathrm{E_{ion}}$ the ionization limit, and E the energy *of the excitation laser*. This is the link between performing laser spectroscopy by varying the frequency ω_3 of the autoionizing laser, and the expressions in eqn. (D.20). It should be noted that each quasibound channel has it's own ionization limit $\mathrm{E_{ion}}$, related to the ionic state to which it tends. The values of $\mathrm{E_{ion}}$ for the six-channel models presented in this chapter can be found in table A.1.

The standard unit of autoionization laser frequency we use is the detuning Δ_3 from the ion line $5s_{1/2} \rightarrow 5p_{3/2} = 407.88$ nm [149]. To acquire the spectrum of the autoionizing states the level of ionization that is produced at each detuning Δ_3 is recorded. The autoionization signal $S(\Delta_3)$ is related to the autoionization cross section for a specific angular momentum state σ_L through

$$S(\Delta_3) = \eta N_L \sigma_L(\Delta_3)\,, \tag{D.22}$$

where η is a constant factor that accounts for the detection efficiency and signal-per-ion conversion factor, and N_L is the number of atoms in the Rydberg state. Hence, the autoionization signal $S(\Delta_3)$ is directly proportional to the autoionization cross section $\sigma(\Delta_3)$, and in this way the experimental data can be modeled.

Fit parameters

A fit to the experimentally measured autoionization spectrum, defined through eqn. (D.22), requires the following parameters: an amplitude $B = \eta N_L A_L$; the inter-channel couplings $R_{12}, R_{13}, R_{14}, R_{25}, R_{36}$, the quantum defects of the bound Rydberg series δ_b and autoionizing states δ_a; and, in the case of the $^1D_2$ series, the singlet-triplet (θ), and m_j (ϕ), mixing angles.

Excepting the amplitude B, all of these values have been measured by studying many states in an autoionizing series ([123] for the $^1S_0$ series, [150] for the $^1D_2$ series).

For the $^1D_2$ series, the $\mathbf{R}-$matrix parameters are set to the literature values, except for R_{36}, where a change of $< 5\%$ improved the agreement with our data. The quantum defect for channel 1 ($5s\nu_b d \rightarrow 5p_{1/2}\nu_a d$) is fixed to the literature value, since in our experiment and in [150] this channel is open. The quantum defects of channels 2 and 3 vary, as the previous experiment only went as high as $n = 36$. The bound state quantum defect δ_b from [111] is used. The m_j mixing angle ϕ is allowed to vary, since our polarization is not the same as in [150]. The singlet-triplet mixing angle θ tends towards -90° at high n (for the $^1D_2$ series) [107], so the value is constrained to $\pm 4°$ either side of this. In total there are five free parameters $B_D, \delta_2, \delta_3, \phi$ and θ, with some constraints, for fitting the autoionization spectra of the $5snd$ Rydberg states.

For the $^1S_0$ series, the $\mathbf{R}-$matrix parameters are set to the literature values [123]. The bound state quantum defect δ_b is taken from [111]. The open channel quantum defects ($\delta_{2,3}$) are fixed to the values from [123]. The quasibound state quantum defect δ_1 is allowed to vary, so for the $^1S_0$ series there are only two free parameters: an amplitude B_S and the quasibound quantum defect δ_1.

	Our fit	From [123]		Our fit	From [123]
R_{12}	0.16	0.16	δ_1	3.42	3.44
R_{13}	0.1	0.1	δ_2	3.41	3.41
R_{14}	0.45	0.45	δ_3	2.10	2.10
R_{25}	0.4	0.4			
R_{36}	0.39	0.39			

Table D.1: The parameters obtained from a six-channel MQDT model fit to the $20\,^1S_0$ autoionization spectrum. Our values are compared to previous work. δ_i is the quantum defect for the quasibound channel i.

Results

The result of fitting eqn. (D.22) to the autoionization spectrum of the $5s20s\,^1S_0$ state is shown in fig. D.2(b), with the fit parameters listed in table D.1. This data was taken with a pulsed dye laser providing the autoionization light (see chapter 5).

The bound state quantum defect of the $20\,^1S_0$ state is $\delta_b = 3.26849$ [111]. The agreement between the six-channel MQDT model and the data is excellent. The value we obtain for the quasibound series quantum defect δ_1 is very similar to the value from [123] (which is quoted without an error bar), as can be seen in table D.1.

The result of fitting eqn. (D.22) to the autoionization spectrum of the $5s19d\,^1D_2$ state is shown in fig. D.2(a), and to the autoionization spectrum of the $5s56d\,^1D_2$ state is shown in fig. D.3(b). A two-channel fit to the $56\,^1D_2$ state autoionization spectrum is shown in fig. D.3(a) for comparison; the six-channel model is clearly better. The effect of interference between the quasibound channels is visible in both the fit and the data through the different widths of the two peaks.

The fit to the $^1D_2$ series data was optimized to the $56\,^1D_2$ state autoionization

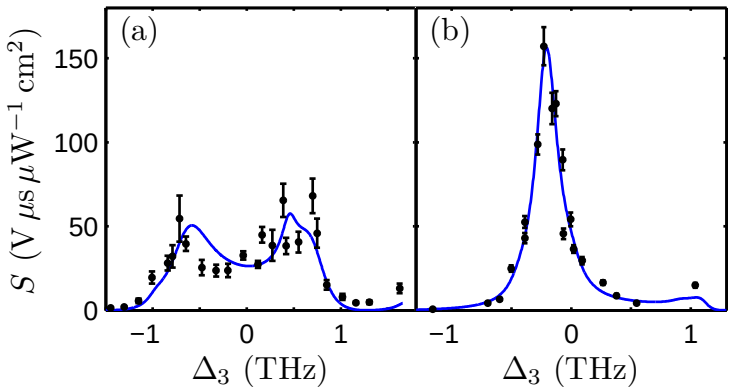

Figure D.2: The autoionization spectra of the (a) $19\,^1D_2$ and (b) $20\,^1S_0$ states. Solid lines are six channel MQDT model fits.

	Our fit	From [150]		Our fit	From [150]
R_{12}	0.4	0.4	δ_1	2.79	2.79±0.02
R_{13}	0.05	0.05	δ_2	2.68	2.78±0.02
R_{14}	0.45	0.45	δ_3	2.89	2.81±0.02
R_{25}	0.61	0.61	θ	-1.30 ($19\,D$), -1.54 ($56\,D$)	-1.29 ($19\,D$)
R_{36}	0.48	0.46	ϕ	0.74 ($19\,D$), 1.24 ($56\,D$)	0.69±0.03

Table D.2: The parameters obtained from six-channel MQDT model fits to the $^1D_2$ series autoionization spectra. Our values are compared to previous work. δ_i is the quantum defect for the quasibound channel i. The value of θ is not listed in [150] for the $56\,^1D_2$ state, however we base it upon the observations of [107].

spectrum. The fit parameters are listed in table D.2. The bound state quantum defect for the $19\,^1D_2$ state is $\delta_b = 2.22364$, and for the $56\,^1D_2$ state $\delta_b = 2.37255$ [111]. The quantum defects that we measure for the quasibound channels are different from the values in [150] outside of the quoted errors, but by less than 4%. This is unsurprising, since the analysis in [150] only went to $n = 36$, and the quantum defects vary with n.

The singlet-triplet mixing angle θ we measure for the $19\,^1D_2$ state is in fair agreement with the value from [150]. The value of θ for the $56\,^1D_2$ state isn't available in the literature, but the value we measure is close to $-\pi/2$, which

is what would be expected at this value of n [107]. The m_j mixing angle ϕ is different for the $19\,{}^1D_2$ and $56\,{}^1D_2$ states, which is expected since the $19\,{}^1D_2$ state data was taken with a pulsed dye laser providing the autoionization light, and the $56\,{}^1D_2$ data with a diode laser, and these lasers have different polarization (see chapter 5). The values of ϕ we measure are different to the value from [150], where the polarization of the autoionizing laser was well defined.

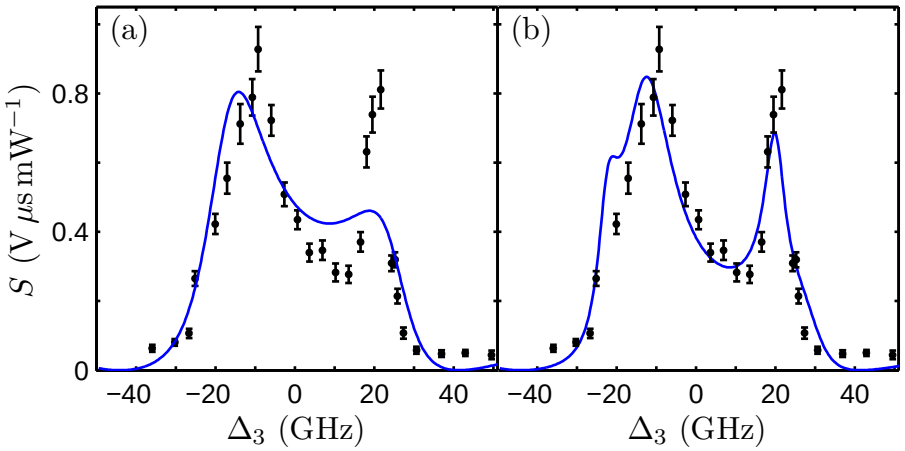

Figure D.3: The autoionization spectrum for the $56\,{}^1D_2$ Rydberg state, $P_2 = 1$ mW. (a) includes a two-channel MQDT model fit (blue line) with a quasibound state quantum defect for the autoionizing $5p_{3/2}56d$ state $\delta_a = 2.77$, and a two-channel $R_{(2)} = 0.77 \pm 0.02$. (b) includes the full six-channel MQDT model fit (blue line). The fit parameters can be found in table D.2.

Bibliography

[1] R. Mukherjee *et al.*, *Many-body physics with alkaline-earth Rydberg lattices* **arXiv:1102.3792** (2011), http://arxiv.org/abs/1102.3792

[2] F Robicheaux, *Transfer of a wavepacket between atoms*, Journal of Physics B: Atomic, Molecular and Optical Physics **43**, 215004 (2010)

[3] B. Vaucher, S. J. Thwaite, and D. Jaksch, *Ultralarge Rydberg dimers in optical lattices*, Phys. Rev. A **78**, 043415 (2008)

[4] Kilian Singer, Jovica Stanojevic, Matthias Weidemüller, and Robin Côté, *Long-range interactions between alkali Rydberg atom pairs correlated to the $ns \rightarrow ns, np \rightarrow np$ and $nd \rightarrow nd$ asymptotes*, Journal of Physics B: Atomic, Molecular and Optical Physics **38**, S295 (2005)

[5] G. Pupillo *et al.*, *Strongly correlated gases of Rydberg-dressed atoms: Quantum and classical dynamics*, Phys. Rev. Lett. **104**, 223002 (2010)

[6] F. Cinti *et al.*, *Supersolid droplet crystal in a dipole-blockaded gas*, Phys. Rev. Lett. **105**, 135301 (2010)

[7] N. Henkel, R. Nath, and T. Pohl, *Three-dimensional roton excitations and supersolid formation in Rydberg-excited Bose-Einstein condensates*, Phys. Rev. Lett. **104**, 195302 (2010)

[8] Y. N. Martinez de Escobar *et al.*, *Bose-Einstein condensation of ^{84}Sr*, Phys. Rev. Lett. **103**, 200402 (2009)

[9] Simon Stellmer *et al.*, *Bose-Einstein condensation of strontium*, Phys. Rev. Lett. **103**, 200401 (2009)

[10] F Maucher *et al.*, *Matter-wave bullets in Rydberg-dressed Bose Einstein condensates* **arXiv:1102.2121** (2011), http://arxiv.org/abs/1102.2121

[11] J. Millen, G. Lochead, and M. P. A. Jones, *Two-electron excitation of an interacting cold Rydberg gas*, Phys. Rev. Lett. **105**, 213004 (2010)

[12] J. Millen *et al.*, *Spectroscopy of a cold strontium Rydberg gas* **arXiv:1102.2715** (2011), http://arxiv.org/abs/1102.2715

[13] I. C. Percival, *Planetary atoms*, Proceedings of the Royal Society of London. A. Mathematical and Physical Sciences **353**, 289–297 (1977)

[14] U. Eichmann, V. Lange, and W. Sandner, *Dipole structure of planetary atoms*, Phys. Rev. Lett. **68**, 21–24 (1992)

[15] N V Prudov and V N Ostrovsky, *Measure of electron correlation in asymmetric doubly excited states*, Journal of Physics B: Atomic, Molecular and Optical Physics **32**, 4163 (1999)

[16] C. E. Simien *et al.*, *Using absorption imaging to study ion dynamics in an ultracold neutral plasma*, Phys. Rev. Lett. **92**, 143001 (2004)

[17] T C Killian *et al.*, *Ultracold neutral plasmas: recent experiments and new prospects*, Journal of Physics A: Mathematical and General **36**, 6077 (2003)

[18] T. Pohl, T. Pattard, and J. M. Rost, *Coulomb crystallization in expanding laser-cooled neutral plasmas*, Phys. Rev. Lett. **92**, 155003 (2004)

[19] J. J. Mestayer *et al.*, *Realization of localized Bohr-like wave packets*, Phys. Rev. Lett. **100**, 243004 (2008)

[20] B Wyker *et al.*, *Decoherence of high-l Rydberg wavepackets by collisions and electrical noise*(2011)

[21] Vera Bendkowsky *et al.*, *Observation of ultralong-range Rydberg molecules*, NATURE **458** (2009), doi:\bibinfo{doi}{10.1038/nature07945}

[22] K. R. Overstreet *et al.*, *Observation of electric-field-induced cs Rydberg atom macrodimers*, NATURE PHYSICS **5**, 581–585 (2009)

[23] H. Schempp *et al.*, *Coherent population trapping with controlled interparticle interactions*, Phys. Rev. Lett. **104**, 173602 (2010)

[24] J. D. Pritchard *et al.*, *Cooperative atom-light interaction in a blockaded Rydberg ensemble*, Phys. Rev. Lett. **105**, 193603 (2010)

[25] Inbal Friedler, David Petrosyan, Michael Fleischhauer, and Gershon Kurizki, *Long-range interactions and entanglement of slow single-photon pulses*, Phys. Rev. A **72**, 043803 (2005)

[26] Thomas F. Gallagher, *Rydberg Atoms* (Cambridge University Press, 1994)

[27] M. Saffman, T. G. Walker, and K. Mölmer, *Quantum information with Rydberg atoms*, Rev. Mod. Phys. **82**, 2313–2363 (2010)

[28] Klaus von Haeften, Tim Laarmann, Hubertus Wabnitz, and Thomas Möller, *The electronically excited states of helium clusters: an unusual example for the presence of Rydberg states in condensed matter*, Journal of Physics B: Atomic, Molecular and Optical Physics **38**, S373 (2005)

[29] B Zygelman, *Recombination and cascade of Rydberg antihydrogen*, Journal of Physics B: Atomic, Molecular and Optical Physics **38**, S387 (2005)

[30] K Tökési, B Juhász, and J Burgdörfer, *Exotic Rydberg atom formation in low-energy antiproton-helium collisions*, Journal of Physics B: Atomic, Molecular and Optical Physics **38**, S401 (2005)

[31] D. Jaksch *et al.*, *Fast quantum gates for neutral atoms*, Phys. Rev. Lett. **85**, 2208–2211 (2000)

[32] M. D. Lukin *et al.*, *Dipole blockade and quantum information processing in mesoscopic atomic ensembles*, Phys. Rev. Lett. **87**, 037901 (2001)

[33] Alpha Gaetan *et al.*, *Observation of collective excitation of two individual atoms in the Rydberg blockade regime*, NATURE PHYSICS **5**, 115–118 (2009)

[34] E. Urban *et al.*, *Observation of Rydberg blockade between two atoms*, NATURE PHYSICS **5**, 110–114 (2009)

[35] X. L. Zhang *et al.*, *Deterministic entanglement of two neutral atoms via Rydberg blockade*, Phys. Rev. A **82**, 030306 (2010)

[36] T. Wilk *et al.*, *Entanglement of two individual neutral atoms using Rydberg blockade*, Phys. Rev. Lett. **104**, 010502 (2010)

[37] L. Isenhower *et al.*, *Demonstration of a neutral atom controlled-not quantum gate*, Phys. Rev. Lett. **104**, 010503 (2010)

[38] Kilian Singer *et al.*, *Suppression of excitation and spectral broadening induced by interactions in a cold gas of Rydberg atoms*, Phys. Rev. Lett. **93**, 163001 (2004)

[39] D. Tong *et al.*, *Local blockade of Rydberg excitation in an ultracold gas*, Phys. Rev. Lett. **93**, 063001 (2004)

[40] K. Afrousheh *et al.*, *Spectroscopic observation of resonant electric dipole-dipole interactions between cold Rydberg atoms*, Phys. Rev. Lett. **93**, 233001 (2004)

[41] Thibault Vogt *et al.*, *Dipole blockade at förster resonances in high resolution laser excitation of Rydberg states of cesium atoms*, Phys. Rev. Lett. **97**, 083003 (2006)

[42] Rolf Heidemann *et al.*, *Rydberg excitation of Bose-Einstein condensates*, Phys. Rev. Lett. **100**, 033601 (2008)

[43] B Sun and F Robicheaux, *Numerical study of two-body correlation in a 1d lattice with perfect blockade*, New Journal of Physics **10**, 045032 (2008)

[44] B. Olmos, R. González-Férez, and I. Lesanovsky, *Fermionic collective excitations in a lattice gas of Rydberg atoms*, Phys. Rev. Lett. **103**, 185302 (2009)

[45] T. Pohl, E. Demler, and M. D. Lukin, *Dynamical crystallization in the dipole blockade of ultracold atoms*, Phys. Rev. Lett. **104**, 043002 (2010)

[46] Hendrik Weimer and Hans Peter Büchler, *Two-stage melting in systems of strongly interacting Rydberg atoms*, Phys. Rev. Lett. **105**, 230403 (2010)

[47] Igor Lesanovsky, *Many-body spin interactions and the ground state of a dense Rydberg lattice gas*, Phys. Rev. Lett. **106**, 025301 (2011)

[48] M. Müller *et al.*, *Mesoscopic Rydberg gate based on electromagnetically induced transparency*, Phys. Rev. Lett. **102**, 170502 (2009)

[49] T. C. Killian *et al.*, *Creation of an ultracold neutral plasma*, Phys. Rev. Lett. **83**, 4776–4779 (1999)

[50] J. L. Roberts, C. D. Fertig, M. J. Lim, and S. L. Rolston, *Electron temperature of ultracold plasmas*, Phys. Rev. Lett. **92**, 253003 (2004)

[51] Setsuo Ichimaru, *Strongly coupled plasmas: high-density classical plasmas and degenerate electron liquids*, Rev. Mod. Phys. **54**, 1017–1059 (1982)

[52] Edward Shuryak, *Physics of strongly coupled quark-gluon plasma*, Progress in Particle and Nuclear Physics **62**, 48 – 101 (2009), ISSN 0146-6410

[53] Thomas C. Killian, *Ultracold neutral plasmas*, Science **316**, 705–708 (2007)

[54] T C Killian *et al.*, *Ultracold neutral plasmas: recent experiments and new prospects*, Journal of Physics A: Mathematical and General **36**, 6077 (2003)

[55] T. C. Killian *et al.*, *Formation of Rydberg atoms in an expanding ultracold neutral plasma*, Phys. Rev. Lett. **86**, 3759–3762 (2001)

[56] Wenhui Li *et al.*, *Evolution dynamics of a dense frozen Rydberg gas to plasma*, Phys. Rev. A **70**, 042713 (2004)

[57] Y. Li, T. Ido, T. Eichler, and H. Katori, *Narrow-line diode laser system for laser cooling of strontium atoms on the intercombination transition*, Applied Physics B: Lasers and Optics **78**, 315–320 (2004), ISSN 0946-2171

[58] A. Walz-Flannigan, J. R. Guest, J.-H. Choi, and G. Raithel, *Cold-Rydberg-gas dynamics*, Phys. Rev. A **69**, 063405 (2004)

[59] T. Pohl, T. Pattard, and J. M. Rost, *Plasma formation from ultracold Rydberg gases*, Phys. Rev. A **68**, 010703 (2003)

[60] Hidetoshi Katori, Tetsuya Ido, Yoshitomo Isoya, and Makoto Kuwata-Gonokami, *Magneto-optical trapping and cooling of strontium atoms down to the photon recoil temperature*, Phys. Rev. Lett. **82**, 1116–1119 (1999)

[61] Xinye Xu *et al.*, *Cooling and trapping of atomic strontium*, J. Opt. Soc. Am. B **20**, 968–976 (2003)

[62] Andrei Derevianko, *Feasibility of cooling and trapping metastable alkaline-earth atoms*, Phys. Rev. Lett. **87**, 023002 (2001)

[63] Andrei Derevianko *et al.*, *Ultracold collision properties of metastable alkaline-earth atoms*, Phys. Rev. Lett. **90**, 063002 (2003)

[64] Martin M. Boyd *et al.*, *Optical atomic coherence at the 1-second time scale*, Science **314**, 1430–1433 (2006)

[65] Masao Takamoto *et al.*, *Improved frequency measurement of a one-dimensional optical lattice clock with a spin-polarized fermionic* ^{87}Sr *isotope*, Journal of the Physical Society of Japan **75**, 104302 (2006)

[66] Rodolphe Le Targat *et al.*, *Accurate optical lattice clock with* ^{87}Sr *atoms*, Phys. Rev. Lett. **97**, 130801 (2006)

[67] Martin M. Boyd *et al.*, ^{87}Sr *lattice clock with inaccuracy below* 10^{-15}, Phys. Rev. Lett. **98**, 083002 (2007)

[68] S. G. Porsev, Andrew D. Ludlow, Martin M. Boyd, and Jun Ye, *Determination of Sr properties for a high-accuracy optical clock*, Phys. Rev. A **78**, 032508 (2008)

[69] S. Blatt *et al.*, *New limits on coupling of fundamental constants to gravity using* ^{87}Sr *optical lattice clocks*, Phys. Rev. Lett. **100**, 140801 (2008)

[70] Andrew J. Daley, Martin M. Boyd, Jun Ye, and Peter Zoller, *Quantum computing with alkaline-earth-metal atoms*, Phys. Rev. Lett. **101**, 170504 (2008)

[71] A. V. Gorshkov *et al.*, *Alkaline-earth-metal atoms as few-qubit quantum registers*, Phys. Rev. Lett. **102**, 110503 (2009)

[72] William D. Phillips and Harold Metcalf, *Laser deceleration of an atomic beam*, Phys. Rev. Lett. **48**, 596–599 (1982)

[73] J. Dalibard and C. Cohen-Tannoudji, *Laser cooling below the doppler limit by polarization gradients: simple theoretical models*, J. Opt. Soc. Am. B **6**, 2023–2045 (1989)

[74] E. M. Bridge, J. Millen, C. S. Adams, and M. P. A. Jones, *A vapor cell based on dispensers for laser spectroscopy*, Rev. Sci. Instrum. **80**, 013101 (2009)

[75] J.A.C. Gallas, G. Leuchs, H. Walther, and H. Figger, *Rydberg atoms: High-resolution spectroscopy and radiation interaction–Rydberg molecules*, Advances in Atomic and Molecular Physics **20**, 413 – 466 (1985), ISSN 0065-2199

[76] G. De Maria and V. Piacente, *Vapor pressures of calcium and strontium by transpiration method*, The Journal of Chemical Thermodynamics **6**, 1 – 7 (1974), ISSN 0021-9614

[77] I. Courtillot *et al.*, *Efficient cooling and trapping of strontium atoms*, Opt. Lett. **28**, 468–470 (2003)

[78] C. J. Dedman *et al.*, *Optimum design and construction of a zeeman slower for use with a magneto-optic trap*, Review of Scientific Instruments **75**, 5136–5142 (2004)

[79] U. Raitzsch R. Löw *et al.*, *Apparatus for excitation and detection of Rydberg atoms in quantum gases* **arXiv:0706.2639v1** (2007), http://arxiv.org/abs/0706.2639v1

[80] A. White, *Frequency stabilization of gas lasers*, Quantum Electronics, IEEE Journal of **1**, 349 – 357 (1965), ISSN 0018-9197

[81] Gary C. Bjorklund, *Frequency-modulation spectroscopy: a new method for measuring weak absorptions and dispersions*, Opt. Lett. **5**, 15–17 (1980)

[82] Jon H. Shirley, *Modulation transfer processes in optical heterodyne saturation spectroscopy*, Opt. Lett. **7**, 537–539 (1982)

[83] D J McCarron, S A King, and S L Cornish, *Modulation transfer spectroscopy in atomic rubidium*, Measurement Science and Technology **19**, 105601 (2008)

[84] R. P. Abel *et al.*, *Laser frequency stabilization to excited state transitions using electromagnetically induced transparency in a cascade system*, Applied Physics Letters **94**, 071107 (2009)

[85] G. Wasik, W. Gawlik, J. Zachorowski, and W. Zawadzki, *Laser frequency stabilization by doppler-free magnetic dichroism*, Applied Physics B: Lasers and Optics **75**, 613–619 (2002), ISSN 0946–2171

[86] C. Wieman and T. W. Hänsch, *Doppler-free laser polarization spectroscopy*, Phys. Rev. Lett. **36**, 1170–1173 (1976)

[87] C. Javaux *et al.*, *Modulation-free pump-probe spectroscopy of strontium atoms*, Eur. Phys. J. D **57**, 151–154 (2010)

[88] J. A. Neuman, P. Wang, and A. Gallagher, *Robust high-temperature sapphire cell for metal vapors*, Review of Scientific Instruments **66**, 3021–3023 (1995)

[89] G. Philip, *An atomic jet in a heat pipe for multiphoton spectroscopy*, Review of Scientific Instruments **78**, 113101 (2007)

[90] S Mauger, J Millen, and M P A Jones, *Spectroscopy of strontium Rydberg states using electromagnetically induced transparency*, Journal of Physics B: Atomic, Molecular and Optical Physics **40**, F319 (2007)

[91] C P Pearman *et al.*, *Polarization spectroscopy of a closed atomic transition: applications to laser frequency locking*, Journal of Physics B: Atomic, Molecular and Optical Physics **35**, 5141 (2002)

[92] M. L. Harris *et al.*, *Polarization spectroscopy in rubidium and cesium*, Phys. Rev. A **73**, 062509 (2006)

[93] Steven Chu *et al.*, *Three-dimensional viscous confinement and cooling of atoms by resonance radiation pressure*, Phys. Rev. Lett. **55**, 48–51 (1985)

[94] *Atomic Physics* (Oxford Master Series in Atomic, Optical and Laser Physics, 2006)

[95] K. M. F. Magalhães *et al.*, *The escape velocity in a magneto-optical trap and its importance to trap loss investigation*, Laser Physics **12**, 145–151 (2002)

[96] B Ueberholz *et al.*, *Cold collisions in a high-gradient magneto-optical trap*, Journal of Physics B: Atomic, Molecular and Optical Physics **35**, 4899 (2002)

[97] Takayuki Kurosu and Fujio Shimizu, *Laser cooling and trapping of calcium and strontium*, Japanese Journal of Applied Physics **29**, L2127–L2129 (1990)

[98] Masami Yasuda and Hidetoshi Katori, *Lifetime measurement of the $^3p_2$ metastable state of strontium atoms*, Phys. Rev. Lett. **92**, 153004 (2004)

[99] Paul D. Lett *et al.*, *Observation of atoms laser cooled below the doppler limit*, Phys. Rev. Lett. **61**, 169–172 (1988)

[100] Thierry Chanelière *et al.*, *Extra-heating mechanism in doppler cooling experiments*, J. Opt. Soc. Am. B **22**, 1819–1828 (2005)

[101] Wang Shao-Kai *et al.*, *Cooling and trapping 88 Sr atoms with 461 nm laser*, Chinese Physics Letters **26**, 093202 (2009)

[102] K. I. Lee, J. A. Kim, H. R. Noh, and W. Jhe, *Single-beam atom trap in a pyramidal and conical hollow mirror*, Opt. Lett. **21**, 1177–1179 (1996)

[103] J. J. Arlt *et al.*, *A pyramidal magneto-optical trap as a source of slow atoms*, Optics Communications **157**, 303 – 309 (1998), ISSN 0030-4018

[104] I. I. Beterov, I. I. Ryabtsev, D. B. Tretyakov, and V. M. Entin, *Quasiclassical calculations of blackbody-radiation-induced depopulation rates and effective lifetimes of Rydberg ns , np , and nd alkali-metal atoms with* $n \leq 80$, Phys. Rev. A **79**, 052504 (2009)

[105] M. P. Robinson *et al.*, *Spontaneous evolution of Rydberg atoms into an ultracold plasma*, Phys. Rev. Lett. **85**, 4466–4469 (2000)

[106] W R S Garton and K Codling, *Ultra-violet extensions of the arc spectra of the alkaline earths: The absorption spectrum of strontium vapour*, Journal of Physics B: Atomic and Molecular Physics **1**, 106 (1968)

[107] Peter Esherick, *Bound, even-parity* $j = 0$ *and* $j = 2$ *spectra of Sr*, Phys. Rev. A **15**, 1920–1936 (1977)

[108] P. Esherick, J. J. Wynne, and J. A. Armstrong, *Spectroscopy of 3 p0 states of alkaline earths*, Opt. Lett. **1**, 19–21 (1977)

[109] J R Rubbmark and S A Borgström, *Rydberg series in strontium found in absorption by selectively laser-excited atoms*, Physica Scripta **18**, 196 (1978)

[110] J. A. Armstrong, J. J. Wynne, and P. Esherick, *Bound, odd-parity* $j =$ *1 spectra of the alkaline earths: Ca, Sr, and ba*, J. Opt. Soc. Am. **69**, 211–230 (1979)

[111] R. Beigang *et al.*, *Sr $5p_{1/2}ns_{1/2}$ and $5p_{3/2}ns_{1/2}$ j=1 autoionizing states*, Optics Communications **42**, 19–24 (1982)

[112] R. Beigang *et al.*, *Determination of absolute level energies of 5sns1s0 and 5snd1d2 Rydberg series of Sr*, Optics Communications **42**, 19 – 24 (1982), ISSN 0030-4018

[113] R Beigang *et al.*, *One-photon laser spectroscopy of Rydberg series from metastable levels in calcium and strontium*, Physica Scripta **26**, 183 (1982)

[114] R Beigang and D Schmidt, *Two-channel mqdt analysis of bound 5 snd 3 d 1,3 Rydberg states of strontium*, Physica Scripta **27**, 172 (1983)

[115] C. J. Dai, *Perturbed $5snd^{1,3}d_2$ Rydberg series of Sr*, Phys. Rev. A **52**, 4416–4424 (1995)

[116] A. K. Mohapatra, T. R. Jackson, and C. S. Adams, *Coherent optical detection of highly excited Rydberg states using electromagnetically induced transparency*, Phys. Rev. Lett. **98**, 113003 (2007)

[117] Wenhui Li, Paul J. Tanner, and T. F. Gallagher, *Dipole-dipole excitation and ionization in an ultracold gas of Rydberg atoms*, Phys. Rev. Lett. **94**, 173001 (2005)

[118] Wenhui Li *et al.*, *Evolution dynamics of a dense frozen Rydberg gas to plasma*, Phys. Rev. A **70**, 042713 (2004)

[119] I. I. Beterov *et al.*, *Ionization of sodium and rubidium ns , np , and nd Rydberg atoms by blackbody radiation*, Phys. Rev. A **75**, 052720 (2007)

[120] T. Amthor *et al.*, *Mechanical effect of van der waals interactions observed in real time in an ultracold Rydberg gas*, Phys. Rev. Lett. **98**, 023004 (2007)

[121] A. Reinhard *et al.*, *Rydberg-Rydberg collisions: Resonant enhancement of state mixing and penning ionization*, Phys. Rev. Lett. **100**, 123007 (2008)

[122] A. Giusti-Suzor and P. Zoller, *Rydberg electrons in laser fields: A finite-range-interaction problem*, Phys. Rev. A **36**, 5178–5188 (1987)

[123] Emily Y. Xu, Yifu Zhu, Oliver C. Mullins, and T. F. Gallagher, *Sr $5p_1/2ns_1/2$ and $5p_3/2ns_1/2$ j=1 autoionizing states*, Phys. Rev. A **33**, 2401–2409 (1986)

[124] P. W. Smith and R. Hänsch, *Cross-relaxation effects in the saturation of the 6328-å neon-laser line*, Phys. Rev. Lett. **26**, 740–743 (1971)

[125] J. O. Day, E. Brekke, and T. G. Walker, *Dynamics of low-density ultracold Rydberg gases*, Phys. Rev. A **77**, 052712 (2008)

[126] Thibault Vogt *et al.*, *Electric-field induced dipole blockade with Rydberg atoms*, Phys. Rev. Lett. **99**, 073002 (2007)

[127] Z M Li and B Bergersen, *Evaluation of two-centre dipole matrix elements of slater s, p and d orbitals; application to the optical absorption spectrum of nbs 2 monolayers*, Journal of Physics C: Solid State Physics **19**, 7281 (1986)

[128] R J Fonck and D H Tracy, *Use of semiclassical wavefunctions for calculation of radial integrals in the coulomb approximation*, Journal of Physics B: Atomic and Molecular Physics **13**, L101 (1980)

[129] Wenhui Li, I. Mourachko, M. W. Noel, and T. F. Gallagher, *Millimeter-wave spectroscopy of cold rb Rydberg atoms in a magneto-optical trap: Quantum defects of the ns, np, and nd series*, Phys. Rev. A **67**, 052502 (2003)

[130] M. Klapisch, *A program for atomic wavefunction computations by the parametric potential method*, Computer Physics Communications **2**, 239 – 260 (1971), ISSN 0010-4655

[131] William L. Goffe, Gary D. Ferrier, and John Rogers, *Global optimization of statistical functions with simulated annealing*, Journal of Econometrics **60**, 65 – 99 (1994), ISSN 0304-4076

[132] F Y Hajj, *Eigenvalues of any parameter in the schrodinger radial equation*, Journal of Physics B: Atomic and Molecular Physics **13**, 4521 (1980)

[133] R.M. Potvliege, *Strflo: A program for time-independent calculations of multiphoton processes in one-electron atomic systems i. quasienergy spectra and angular distributions*, Computer Physics Communications **114**, 42 – 93 (1998), ISSN 0010-4655

[134] B. H. Bransden and C. J. Joachain, *Physics of Atoms and Molecules* (Longman Group Limited, 1986)

[135] Zhi Miao-chan, Dai Chang-jian, and Li Shi-ben, *Stark structure of the Rydberg states of alkaline-earth atoms*, Chinese Physics **10**, 929 (2001)

[136] Michael G. Littman *et al.*, *Structure of sodium Rydberg states in weak to strong electric fields*, Phys. Rev. Lett. **36**, 788–791 (1976)

[137] Myron L. Zimmerman, Michael G. Littman, Michael M. Kash, and Daniel Kleppner, *Stark structure of the Rydberg states of alkali-metal atoms*, Phys. Rev. A **20**, 2251–2275 (1979)

[138] M L Zimmerman, T W Ducas, M G Littman, and D Kleppner, *Stark structure of barium Rydberg states*, Journal of Physics B: Atomic and Molecular Physics **11**, L11 (1978)

[139] K Sakimoto, *Multichannel quantum-defect theory of the stark effect*, Journal of Physics B: Atomic and Molecular Physics **19**, 3011 (1986)

[140] Thad G. Walker and M. Saffman, *Consequences of zeeman degeneracy for the van der waals blockade between Rydberg atoms*, Phys. Rev. A **77**, 032723 (2008)

[141] Arne Schwettmann, Jeff Crawford, K. Richard Overstreet, and James P. Shaffer, *Cold cs Rydberg-gas interactions*, Phys. Rev. A **74**, 020701 (2006)

[142] Thad G Walker and Mark Saffman, *Zeros of Rydberg–Rydberg föster interactions*, Journal of Physics B: Atomic, Molecular and Optical Physics **38**, S309 (2005)

[143] S. Kunze *et al.*, *Lifetime measurements of highly excited Rydberg states of strontium i*, Zeitschrift für Physik D Atoms, Molecules and Clusters **27**, 111–114 (1993), ISSN 0178-7683

[144] Wei Zhang *et al.*, *Radiative-lifetime measurements and calculations of odd-parity highly excited levels in ba i*, Phys. Rev. A **82**, 042507 (2010)

[145] Mireille Aymar, Chris H. Greene, and Eliane Luc-Koenig, *Multichannel Rydberg spectroscopy of complex atoms*, Rev. Mod. Phys. **68**, 1015–1123 (1996)

[146] W. E. Cooke, T. F. Gallagher, S. A. Edelstein, and R. M. Hill, *Doubly excited autoionizing Rydberg states of Sr*, Phys. Rev. Lett. **40**, 178–181 (1978)

[147] R. R. Jones, C. J. Dai, and T. F. Gallagher, *Ba $6p_j nf_{j'}$ autoionizing series*, Phys. Rev. A **41**, 316–326 (1990)

[148] Richard R. Freeman and Daniel Kleppner, *Core polarization and quantum defects in high-angular-momentum states of alkali atoms*, Phys. Rev. A **14**, 1614–1619 (1976)

[149] M. D. Wright, D. M. O'Brien, J. F. Young, and S. E. Harris, *Laser-induced charge-transfer collisions of calcium ions with strontium atoms*, Phys. Rev. A **24**, 1750–1755 (1981)

[150] Emily Y. Xu, Yifu Zhu, Oliver C. Mullins, and T. F. Gallagher, *Sr 5pnd j=3 autoionizing series and interference of excitation due to bound-state perturbation*, Phys. Rev. A **35**, 1138–1148 (1987)

[151] M J Seaton, *Quantum defect theory*, Reports on Progress in Physics **46**, 167 (1983)

[152] S. A. Bhatti, C. L. Cromer, and W. E. Cooke, *Analysis of the Rydberg character of the* $5d7d\,^1d_2$ *state of barium*, Phys. Rev. A **24**, 161–165 (1981)

[153] J R Rubbmark, S A Borgstrom, and K Bockasten, *Absorption spectroscopy of laser-excited barium*, Journal of Physics B: Atomic and Molecular Physics **10**, 421 (1977)

[154] S. Coeck *et al.*, *Microchannel plate response to high-intensity ion bunches*, Nuclear Instruments and Methods in Physics Research Section A: Accelerators, Spectrometers, Detectors and Associated Equipment **557**, 516 – 522 (2006), ISSN 0168-9002

[155] P. Grafström *et al.*, *Natural radiative lifetimes in the interacting* $5snd\,^{1,3}d_2$ *sequences in Sr*, Phys. Rev. A **27**, 947–949 (1983)

[156] J. E. Sansonetti and G. Nave, *Wavelengths, transition probabilities, and energy levels for the spectrum of neutral strontium (Sr i)*, Journal of Physical and Chemical Reference Data **39**, 033103 (2010)

[157] S.-U. Haq *et al.*, *Photoionization cross section and oscillator strength distribution in the near-threshold region of strontium*, The European Physical Journal D - Atomic, Molecular, Optical and Plasma Physics **44**, 439–447 (2007), ISSN 1434-6060

[158] T F Gallagher, *Time domain spectroscopy of Rydberg atoms*, Physica Scripta **76**, C145 (2007)

[159] S. K. Dutta *et al.*, *High-angular-momentum states in cold Rydberg gases*, Phys. Rev. Lett. **86**, 3993–3996 (2001)

[160] W. R. Anderson, J. R. Veale, and T. F. Gallagher, *Resonant dipole-dipole energy transfer in a nearly frozen Rydberg gas*, Phys. Rev. Lett. **80**, 249–252 (1998)

[161] I. I. Ryabtsev *et al.*, *Stark-tuned förster resonance and dipole blockade for two to five cold Rydberg atoms: Monte carlo simulations for various spatial configurations*, Phys. Rev. A **82**, 053409 (2010)

[162] S. Cohen *et al.*, *Experimental and theoretical analysis of the* $5pnpj = 0, 1, 2$ *autoionizing spectrum of Sr*, The European Physical Journal D - Atomic, Molecular, Optical and Plasma Physics **13**, 165–180 (2001)

[163] R. H. Dicke, *Coherence in spontaneous radiation processes*, Phys. Rev. **93**, 99 (1954)

[164] T. Wang *et al.*, *Superradiance in ultracold Rydberg gases*, Phys. Rev. A **75**, 033802 (2007)

[165] I. Mourachko *et al.*, *Many-body effects in a frozen Rydberg gas*, Phys. Rev. Lett. **80**, 253–256 (1998)

[166] H. G. C. Werij, Chris H. Greene, C. E. Theodosiou, and Alan Gallagher, *Oscillator strengths and radiative branching ratios in atomic Sr*, Phys. Rev. A **46**, 1248–1260 (1992)

[167] H. Jürgen Kluge and Hatto Sauter, *Levelcrossing experiments in the first excited* $^1p_1$ *states of the alkaline earths*, Zeitschrift für Physik A Hadrons and Nuclei **270**, 295–309 (1974), ISSN 0939-7922

[168] E. R. Eliel, W. Hogervorst, T. Olsson, and L. R. Pendrill, *High resolution laser spectroscopy of low-lying p states in Sr i and ba i*, Zeitschrift für Physik A Hadrons and Nuclei **311**, 1–6 (1983), ISSN 0939-7922

[169] N. H. Tran, P. Pillet, R. Kachru, and T. F. Gallagher, *Multistep excitation of autoionizing Rydberg states*, Phys. Rev. A **29**, 2640–2650 (1984)

[170] W. E. Cooke and C. L. Cromer, *Multichannel quantum-defect theory and an equivalent n-level system*, Phys. Rev. A **32**, 2725–2738 (1985)

[171] U. Fano, *Effects of configuration interaction on intensities and phase shifts*, Phys. Rev. **124**, 1866–1878 (1961)